UNIVERSITY OF LIVERPOOL

Investigation of Planar Power Dividers for Wireless Communication Systems

by

Chen, Anqi

B.Eng.

A thesis submitted in accordance with the requirements for the award of the degree of *Doctor of Philosophy* of the University of Liverpool

September 2018

Declaration

I hereby declare that except where specific reference is made to the work of others, the contents of this dissertation are original and have not been submitted in whole or in part for consideration for any other degree or qualification in this, or any other University. This dissertation is the result of my own work and includes nothing which is the outcome of work done in collaboration, except where specifically indicated in the text.

Chen, Anqi

2018

Acknowledgements

First and foremost, I would like to express my deepest gratitude to my main supervisor Dr. Zhou Jiafeng for granting me the precious opportunity to test myself at the highest level. You have encouraged and helped me to grow up from a fresh graduate student to a professional researcher. I learned so much from you both academically and personally. Thank you for the invaluable comments and advice on my research as well as my boyfriend and career. It is a great honour for me to be one of your PhD students, and I hope I have repaid the faith you showed in me. You have taught me to be a rigorous researcher and a realistic engineer with commercial awareness. I will always treasure your support, encouragement, and guidance.

I would also like to thank my parents, especially my father. You have always supported me with no expectation of a reward. Your continuous help and understanding have made my life full of love and I am grateful for everything you have done. I would also like to express my appreciation to my boyfriend. I would never have succeeded without his tolerance, support, encouragement, and patience. This work is dedicated to you.

Special thanks are also paid to my brilliant and lovely colleagues and friends; in particular to Dr. Chaoyun Song, Dr. Qian Xu, Dr. Lei Xing, Dr. Sheng Yuan, Dr. Saqer S. Alja'afreh, Dr. Muayad Kod, Dr. Chaoyun Song, Dr. Zhihao Tian, Dr. Zhouxiang Fei, Dr. Muaad Hussein, Dr. Abed Pour Sohrab, Yuan Zhuang, Manoj Stanley, Wenzhang Zhang, Chen Xu, Tianyuan Jia, Dr. Dajun Lei, Rui Pei, Zhenzhen Jiang, Jingchen Wang and Umniyyah Ulfa for many fruitful discussions and enjoyable moments. Particular thanks should also be paid to Mark Norman, John Owens, Gareth Blacoe and John Gillmore from the Electrical Workshop for always being very kind to me and fabricating my circuits very quickly and beautifully.

Table of Contents

List of Figures

List of Tables

List of Publications

[1] **A. Chen**, Y. Zhuang, J. Zhou, Y. Huang and L. Xing, "Design of a Broadband Wilkinson Power Divider with Wide Range Tunable Bandwidths by Adding a Pair of Capacitors," *IEEE Transactions on Circuits and Systems II: Express Briefs (Early Access)*, 2018.

[2] **A. Chen**, Y. Zhuang, Y. Huang and J. Zhou, 'A Horst-type Power Divider with Wide Frequency Tuning Range Using Varactors,' *IEEE Access,* ISSN: 2169-3536， pp: 1-13, 2018.

[3] **A. Chen**, B. Mousa, Y. Zhuang, Y. Huang and J. Zhou, "Compact Ka-band substrate-integrated waveguide filter with spurlines for satellite communication systems," *2016 IEEE 9th UK-Europe-China Workshop on Millimetre Waves and Terahertz Technologies (UCMMT),* Qingdao, China, 2017.

[4] **A. Chen**, Y. Zhuang, Y. Huang and J. Zhou, "Design of Reconfigurable Power Dividers with Wide Tuning Ranges," *ARMMS RF and Microwave Society Conference, Oxford (accepted)*, 2018.

[5] Y. Zhuang, Zhouxiang. Fei, **A. Chen**, Yi. Huang, K. Rabbi and Jiafeng. Zhou, "Design of multiovtave high-efficiency power amplifier using stochastic reduced order models,", *IEEE Transactions on Microwave Theory and Techniques*., vol. 66, No.2, pp.1015-1023, Feb, 2018.

[6] Y. Zhuang, C. Xu, C. Song, **A. Chen,** W. Lee, Y. Huang and J. Zhou, "A novel method of improving current transformer-based energy extraction from AC power lines under agnetic saturation," *IEEE Transactions on Industrial Electronics*, 2018 (under review).

[7] Y. Zhuang, **A. Chen,** C. Xu, C. Song, Y. Huang and J. Zhou, "Position-free efficient high power-transfer wireless power transfer using multiple bidirectional resonant coils," *IEEE Transactions on Industrial Electronics*, 2018 (submitting).

[8] Q. Xu, Y, Huang, L. Xing, Z. Tian, J. Zhou, **A. Chen** and Y. Zhuang, "Average Absortion Coefficient Measurement of Arbitrarily Shaped Electrically Large Objects

in a Reverberation Chamer," *IEEE Transactions on Electromagnetic Compatibility*, vol. 58, No.6, pp. 1776-1779, doi. 10.1109/TEMC.2016.2587679, 2016.

[9] Y. Zhuang, J. Zhou, Y. Huang and **A. Chen**, "Design of a broadband high efficiency GaN power amplifier for GNSS applications," *IEEE MTT-S International Wireless Symposium,* Shanghai, China, 2016.

[10] Y. Zhuang, C. Xu, S. Yuan, C. He, J. Zhou, Y. Huang, **A. Chen** and W. W. Lee, "Design of an Energy Harvesting System on Power Transmission Lines," *IEEE MTT-S Wireless Power Transfer Conference*, Taipei, Taiwan, May, 2017.

[11] Y. Zhuang, C. Xu, S. Yuan, C. He, **A. Chen**, W. Lee, Y. Huang and J. Zhou, "An improved energy harvesting system on power transmission lines," *IEEE Wireless Power Transfer Conference*, June, 2017.

[12] Y. Zhuang, C. Xu, C. Song, **A. Chen**, W. Lee, Y. Huang and J. Zhou, "Using control coil to improve magnetic energy extraction from AC power line under magnetic saturation," *Asian Wireless Power Transfer Workshop*. Dec, 2017.

[13] Y. Zhuang, C. Xu, **A. Chen**, W. Lee, Y. Huang and J. Zhou, "Distributed Matching Network design for broadband power amplifiers," *IEEE Electrical Design of Advanced Packaging and System Symposium*, Dec, 2017. (Best Paper)

[14] Y. Zhuang, **A. Chen**, C. Xu, Y. Huang and J. Zhou, "Range-adaptive wireless power transfer system using multi-antiparallel loops," *IEEE Asian Pacific Conference on Antenna Propagation*, Auckland, New Zealand, Aug, 2018. (Best Student Paper First Prize).

Acronyms

CAD	Computer-aided Design
CDMA	Code Division Multiple Access
CPS	Symmetric Coplanar Strip-lines
CPW	Coplanar Waveguide
CRLH	Composite Right/Left Handed
DUT	Device Under Test
EBL	Electron Beam Lithography
GSG	Ground-signal-ground
GSM	Global System for Mobile Communications
HSPA	High-Speed Packet Access
LRRM	Line-Reflect-Reflect-Match
LTCC	Lower Temperature Co-Fired Ceramic
LTE	Long-Term Evolution
MHMIC	Monolithic Hybrid Microwave Integrated Circuit
MMIC	Monolithic Microwave Integrated Circuit
mm-Wave	Millimetre-Wave
NA	Network Analyzer
OFDM	Orthogonal Frequency-Division Multiplexing
PCB	Printed Circuit Boards
PD	Power Divider

RF	Radio Frequency
RFID	Radio Frequency Identification
Rx	Receiver
SIW	Substrate Integrated Waveguide
SOLR	Short-Open-Load-Reciprocal
SOLT	Short-Open-Load-Thru
TDMA	Time-Division Multiple Access
Tx	Transmitter
VNA	Vector Network Analyzer

Abstract

This thesis presents several studies and designs on power dividers, filters and diplexers to overcome respective challenges of these topics. This thesis focuses on the following three areas.

The first research area focuses on improving the bandwidth of Wilkinson-type power dividers. For broadband power dividers design, the impedance matching is challenging. A novel design method is proposed to broaden the bandwidth of Wilkinson-type power dividers by adding capacitors in parallel with the main structures. Adding capacitors in parallel with transmission lines is firstly proposed to control of the reflection zero frequency and operating bandwidth. The fabricated circuit occupies a very compact circuit size at the same time. A two-way power divider is designed and measured to validate the proposed method. The measurement indicates that the device has a 15-dB bandwidth of 2.73:1. The proposed method can be applied to the design of multi-way multi-section power dividers. An eight-way power divider is designed and fabricated. The measured response has a bandwidth of 2.67:1. The proposed power divider exhibits a much wider tunable bandwidth than other similar works. In addition, the design has a simple layout, compact size, good physical and electrical isolation features.

The second area concentrates on reconfigurable power dividers. A novel power divider with a wide operational frequency tuning range is presented and investigated. Using varactors in parallel with transmission lines is firstly proposed to extend the operational frequency tuning range. The reconfigurable feature is realized by electrically adjusting the bias voltage on varactors. Theoretical formulas for the characteristic impedance and electrical length of the transmission lines of the power divider are derived and analysed to precisely control the operating frequency band. A power divider has been designed and fabricated to validate the proposed design method. The measured results indicate that the power divider can achieve a 20-dB tunable operating frequency range of 4.63:1 which is the largest among all the other similar works. Moreover, the power divider has a simple layout and a very compact size of $0.2\boldsymbol{\lambda_g} \times 0.16\boldsymbol{\lambda_g}$. This work demonstrates the excellent potential for working with frequency agile components in modern communication systems, such as antenna arrays.

The last area under investigation is mm-Wave (Millimetre-Wave) coplanar power dividers design. For mm-Wave applications, most of existing power dividers suffer from large size,

high cost, complex fabrication processes and lossy performance. On these circumstances, CPW power dividers using coupled resonators at V band are designed. This work has three main contributions. The first is that the power dividing ratio of a power divider can be precisely controlled via calculation. The second one is reducing circuit loss by replacing T- or Y-junctions to eliminate air-bridges. The last contribution is circuit miniaturization by using spiral resonators. Mathematical proof and parametric studies have been done in the thesis. A diplexer is designed using this method which indicates an extensive applicability of the method for RF components designs.

This thesis has successfully demonstrated novel design methods and techniques for power divider designs. Several challenges including complex circuitry, large size and unnecessary loss have been overcome by using the presented technologies. The research and knowledge in this thesis should be of great significance to the future development of power dividers or even other RF devices.

Chapter 1 Introduction

Advanced researches are aiming to keep up with the social demands for a new generation of wireless communication functions. As shown in **Fig. 1. 1**, the development of modern wireless communication contributes to every aspect of life globally including health & safety, security and wireless charging, etc. Radio Frequency (RF) devices, as the physical fundamentals for signal transmission and receiving, play a vital role in wireless communication systems.

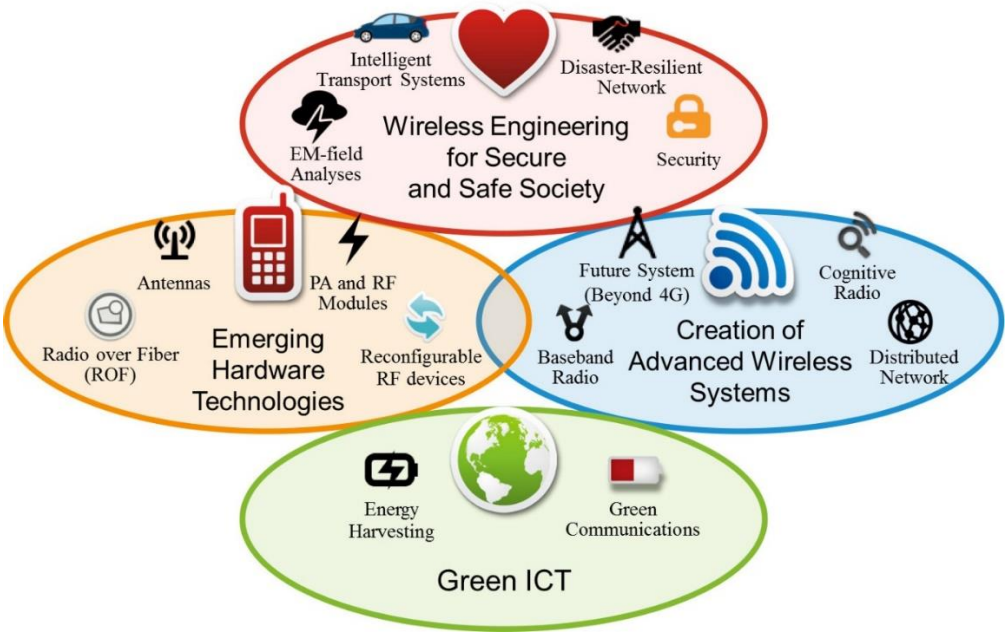

Fig. 1. 1. A diagram of wireless communication networks [1].

1.1 Power Dividers

Power dividers (PDs), also called power splitters, are one of the essential components in building wireless communication systems. A PD can be used to split the power from the input port into several smaller portions to different output ports. On the other hand, the PD can be used for combining power from several input ports into one output port once the jobs of the

input and output ports are reversed. The features and performance of the PD regarding operating frequency, bandwidth, output ports isolations, circuit size etc. will significantly affect the overall performance of the wireless communication system built on it. With the development of communication systems, especially 5G communications, the spectral range for data transmission is higher and higher. Multiple communication standards are desired due to that a single standard transmission cannot satisfy the required performance of the system. In that case, PDs are essential for assigning the signal to different paths. In RF systems and measurement control systems, like power amplifier network, the performance of the power distribution and coupling elements are crucial to the quality of the whole system. Many PDs are designed to have different features to satisfy the requirements of a high-performance communication system.

Resistive PD.

The easiest method to realise a PD is to use simple purely resistive elements [2]. Choosing proper values of the resistors used in the PD can enable the input/output impedance of the system to be constant when splitting or combining the power with the desired ratio. One of the most common and fundamental forms of the PD is a three-way PD. The most adopted configurations of the three-way resistive PD, namely star and delta format, are shown in **Fig. 1. 2**(a) (b) as follow.

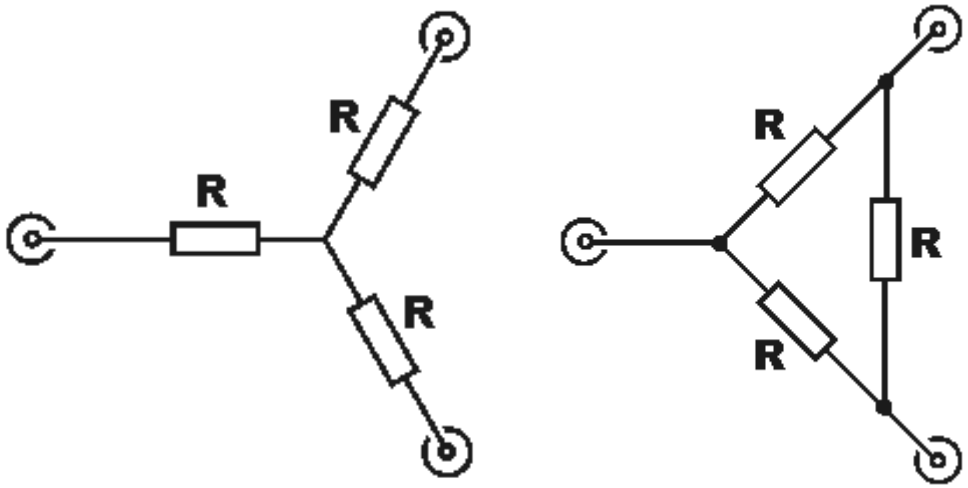

(a) (b)

Fig. 1. 2. Schematic of the resistive PD, (a) star format PD, (b) delta format PD.

For the star PD, the series resistors to the star centre are all equal. Since the input impedance should be equal to the load impedance Z_0 and the resistance can be derived by

$$R + {(R + Z_0)}/{2} = Z_0$$

$$R = {Z_0}/{3} \tag{1.1}$$

Eq (1.1) shows that the resistance is one-third of the characteristic impedance of the ports. For the delta format PD, the resistance of the resistors is identical to that of the characteristic impedance of the RF system. With these simple forms of resistive PDs or splitters, any port can be used as the input while the rest two severing as the outputs.

It should be mentioned that the resistive PD has double loss compared to a lossless PD's insertion loss. Taking the star format PD as an example, for an N-way star format PD, the power dissipated in resistor *A* that is close to the common port is $P_{dissipated\_A} = P_{in} \times (N-1)/(N+1)$, while the power dissipated in the two resistors *B* and *C* that are close to output ports can be calculated as $P_{dissipated\_B/C} = P_{in} \times (N-1)/[(N+1) \times N^2]$. For example, when *N* equals to 2, the output power is only 25% of the input power (-6.02 dB). Furthermore, it is very convenient to achieve multi-ports PD by connecting more resistors to the centre of the star. But the power loss will be higher, which is acceptable for some applications. Resistive PDs are very easy to implement, and they can provide an extensive operating bandwidth as the resistors are not frequency dependent. Also, a resistive PD is relatively cheap. These factors make them very attractive for many applications if the main disadvantage of power loss can be tolerated.

T-junction PD.

The T-junction [3]-[4] is a simple lossless three-port network that can be used for power dividing or power combining. It can be formed in virtually any type of transmission line medium (commonly used in the waveguide, microstrip or stripline structure). The lossless T-junctions shown in **Fig. 1. 3**(a)-(c) can all be modelled as a junction of three transmission lines as shown in **Fig. 1. 4**. Z_1 represents ports impedance, and Z_2 and Z_3 indicate load impedances at Port 2 and Port 3.

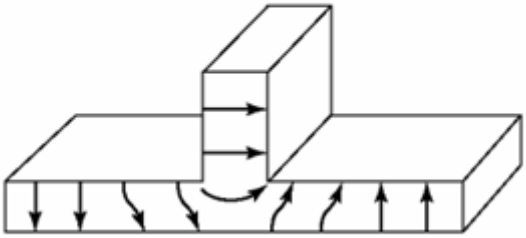

(a)

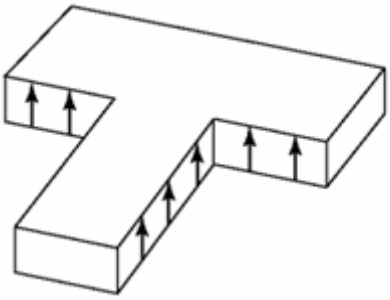

(b)

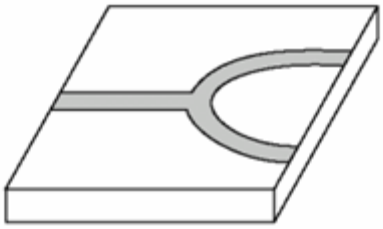

(c)

Fig. 1. 3. (a) E-plane waveguide, (b) H-plane waveguide and (c) Microstrip T-Junction.

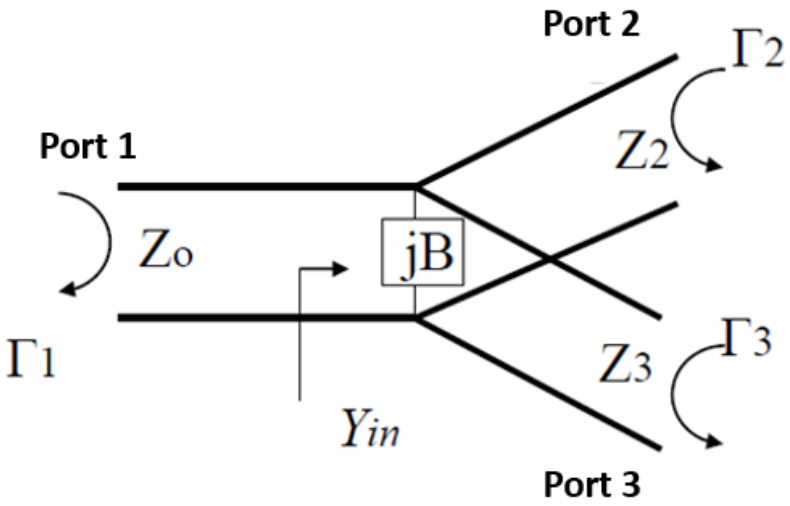

Fig. 1. 4. Transmission line model of a lossless T-junction.

Due to the fringing fields and higher order modes that associated with the discontinuity, stored energy that can be regarded as a lumped susceptance, *B*. To have input impedance matched, the following equation should be satisfied (1.2)

$$Y_{in} = jB + \frac{1}{Z_2} + \frac{1}{Z_3} = \frac{1}{Z_0} \tag{1.2}$$

$$B = 0 \text{ "not practical"}$$

$$\Rightarrow \text{A lossless divider has mismatched ports}$$

A transmission line is assumed to be lossless so that the characteristic impedances are all real. In that case, *B* should be zero for perfect matching. However, *B* is not negligible in practice, so a lossless divider has mismatched ports. But some reactive tuning element can usually be added to the divider to cancel the susceptance *B*, at least over a narrow frequency range [5]. If not, there will be poor isolation between the two output ports, and there will be a mismatch looking into the output ports. The T-junction PD realised by the transmission lines will maintain a good power division efficiency with a minimal loss.

Wilkinson-type PD.

The Wilkinson N-way power splitter that shown in **Fig. 1. 5** was invented by Ernest Wilkinson [6] in 1960. The Wilkinson-type PD uses quarter-wavelength transformers, which are easy to be fabricated using transmission lines on printed circuit boards (PCB). As a result, it offers the possibility of a very cheap and straightforward splitter/divider/combiner while still providing high levels of performance regarding loss and isolation between output ports.

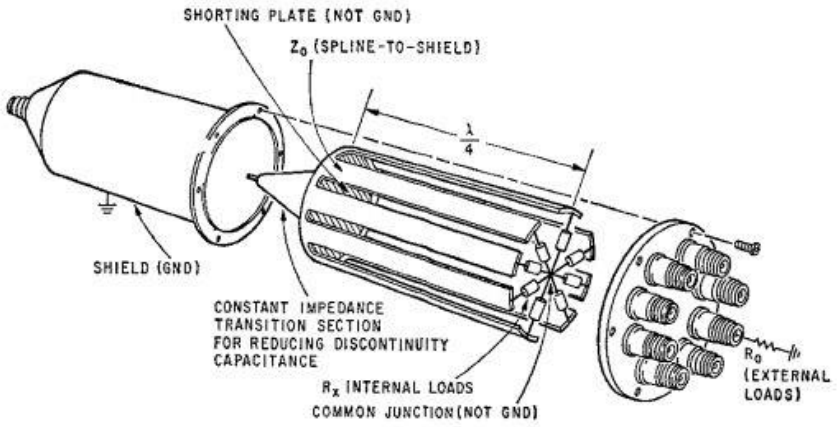

Fig. 1. 5. N-way Wilkinson PD [6].

The *N*-way PD proposed by Wilkinson in [6] can split an input signal into *N* equal phase output signals or combine *N* equal-phase signals into one in the opposite direction.

Looking at a two-way PD first, the main path of Wilkinson-type circuits relies on quarter-wave transformers to match the split ports (output ports) to the common port (input port). Due to the difficulty of achieving the perfect matching of a three-ports reciprocal network, usually a resistor will be added between the output ports. The added resistor will not only contribute to the terminations matching but also provides good isolation between the output ports. An equal-amplitude, two-way splitting, single-stage Wilkinson is shown as **Fig. 1. 6**. The two split paths are quarter-wave transformers of impedance $\sqrt{2}Z_0$. Therefore, these two paths provide the same potential over the two ends of the resistor, the resistor consumes no resistive power, so an ideal Wilkinson splitter is 100% efficient. Although Wilkinson PDs can be used as N-way PDs, it is difficult to realise a planar structure since all ports need to connect to a common point with a resistor.

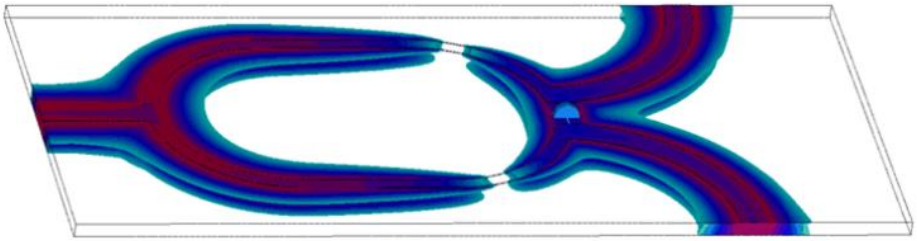

(a)

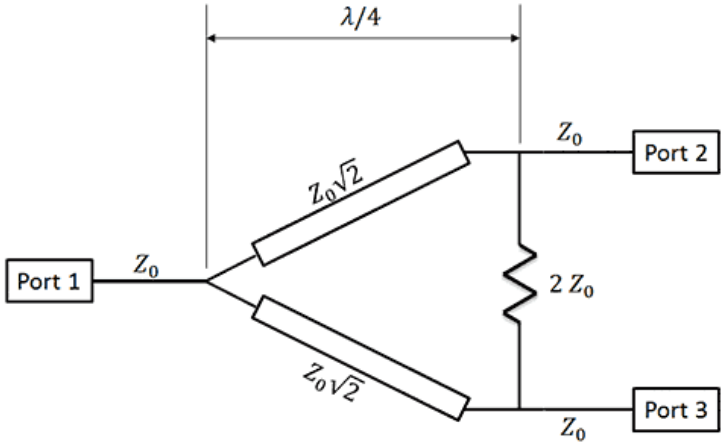

(b)

Fig. 1. 6. (a) Signal split in a two-way Wilkinson PD, (b) schematic of a two-way Wilkinson PD.

A two-way Wilkinson PD is relatively simple and can be realised by different technologies such as printed components on a printed circuit board (PCB) and lumped inductor and capacitor elements [7]. From the power loss point of view, if perfect elements are adopted, the Wilkinson PDs would not present any extra power loss from the division of the power. In practice, the real components used for the Wilkinson splitter can be of low loss, especially when PCB transmission lines are used along with a low loss PCB substrate material.

Furthermore, contributed by the isolation circuit realised by resistors, high-level isolation is introduced between the output ports which will prohibit the ports from interfering with each other. On the other hand, the realisation of the Wilkinson PD is highly dependent on the quarter wavelength transmission lines. Once the operating frequency deviates from the original one, it will cause a vital impedance mismatch, and limit the performance. Thus, the traditional Wilkinson PDs are only suitable for relatively narrow-band applications.

Rat-race Coupler.

The Rat-race coupler is one of the 180° hybrid couplers that are widely used in PD and combiner designs. The schematic of a conventional rat-race coupler is outlined in **Fig. 1. 7**[8]. It is a lossless reciprocal four-port network. It comprises three 90° branches and one 270° branch. In many references, the 270° branch is always decomposed into three 90° sections to simplify the design. The characteristic impedance of the ring should be $\sqrt{2}$ times the characteristic impedance of the port terminations with the purpose of impedance

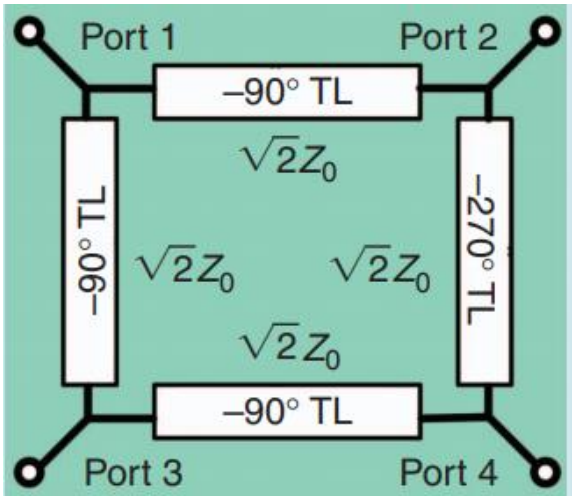

(a)

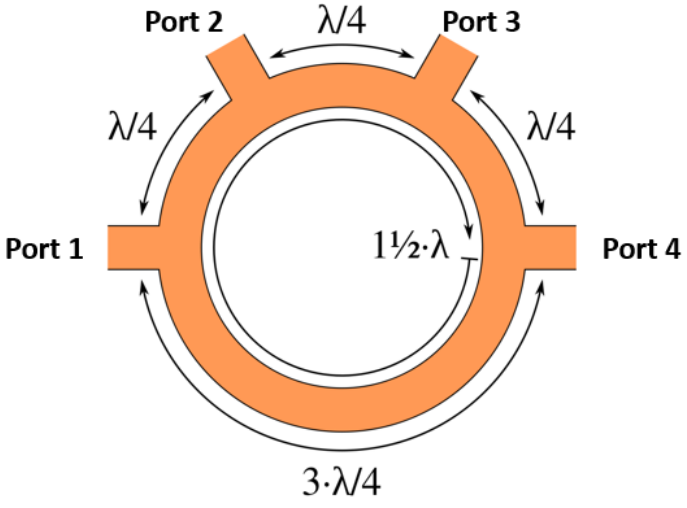

(b)

Fig. 1. 7. (a) Circuit schematic and (b) configuration of a conventional rat-race coupler [8].

matching for all ports. As a PD, the rat-race coupler can be used for in-phase operation and 180° out-of-phase operation. For the case of the in-phase operation, a signal applied to port 1 is divided equally into Ports 2 and 3 with the same phase shift, and Port 4 is isolated. Conversely, for out-of-phase operation, a signal injected into Port 4 is divided evenly into Ports 2 and 3 with 180° phase difference, and Port 1 is isolated.

The rat-race coupler is easily realisable and can be implemented in numerous technologies, such as microstrip line, stripline and waveguide (magic-tee). Advantages are the simple design and high degree of isolation between the input ports. However, it also has serious drawbacks, such as relatively narrow bandwidth and sizeable occupied area due to the requisite 270° transmission line section [8].

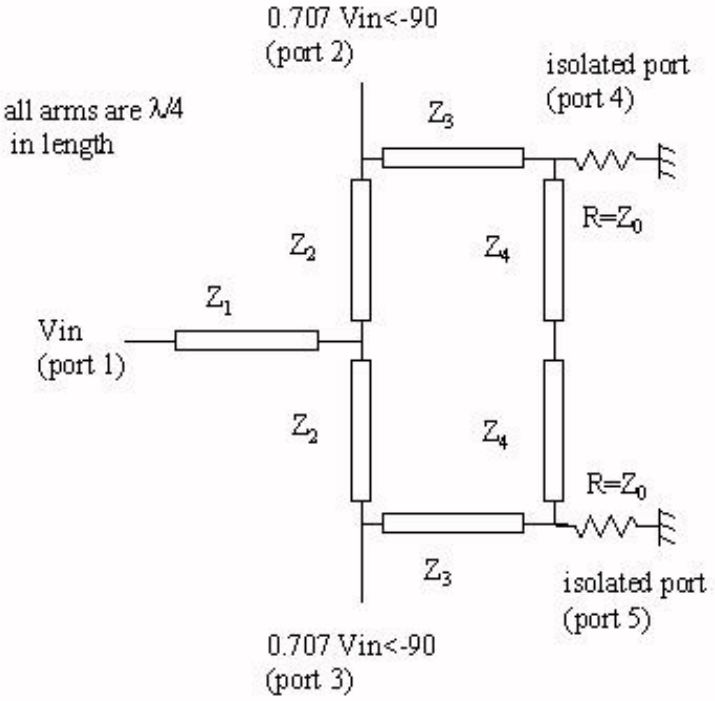

Fig. 1. 8. Basic Gysel topology.

Gysel PD.

Ulrich Gysel [9] proposed a new structure (shown in **Fig. 1. 8**) of PD in 1975. The configuration is similar to a combination of a Wilkinson and a rat-race coupler [10]. The main advantage of the Gysel power splitter is its power handling capacity. In a Wilkinson splitter, the resistor is embedded into the network and must provide a short phase length for the scheme to work. The

terminations in a Gysel are equal to Z_0 and can be high-power loads if power handling is a requirement. The Gysel divider is often used in kilowatt-level power combining, for example, if some redundancy in a 50,000-Watt television transmitter is demanded a five-way Gysel combiner with 15,000 Watt tubes could be use and it is able to remove one of the tubes for service or replacement without taking the transmitter off-line.

1.2 PD in Modern Wireless Communication Systems

The increasing number of frequency bands and spectrum fragmentation demand the system having broadband features. Modern wireless communication systems are evolving and applying a multiplicity of emerging communication standards such as high-speed packet access (HSPA), long-term evolution (LTE) and microwave access (WiMAX). These techniques require different centre frequencies, bandwidths and modulation schemes [11]. Wireless service providers have to offer a large number of radios for each standard resulting in a very costly overall network infrastructure. To decrease costs, the flexibility and reusability of RF transmitters and transceivers should be improved to allow the combination of different technologies in a single piece of hardware. Driven by the demands of the consumer for wireless services such as portable devices, smartphones and Internet access with the high data rate, the industry and academia have responded and offered improved services and standards [12] [13]. For example, the first generation named 1G cellular was introduced in the early 1980s, based on the analogue network operated at 900MHz. Then, the 2G cellular system based on Time-Division Multiple Access (TDMA), Global System for Mobile Communications (GSM), and Code Division Multiple Access (CDMA) was announced ten years later, which provided much-improved data rate. Till now, the 4G using OFDM technology is operated around the world offering high quality and enhanced functionality services. Nowadays, the idea of the 5G system has been proposed to deliver higher data rate services. It will demand broader bandwidths and higher efficiency with lower cost and smaller size devices. In this case, the design of broadband, multi-band tunable, high isolation and compact PD attracts attention and becomes the research topic.

In general, the main preferred functionalities of a PD can be summarized as the following aspects.

- Broadband technology has drawn much attention to wideband antennas and antenna arrays [1]. As an essential part of these applications, PDs need to keep up with the spectrum extension.
- Many wireless communication systems have multi-band operating ranges. GSM works at 0.9 GHz and 1.8 GHz; WLAN system works at 2.4/5.2/5/8 GHz. Many RF devices tend to have a multi-band or reconfigurable feature to make the most of existing spectrum and infrastructure sources.
- Nowadays, people demand mini portable products, like smaller and thinner mobile cell phones and RFID (Radio Frequency Identification). Circuit miniaturisation and integration are the trends. Obtaining compact sizes and maintaining high performance of the device will be the primary challenge.

From the functionality point of view, there are PDs with different frequency configuration which includes dual-band, multi-band and wideband PDs. Those types work for multi-standard communication systems. In addition to multi-band or broadband features, PDs having tunable operating frequencies are valuable for constructing multi-standard systems. Despite tuning operating frequencies, power ratio can also be tuned. For some applications like antenna arrays, and power amplifiers, power division ratios need to be customized. In those cases, PDs with different power division configurations are desirable. Although most of the time the word "power divider" indicate in-phase power division, arbitrary phase differences are required in many applications like phased arrays.

In addition to the pre-mentioned types, function–integrated (hybrid) PDs are also very popular, such as PDs with different termination impedances, PDs with filtering response and PDs with harmonic suppression. There are several hybrid PD examples demonstrated in the next chapter. Usually, those multi-functional PDs are suitable for systems that are very complex and highly integrated to save space and avoid unnecessary loss.

From the fabrication technology's aspect, there are conventional transmission lines PDs including microstrip, stripline, coplanar waveguide, etc. It is usually easy to calculate the dimensions and fabricate. However, to achieve advanced performance, unconventional transmission lines are widely used, like coupled-line PDs and PDs using right-/left-handed (CRLH) transmission lines and Lower Temperature Co-fired Ceramic (LTCC). The structures

of above PDs follow the fundamental topology like Wilkinson type PDs. The substrate integrated waveguide (SIW) is also a popular technology. By using metallic via holes to prevent signal leakage a "planar waveguide" can be formed. An SIW has waveguide properties but without a bulky size or heavyweight.

1.3 The Motivations of the Work

In recent years, with the rapid development of wireless communication systems, many ideas and technologies have been applied to improve the overall performance of the systems. Passive PDs, as an essential component of RF modules, have attracted more and more interests in researching and industry field. The nature of a three-port network determines that it cannot be simultaneously lossless, reciprocal, and matched at all ports. As a result, pursuing optimised performance for a PD is worth investigating. Nowadays, PDs have already gone far beyond original prototypes to keep up with the innovation of modern communication technologies. For practical use, people care about the performances, functions and fabrication processes of a PD. State-of-the-art PDs exhibit improvement in various aspects according to different applications and specifications. Subsequently, function-integrated PDs attract more and more attention because this is the trend to have compact integrated systems.

To summarise, more works can be done to improve the performance of a PD. The main objectives of this research are listed below:

- To study the wideband PD technologies and investigate the mechanisms of these methods.
- To design a wideband PD with a simple layout and compact size. Analytical solutions for determining the design parameters should be produced.
- To further study the mechanism of designing reconfigurable PDs and evaluate the pros and cons of each method. To investigate multi-functional PDs.
- To develop a reconfigurable PD with a wide centre frequency tuning range and has a very compact size.
- To explore mm-Wave PD designs and fabrication technologies.

- To design an mm-Wave coplanar waveguide PD using coupled resonators for easy fabrication and reduction of conductor loss at such high frequencies.

1.4 Thesis Organization

The content of this thesis are organized in the following manner.

Chapter 1 provides the background of the project, the motivations of the work and the outline of the thesis.

Chapter 2 is the literature review of previous works on PDs. The main focuses of the literature review are broadband PDs, reconfigurable PDs and mm-Wave PDs.

Chapter 3 presents a wideband PD design. The procedures and methodology of the design are provided. Measurements were taken to validate the design.

Chapter 4 introduces a reconfigurable PD with a wide centre frequency tuning range. The tuning mechanism is explained, and the relationship between the varactors and the tunable centre frequency is analysed in detail. Measurements were taken for validating of the design.

Chapter 5 explores mm-Wave CPW PDs using coupled resonators. The size can be significantly minimized by using G-type spiral resonators. Also by the use of a common resonator to replace a T-junction or Y-junction, the size can be further reduced. Moreover, by controlling the coupling between the resonators, a different power dividing ratio can be achieved. Based on the coupling method, a diplexer can also be implemented by controlling the size and distances of resonators.

Chapter 6 concludes the works. The main objectives and contributions of the work are reviewed and highlighted. Moreover, the potential extensions of the work and its challenges are presented. This chapter has also listed several future research topics worthy of investigation.

References

[1] Hilink.com.cn. (2018). Reactive Power Splitter-Power Splitter-Manufacturer of Passive Products. [online] Available at: http://www.hilink.com.cn/en/Power_divider/show/28.html [Accessed 17 Sep. 2018].

[2] Adams, Greg. "Designing Resistive Unequal Power Dividers." High-Frequency Electronics (2007): 48-50.

[3] C. J. R. Smith and H. H. Sigmarsson, "Microstrip T-junction power divider with exponentially tapered transmission lines," *IEEE Microw. Wireless Compon. Lett.,* vol. 26, no. 12, pp. 987–989, Dec. 2016.

[4] G. R. Branner, B. P. Kumar, and D. G. Thomas, Jr., "Design of microstrip T junction power divider circuits for enhanced performance," in *IEEE Proc. 38th Midwest Circuits Syst. Symp.*, 1995, vol. 2, pp. 1213–1215.

[5] D. M. Pozar, "Power dividers and directional couplers," in Microwave Engineering, 4th ed. Hoboken, NJ, USA: Wiley, 2012, ch. 7, pp. 362–364.

[6] E. Wilkinson, "An N-way hybrid power divider," *IEEE Trans. Microw. Theory Thech.*, pp. 116-118, 1960.

[7] Djordjevic, A. Scattering Parameters of Microwave Networks with Multiconductor Transmision Lines: Software and User's Manual. Artech House, 1990.

[8] H.-X. Xu, G.-M. Wang, and K. Lu, "Microstrip rat-race couplers," *IEEE Microw. Mag.*, vol. 12, no. 4, pp. 117–129, Apr. 2011.

[9] U. H. Gysel, "A new N-way power divider/combiner suitable for highpower applications," in *IEEE MTT-S Int. Microw. Symp. Dig*., May 1975, pp. 116–118.

[10] J. Reed and G. Wheeler, "A method of analysis of symmetrical four-port networks," *IRE Trans. Microwave Theory Tech*., vol. MTT-4, pp. 246-252, Oct. 1956.

[11] Subharthi Paul, Long Term Evolution (LTE) & Ultra-Mobile Broadband (UMB) Technologies for Broadband Wireless Access, [online] available at: http://www.cse. wustl.edu/~jain/cse574-08/ftp/lte.pdf [Accessed 15 Oct. 2018]

[12] Jaiswal, S., Kumar, A. and Kumari, N., 2014. Development of wireless communication networks: From 1G to 5G. International Journal of Engineering and Computer Science, pp 6053-6056.

[13] Sharma P. "Evolution of mobile wireless communication networks-1G to 5G as well as future prospective of next generation communication network." International Journal of Computer Science and Mobile Computing. 2013 Aug;2(8):47-53.

Chapter 2 A Review of Power Dividers

In this chapter, a number of state-of-the-art planar PDs are introduced and discussed. The innovations of these PDs lie in their performance breakthrough, physical configurations, and function integrations. This chapter provides a basis for the development of planar PDs.

2.1 Broadband PD Technologies

PDs with different frequency configurations are quite important for modern communication systems that require multi-standards. Since conventional PDs [1] [2] can not provide sufficient bandwidth, many works have been reported on dual-band [3]-[18], multi-band [19]-[20], and broadband PDs [21]-[28]. Compared to multi-band designs, PDs with wide frequency bands are more desired because they are not only able to meet the requirements of the multi-standard system, but can also contribute high-speed data rate [29]. It is reported in the literature [30] that there are several techniques that identify the broadband PDs. The pros and cons of those techniques will be analysed and discussed in the following sections with some typical design examples. The discussion of the bandwidth in this thesis will be based on the scattering parameters S_{ij}.

2. 1. 1 PDs with Multi-section

Theoretically, the conventional single-section two-way Wilkinson-type PD has a usable bandwidth (20-dB return loss) of 1.44:1. The impedances are perfectly matched at all ports that generate reflection zeros at the centre frequency and its harmonic frequencies. However, S_{ii} and S_{ij} between each adjacent reflection zeros are insufficient to make it a wideband. As a result, the operational band only consists of one reflection zero. To broaden the operational bandwidth, the reflection zeros can be allocated closer to make S_{ii} and S_{ij} sufficient (ideally all below 20 dB) for a wideband response. This is done by carefully choosing the impedances and lengths of the transmission lines. In that case, the operational band will consist of several reflection zeros. This cannot be accomplished by using conventional single-section Wilkinson PDs. On

the other hand, adapting multi-section paths to the main circuit, as shown in **Fig. 2. 1**(a), is a comprehensive method to realise the broadband response.

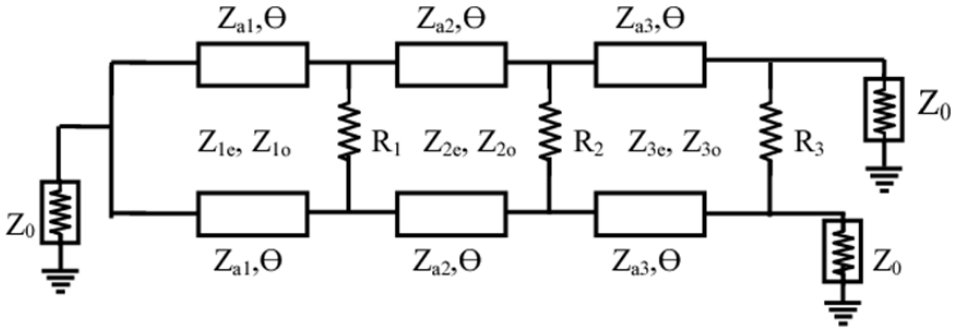

(a)

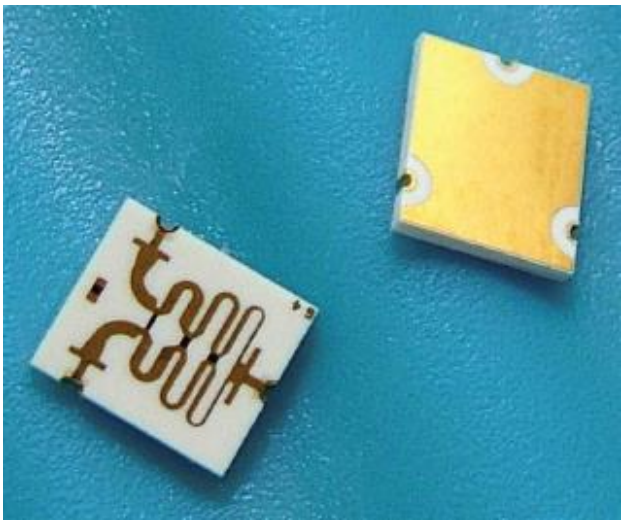

(b)

Fig. 2. 1 (a) Schematic of three-section Wilkinson PD, (b) photo of industrial products.

The multi-section method was introduced in 1968 [31] to further broaden the operational bandwidth of the Wilkinson PDs. Each section consists of a pair of transmission lines and a resistor. This is done so that the circuit is like several single-section two-way Wilkinson PD cascaded end to end. The multi-section structure can provide a significant increase in bandwidth. More specifically, bandwidth can be increased to 2:1 with two sections, 4:1 with four sections, and even 10:1 with seven sections. Theoretically, the bandwidth of multi-section PDs can be extended without limitation with infinite sections. However, the size will be sacrificed accordingly as shown in **Fig. 2. 1**(b). As shown in [30], the circuit is composed of a

finite number of resistors and the same transmission lines, and so synthesis for optimum performance can be concluded. The design procedure is easy for two sections PDs, but calculation difficulties of PDs with more sections will increase exponentially. Although in the following half-century, many works [32]-[34] have been conducted on optimising the algorithms with the help of simulation software, the designs are reliant on the approximations and software tuning processes. In addition to the calculation difficulties, the size of a multi-section Wilkinson PD is multiplied because the length of each section is usually a quarter wavelength.

In summary, the advantages are that this multi-section solution can effectively provide unlimited bandwidth, and the bandwidth in terms of design parameters can be calculated and predicted. However, the longer transmission lines for the wider bandwidth increased the circuit size which in turn brings more insertion loss.

To save space of the circuit, Yu [35] has analysed broadband Wilkinson PDs based on a segmented structure formed by many transmission line segments in shunt with grounded capacitors and series resistor-capacitor networks. The word "segment" is to distinguish "multi-section"; while the latter indicates a multiple quarter-wavelength transmission line section, "segmented" implies the total length of transmission lines is $\lambda/4$ which downsizes the circuits. The layout of a segmented structure is shown in **Fig. 2. 2**. The reason that this work is put in "multi-section" is because the design still needs a number of resistors to connect each segment. The operation bandwidth of Wilkinson PDs with a fixed transmission line length can be extended by replacing the original quarter-wave transmission line section with the proposed impedance transformer segmented. As shown in **Fig. 2. 3**, the measured bandwidth is 1 in this work, which is a very significant improvement compared to the previous best-reported bandwidth of 2.03:1 in [18].

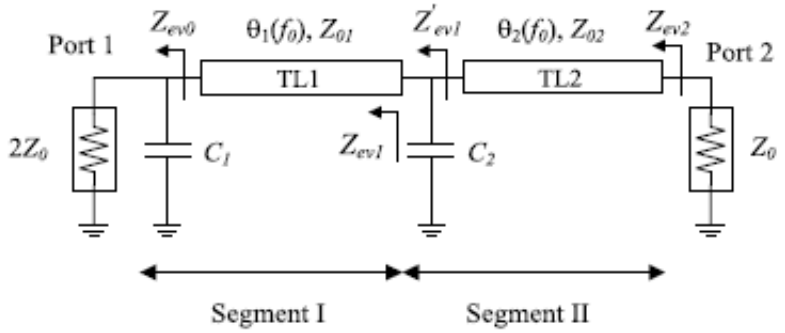

(a)

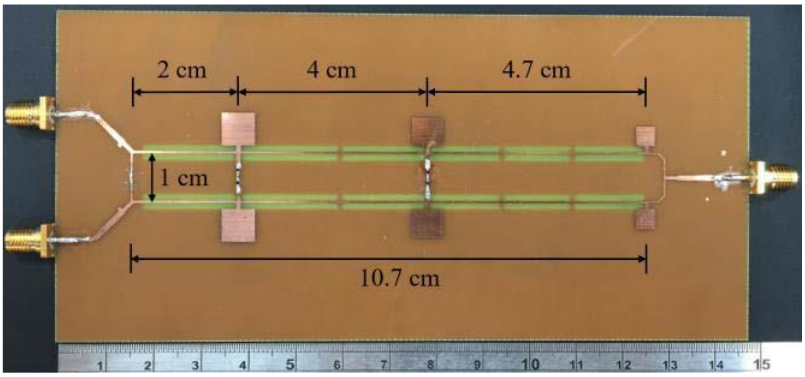

(b)

Fig. 2. 2 (a) Even-mode circuit of the design in [34] based on the structure of two segments, (b) printed circuit.

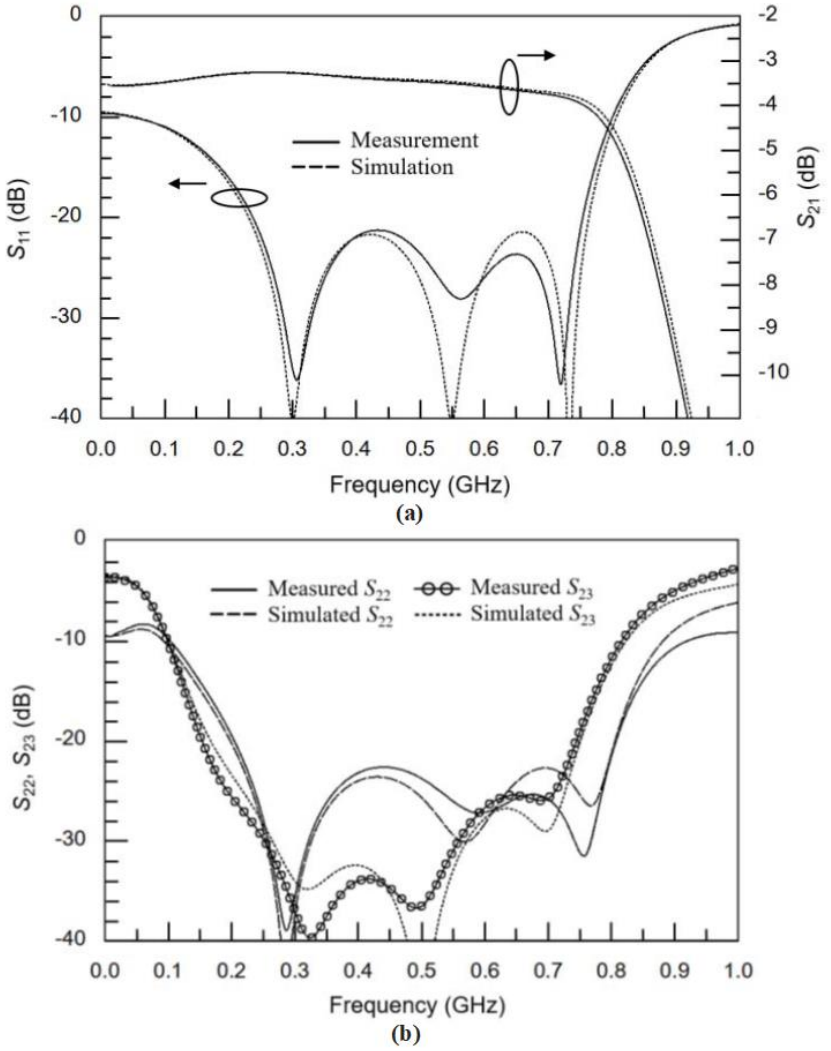

Fig. 2. 3 (a) Simulated and measured S_{11} and S_{21}, (b) simulated and measured S_{22} and S_{23} [35].

Theoretically, more implemented segments can achieve larger bandwidths. Practically, though, the limitations of the maximum achievable bandwidth depend on the implementation of the required components values. In addition, too many lumped elements will consume more energy.

2. 1. 2 PDs with Stepped-impedance Transformers

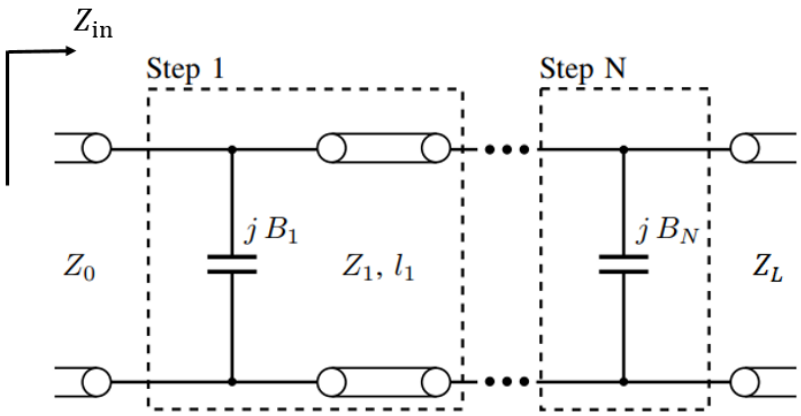

Fig. 2. 4 Structure of stepped-impedance transformer.

Comparable to the multi-section solution, the use of stepped-impedance lines is also an easy and accessible method to achieve broadband PDs. Stepped-impedance lines, also known as stepped-impedance transformers, were initially proposed by Young [36] in 1962. The stepped-impedance transformer is shown in **Fig. 2. 4**. It consists of several lossless transmission line sections with electrical length φ and terminated in resistive load Z_0 and Z_L. The input impedance looking into the transformer can be calculated by continually integrating the input impedance of lossless transmission line formula (2.1) [36]:

$$Z_{in}(l) = Z_0 \frac{Z_L + jZ_0 \tan(\beta l)}{Z_0 + jZ_L \tan(\beta l)} \tag{2.1}$$

where phase constant $\beta = \frac{2\pi}{\lambda}$ and λ indicates the wavelength. Stepped-impedance transformers are widely applied in filter designs for circuit size reduction [37]-[40]. For Wilkinson PDs, output ports need to be close in order to minimize phase shift across the resistor. However, an extra 50 Ω transmission lines are needed to connect the resistor to the output ports. The stepped-impedance transformers utilize the space occupied by 50 Ω interconnection lines to improve impedance matching on all ports, in turn reducing the circuit size simultaneously. Refs [41]-[43] provide some mathematical solutions of choosing the values for these transmission lines.

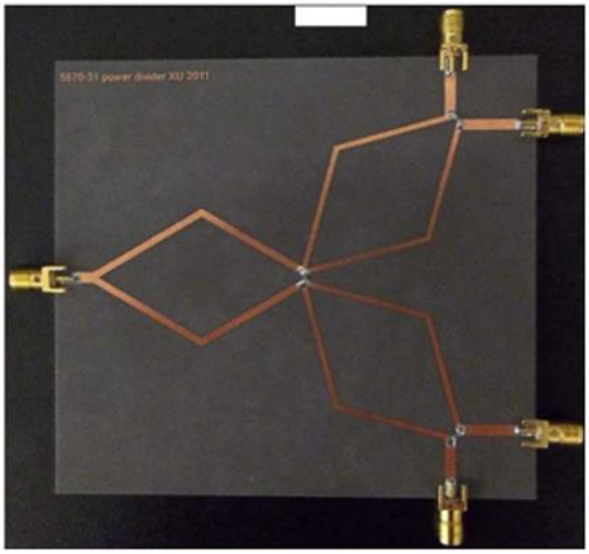

(a)

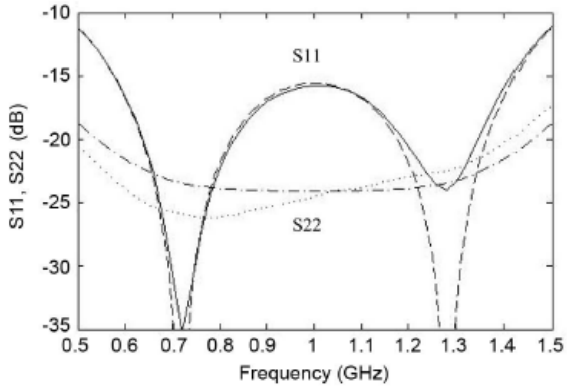

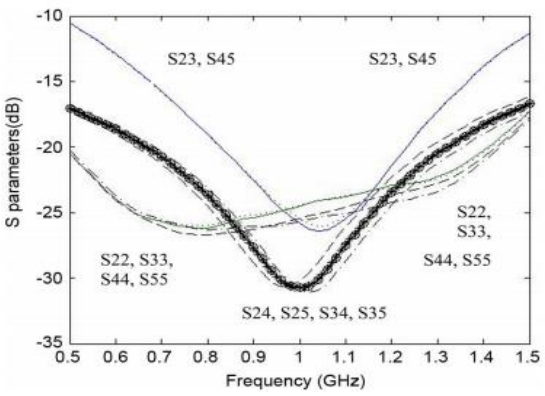

(b) (c)

Fig. 2. 5 (a) Photograph of the designed four-way PD, (b) S_{11} S_{21} and output return losses and (c) isolations of the designed four-way PD with ripple 15 dB [46].

Papers [44]-[45] propose an impedance-matching method of interconnecting transmission lines between adjacent stages to achieve wideband feature. Ref [46] has demonstrated a comprehensive design of stepped-impedance transformers by choosing different parameters at different stages to have concurrent impedance matching between stages, broadening the bandwidth significantly. As shown in **Fig. 2. 5**(a), by cascading three single-section two-way PDs into a four-way one, the measured results demonstrate a bandwidth of 3:1 as **Fig. 2. 5**(b) (c) indicate. This method employs Chebyshev polynomials [47]-[49] to the interconnecting

transmission lines between stages. Theoretically, for the given number of stepped-impedance transformers, the optimised design parameters can indeed be calculated. This method could be very effective when dealing with conventional multi-stage, multi-way Wilkinson PDs with plenty of interconnecting transmission lines, but these interconnecting transmission lines will inevitably occupy more space.

2. 1. 3 PDs with Coupled-Line

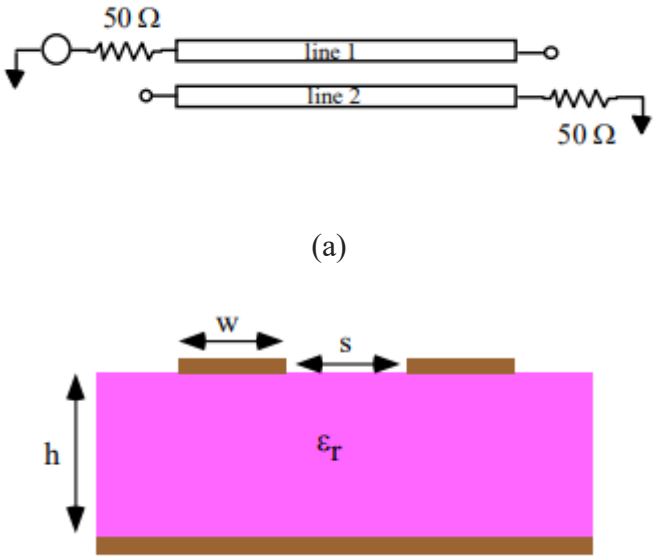

Fig. 2. 6 (a) Schematic model of coupled-line, (b) coupled-line side view.

Coupled-line is one type of transmission line that is widely used in microwave integrated circuit designs. An example of two microstrip coupled-lines over a common plane as shown in **Fig. 2. 6**(a) (b). Coupling will gradually emerge when they are sufficiently close to each other. The coupling strength between the coupled lines can be modelled by introducing a mutual inductance and capacitance per unit length, L_m and C_m. When $L_m = C_m = 0$, they are reduced to the uncoupled equations describing the isolated individual lines.

Coupled-line resonators are widely used in wideband filter designs (see works in [50]-[55]). As a result, these types of PDs are typically designed by following the filter design synthesis

which can generate finite transmission poles in the band, just as filters are performed. The transmission poles and bandwidth can therefore be predicted and controlled according to the filter performance. Moreover, coupled-lines and microstrip-slotline transitions [56]-[59] can be regarded as transmission line transformers, which is a benefit for size reduction and is capable for further bandwidth extension.

Conventional two-way Wilkinson PDs consists of two quarter-wavelength lines and an isolation resistor. For high-frequency applications, chip resistors with small dimensions are widely used for the isolation resistors. In such cases, the coupling between the two quarter wavelength transmission lines can not be neglected. To avoid unwanted coupling, some measures are taken to lead the designs for PDs [60]-[64]. However, as the analysis in [65] illustrates, the broadband feature can be achieved with ports impedance matching at a relatively wide frequency range by controlling the coupling between coupled-line. The coupled-line PD can provide a filtering response compare to PDs with conventional transmission lines. In addition, owing to the coupled-line structure, the width and spacing of the microstrip lines are reduced, thereby resulting in the miniaturisation of circuit width. Since the first coupled-line Wilkinson PD has been proposed in [66], there has been a worldwide interest to develop more versatile components by using this method.

The PD in [67] utilises the coupling between transmission lines to enhance the bandwidth, reducing the size of a convention Wilkinson PD. The two transmission lines of the conventional Wilkinson PD are placed apart to avoid coupling between them, as unwanted coupling will lead to diminished performance. However, for the design in [67], the two transmission lines are close to each other because the coupling is a part of the impedance matching network.

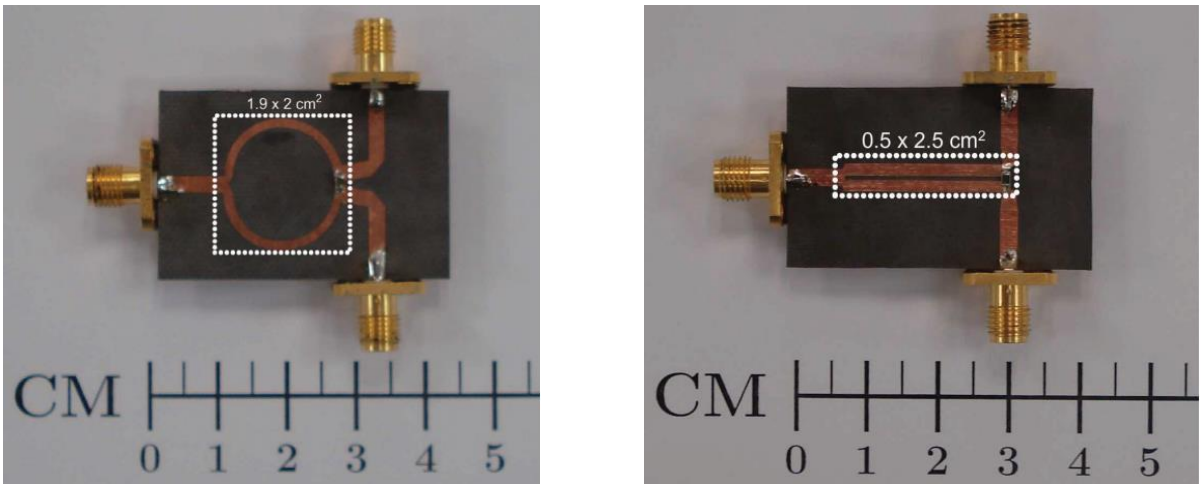

(a) (b)

Fig. 2. 7 Fabricated PDs of (a) conventional and (b) coupled-line design for a gap of 0.56 mm.

Fig. 2. 7 exhibits the size comparison between a conventional Wilkinson PD and coupled-line PD, and the size of the latter is a quarter of the former. The measurement results in **Fig. 2. 8** indicate that the proposed design achieves slightly wider S_{11} bandwidth compared to the conventional Wilkinson one. The circuit is analysed by using even- and odd-mode analyses. The odd-mode impedance of the transmission line Z_0 will only change the matching output ports while not affecting the matching condition for the input port. The 20-dB S_{11} bandwidth is 1.45:1, and S_{22} and S_{33} are 2.08:1 which shows little improvement to the conventional Wilkinson one. The bandwidth improvement is limited as only one coupled-line section is used as shown in **Fig. 2. 8**(a)**.** It should be noted that the isolation S_{23} and output return loss S_{22}/S_{33} have visible shifts from the centre frequency. This is because the odd-mode impedance Z_0will change along with the frequency, which degrades the matching of the output ports. The frequency shift can be mitigated by adding more lumped elements and transmission lines between the output ports. This design shows the potential of the coupled-line method to change the impedance matching at ports.

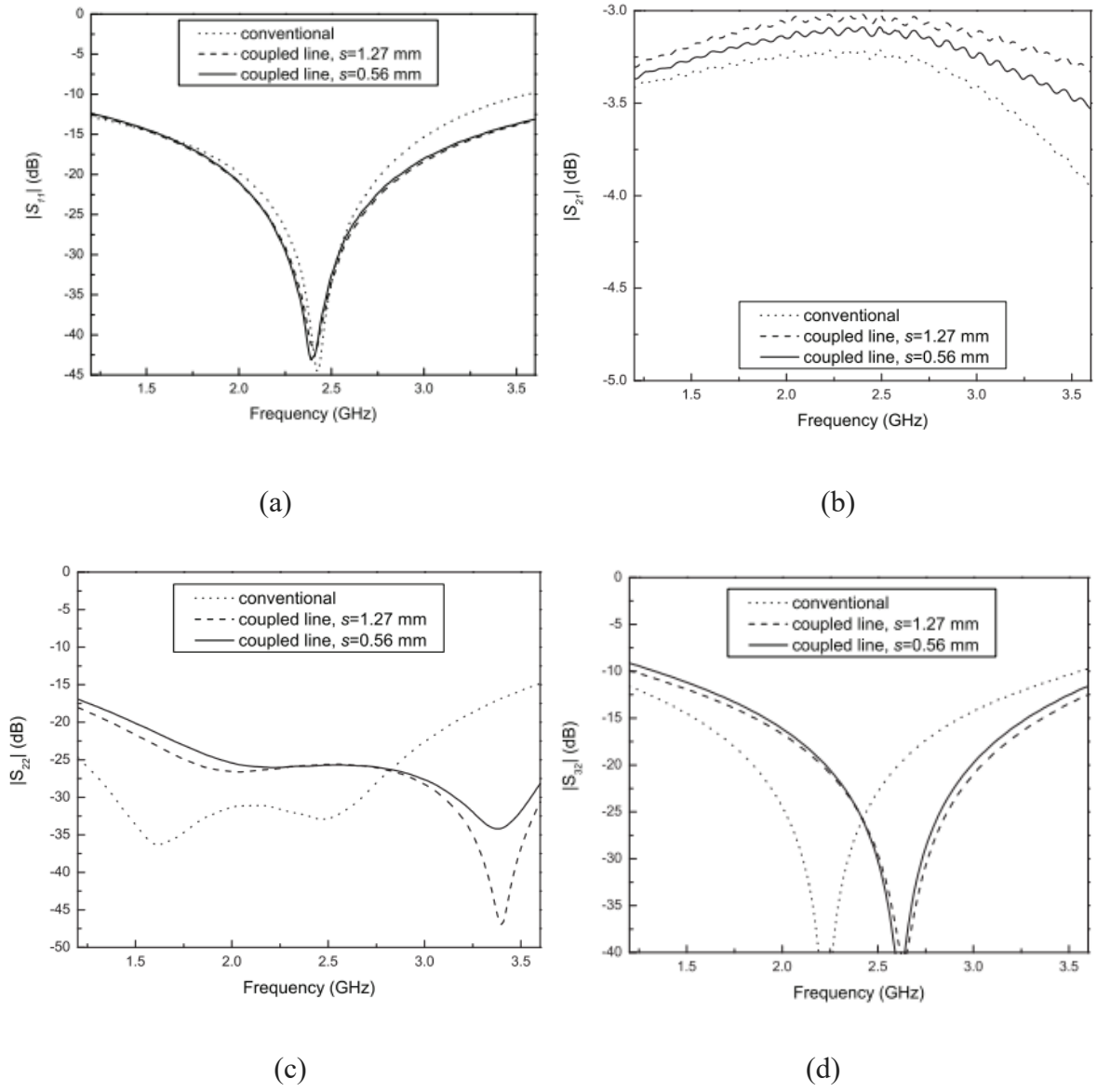

Fig. 2. 8 Measured (a) S_{11}, (b) S_{21}, (c) S_{22}, and (d) S_{23} comparing to the conventional Wilkinson PD [67].

2.1.3 Hybrid and Multi-Functional Wideband PDs

As the basic design in [67] can only produce small improvements in terms of bandwidth, more technologies are expected to be combined to provide better performance such as wider bandwidth and higher out-of-band selectivity. A better-designed case is presented in [68] as shown in **Fig. 2. 9**(a), connecting coupled-line and stepped-impedance stubs to the conventional Wilkinson PD. From **Fig. 2. 9**(a) (b), this design utilises a pair of quarter-wavelength coupled lines that are located between one side of the resistor and the outputs. In

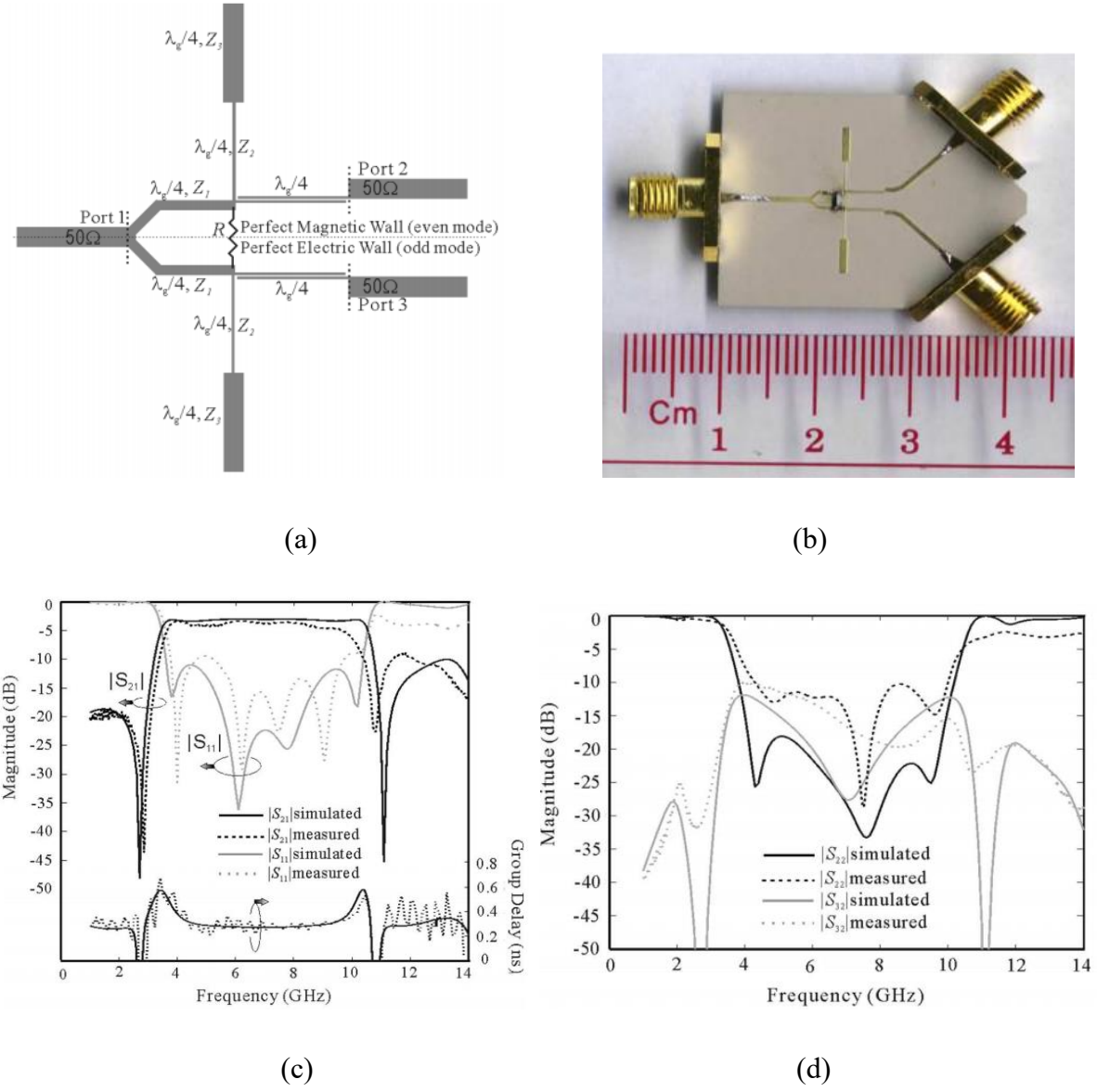

Fig. 2. 9 (a) Schematic of proposed Ultra-wideband PD and (b) fabricated circuit. Simulation and measured comparison of (c) S_{11}, S_{21}, and (d) S_{22} & S_{23} [68].

addition, a pair of stepped-impedance open-circuited stubs and parallel coupled lines are introduced to the output ports. As a result, four additional transmission poles can be generated. Thus, impedance matching can be achieved in the overall ultra-wide band range if these poles are properly allocated. The work can achieve a 3.4:1 13-dB bandwidth corresponding to a bandwidth from 3.1 GHz to10.6 GHz which is relatively wide for PDs designed in X-band. The advantages of the design are the simple structure (only one segment of Wilkinson divider), the sharp and controllable reflection-zeros on S_{21} band edges, and the relatively wide frame.

Moreover, the isolation can be sufficient without adding more lumped elements to the isolation circuit. However, this design requires a large area (four quarter-wavelength × two quarter-wavelength) which will consume more energy, especially in the higher frequency bands.

A multi-functional, ultra-wideband PD using coupled-line is reported in [69]. This design proposed a two-way dual-section PD with three pairs of coupled lines as shown in **Fig. 2. 10**. This filtering PD can realise multiple properties, including good in-band return loss, high isolation, good harmonic suppression, ultra-wide isolation frequency band, and ultra-wide stopband. In **Fig. 2. 10**(a) (b), the quasi-coupled lines are composed of one transmission line and three coupled lines for power splitting. By shifting the isolation circuit Z_{iso} to the right-hand side of the middle-coupled line, a broad isolated bandwidth between two output ports can be observed. Also, with a weak–strong–weak coupling scheme and low impedance of the middle-coupled line, the adopted quasi-coupled lines would result in a wide stopband. Furthermore, unlike the shifted isolation band in [67], the work in [69] has already improved the output ports matching by connecting the resistor R and the capacitor C in series. A reflection zero would appear in the passband so that there would be conspicuous isolation. The open and short stubs are used for harmonic suppression. Consequently, with the assistance of open and shorted stubs, available passband frequencies at the input port can be significantly increased and the isolated frequency band between two output ports can be broadened.

A design guideline is provided; by determining the centre operating frequency, the length of coupled lines can be confirmed and then the even- and odd-mode impedances of coupled lines can be calculated accordingly. Finally, a formula concludes the total impedance of the isolation circuit; by substituting all design parameters of coupled lines, the impedance Z_{iso} can be calculated as a complex number while the real part is the resistance and the imaginary part can be capacitance in the isolation circuit. Overall, as shown in **Fig. 2. 10**(c) (d) the design exhibits a 15-dB bandwidth of 3.2:1 and a stop bandwidth of 3.04:1. This design not only successfully demonstrates a wideband response for operating band, but also realizes an ultra-wide stopband (4.5GHz to 14.5 GHz). It is worth noting that the fabricated circuit is very

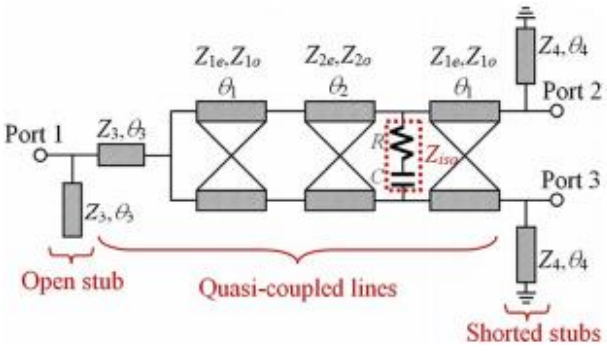

(a)

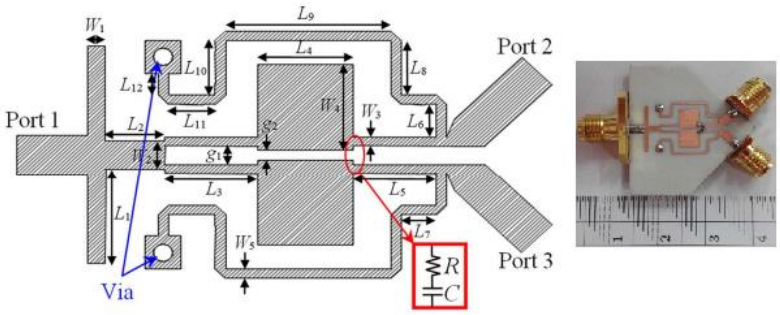

(b)

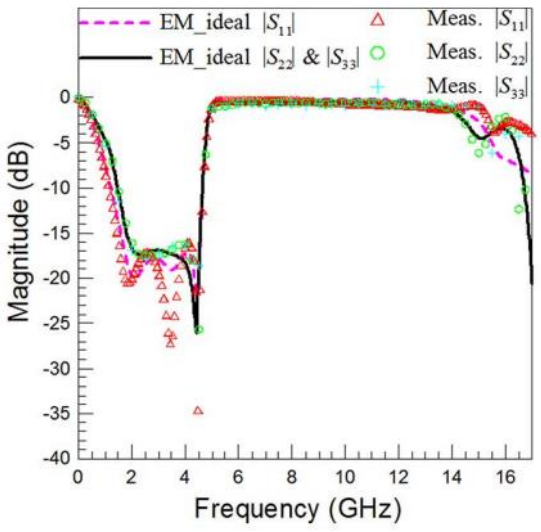

(c)

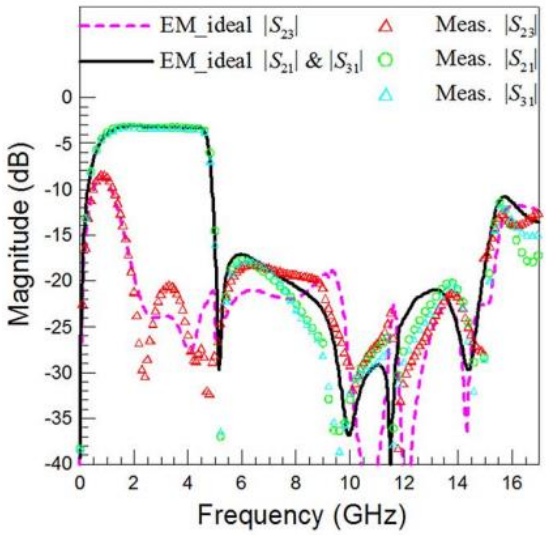

(d)

Fig. 2. 10 (a) Schematic and (b) fabricated circuit of the proposed wideband filtering PD, simulation and measured results of (c) S_{11}, S_{22} and S_{33}, (d) S_{21}, $S_{31}$and S_{23} [69].

compact ($0.2\lambda_g$ x $0.15\lambda_g$) compared to other works with similar performance. Normally, compact size is referring to the circuit that the longest dimension is shorter than *N* quarter wavelengths ($N \times 0.25\lambda_g$, *N* is the order of the circuit) at the centre operating frequency. This type of multi-functional work is desired in many applications to replace filters.

2.2 Reconfigurable PDs

If a system requires changing operating frequencies but not very wideband performance, then reconfigurable PDs are desired. Reconfigurable PDs are capable of selecting the frequencies by adapting a tuning process. The multi-standard or self-adapted systems require tunable PDs or reconfigurable PDs. The tunability of a PD mainly focuses on two aspects; one is the power division ratio, and the other is operating frequencies.

2. 2. 1 Tunable Power Dividing Ratios

Plenty of applications such as antenna feeding networks and power amplifiers prefer small PDs with highpower division ratios. These applications propose several challenges for PDs with different dividing ratios. One is that the circuit is expected to be compact, and the arbitrary power division ratio is best to fit in multi-standard communication systems. Typically, there are three common methods to achieve unequal power division ratios, namely the uneven-impedance method, the phase-modification method, and the hybrid method. The uneven-impedance method is based on the notion that more power is passed through the path with smaller impedance. Tuning the charateristic impedances of each ouput port will then achieve the desired power division ratio easily. However, changing the characteristic impedances will lead to extremely narrow or wide transmission lines, which are difficult to fabricate. The second method, tuning the phase of the transmission lines instead of impedance, is easier. Moreover, this method is capable of constructing high power division ratios. The third method, a hybrid, is where the phase and impedance of the transmission line is modified simultaneously. To realize single-band PDs with various functions, such as equal/unequal power splitting and tunable power splitting ratio, conventional three-line coupled structure has been widely utilised. The work in [68] shows a two-way PD with arbitrary power division as shown in **Fig. 2. 11**(a) (b)**.** The hybrid method is used in this design. A quarter-wavelength three-line coupled structure

is employed. One terminal of the central coupled-line is connected to the input port, whereas the other terminal is grounded. The two coupled sidelines are connected to the output ports, whereas an isolation resistor connects the other ends. The power division ratios can be tuned by altering the capacitance of two centrally connected varactors. Adding capacitors between coupled lines can affect the odd-mode impedance of the circuit and tuning the capacitance of the varactors will further change the odd-mode impedance and phase velocity simultaneously. There are two bias circuits applying voltages to two varactors; the bias circuits come with L biases and C blocks connected to prevent short circuit. The results in **Fig. 2. 12**(a)-(c) show a tunable power division ratio from 1:1 to 2.4:1 with more than 15 dB of isolation and 10 dB of return loss across the frequency band from 0.7 to 1.4 GHz.

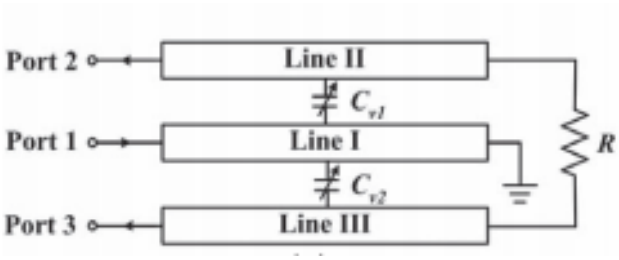

(a)

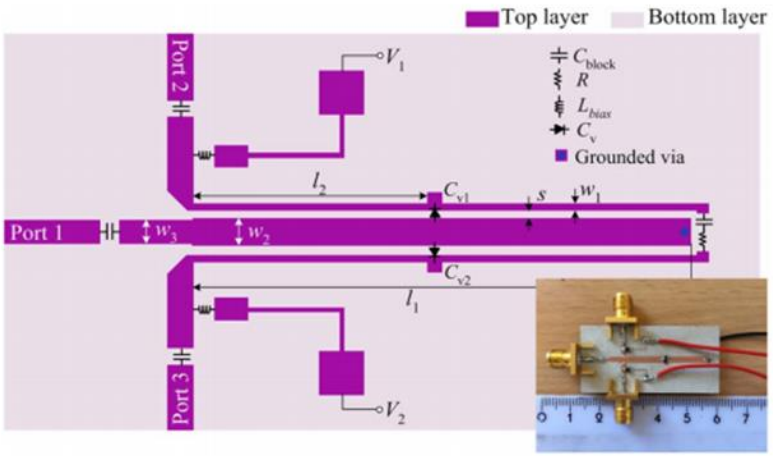

(b)

Fig. 2. 11 (a) Tri-coupled line structure, (b) layout and photography of the proposed tunable PD [70].

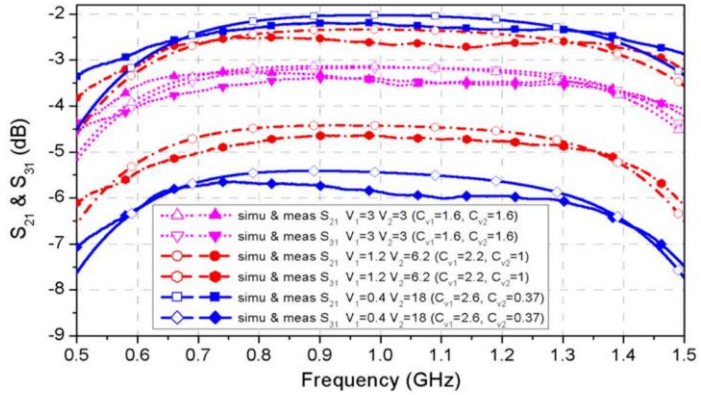

(a)

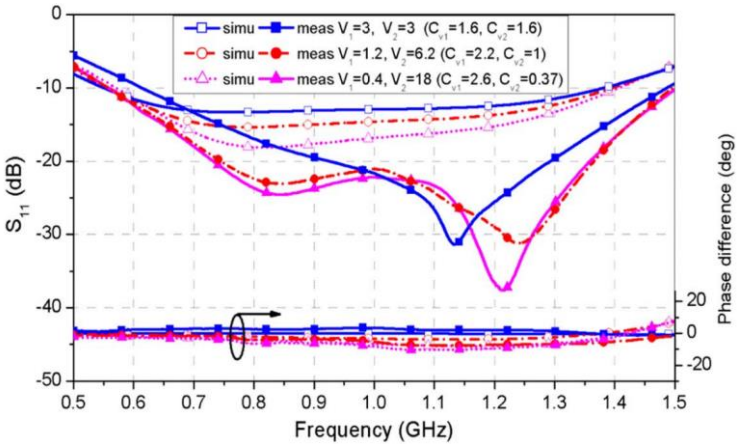

(b)

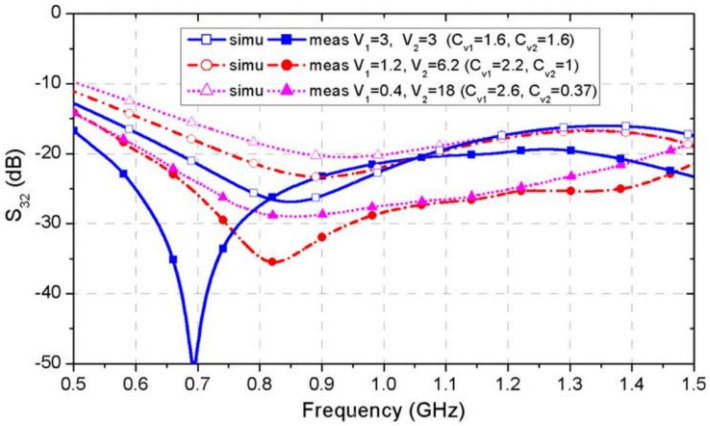

(c)

Fig. 2. 12 Measured (a) S_{21} and S_{31}, (b) S_{11} and the phase difference between output ports, (c) S_{23} [70].

2. 2. 2 Tunable Operating Frequency

Similar to the tunable power division, from the reconfigurable operating frequency point of view, the most commonly used method is adding varactors to change the ports impedance matching. The tunability results from the impedance/phase velocity change of the coupled or uncoupled lines.

Fig. 2. 13(a) (b) show the configuration and layout of the PD in [71]. Adapting a stepped-impedance transformer on the common arm, a pair of coupled lines, and a shunt varactor is connected at the common node for tunability. An approximate solution for impedance Z_3 and Z_{4e} is given in the paper under the condition of θ_3 is small, and the sum of θ_3 and θ_4 approaches θ_2. According to **Fig. 2. 14**(a)-(d), this work achieves a wide tuning band of 2.89:1 considering all *S*-parameters better than 20-dB. This tuning band range is extensive in relation to its compact size ($0.24\lambda_g \times 0.02\lambda_g$). However, as mentioned in the paper, the bandwidth is not constant; with the change of centre frequency, the lowest return loss will turn up after 2 GHz, resulting in the bandwidth shrink with a 20-dB standard. Although this study exhibits a very wide tuning range, the main drawback is putting the isolation circuit between the closely spaced coupled-line. Moreover, the realization of physical isolation between two outputs requires two 50Ω transmission lines which increases circuit size. Integrating filtering response into a PD as shown in **Fig. 2. 15**(b) is effective for system simplification. For instance, a PD and tunable filter combined in the same front-end can be merged as shown in **Fig. 2. 15**(a), resulting in a multi-functional but simply component with no extra loss.

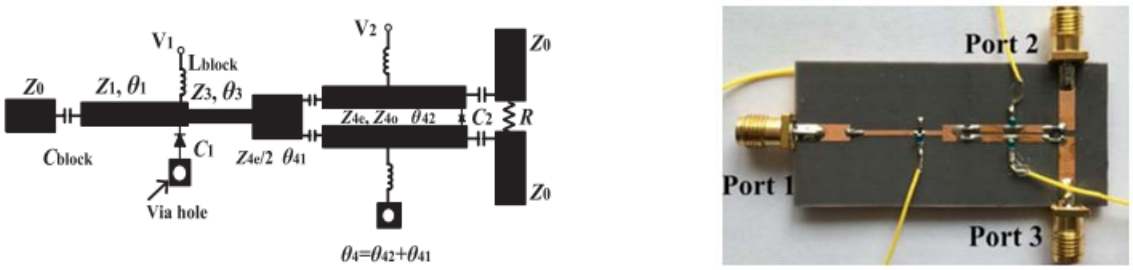

(a) (b)

Fig. 2. 13 (a) Configuration and (b) fabricated circuit of the PD.

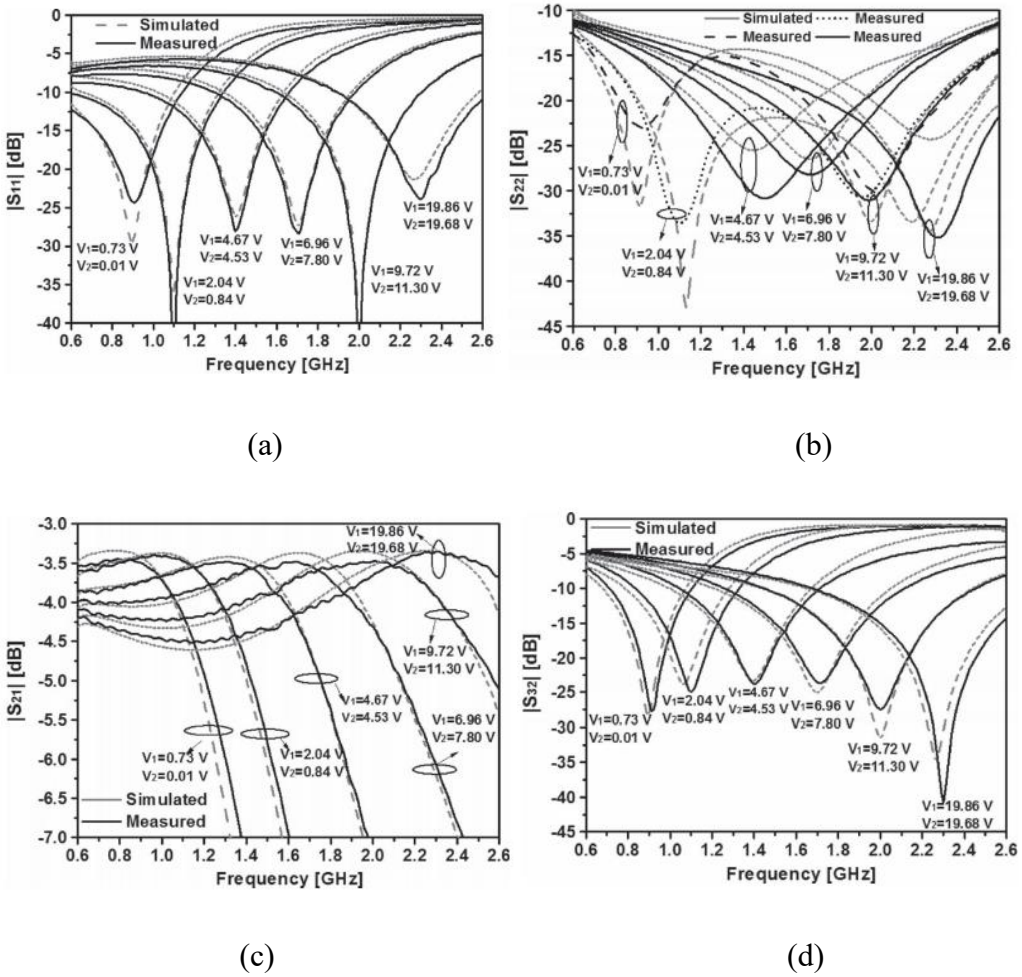

Fig. 2. 14 Comparison of simulated and measured (a) S_{11}, (b) S_{22}, (c) S_{21}, and (d) S_{32}.

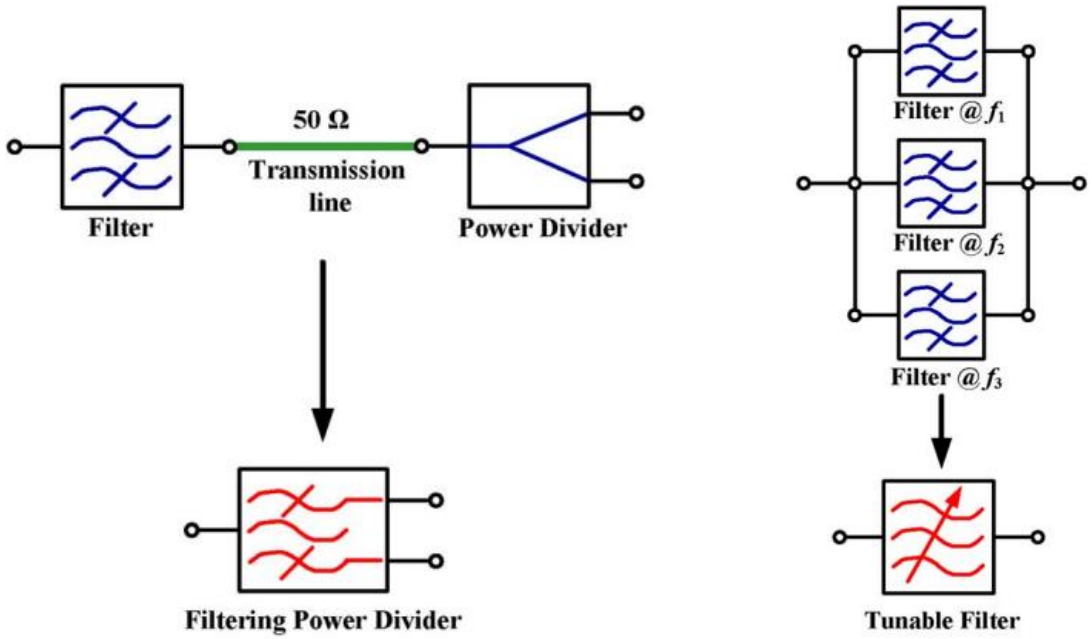

Fig. 2. 15 (a) Cascaded a filter and a PD to form a filtering PD, and (b) multiple bandpass filter to form tunable bandpass filter.

Research study [72] utilises the synthesis of coupled-resonator filters to produce a tunable PD with filtering response. The art of this method is that tuning the varactors will only affect the resonating frequencies, while the coupling coefficient and quality factors do not change. In other words, the centre operating frequency will be changed by altering varactors, but the bandwidth will be ideally kept constant. Since tunable filters with constant bandwidth have become a popular trend, the same mechanism can be applied to design PDs.

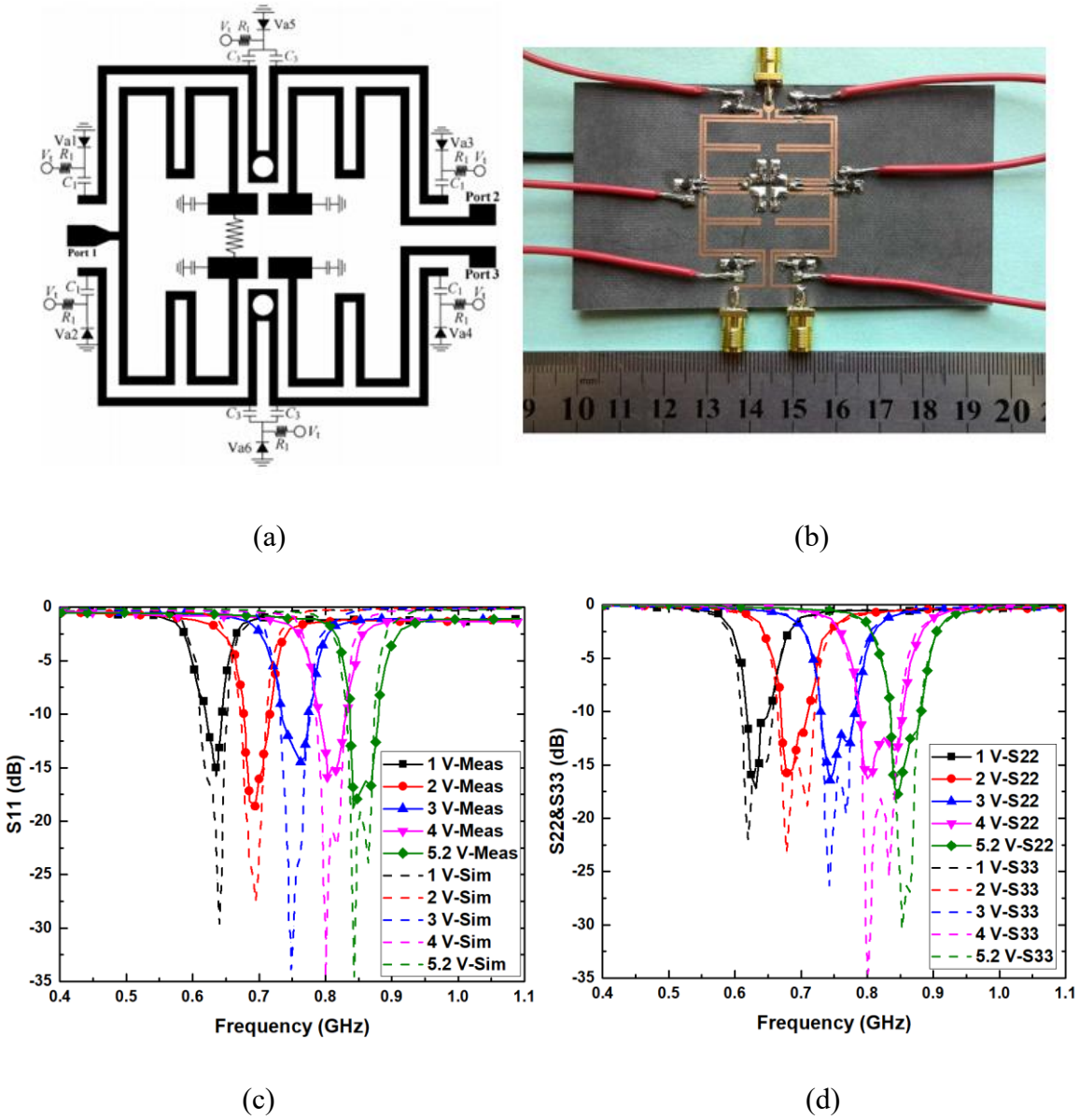

Fig. 2. 16 (a) Configuration and (b) fabricated circuit of the proposed PD in [72], and comparison of measured and simulated performances regarding (c) S_{11}, and (d) S_{22} & S_{33}.

The configuration of the PD is shown in **Fig. 2. 16**(a) (b). Methods of controlling the coupling coefficients and external quality factors are investigated, and the constant bandwidth is complimented by using capacitors as well as magnetic and electric coupling to obtain required external quality factors and coupling coefficients. A constant bandwidth is maintained when tuning the frequency. The performance is shown in **Fig. 2. 16**(c) (d) with the frequency tuning range from 0.62 to 0.85 GHz (1.37:1) with an absolute bandwidth of 60$\pm$2.5 MHz. Since the

frequency tuning range is not very wide, this method is suitable for applications that require the same absolute bandwidth in a small tuning range.

2. 2. 3 Hybrid Reconfigurable PDs

The word "hybrid" indicates multiple reconfigurable responses, including operating frequency tuning, operating bandwidth tuning, and power division tuning, all implemented at the same time.

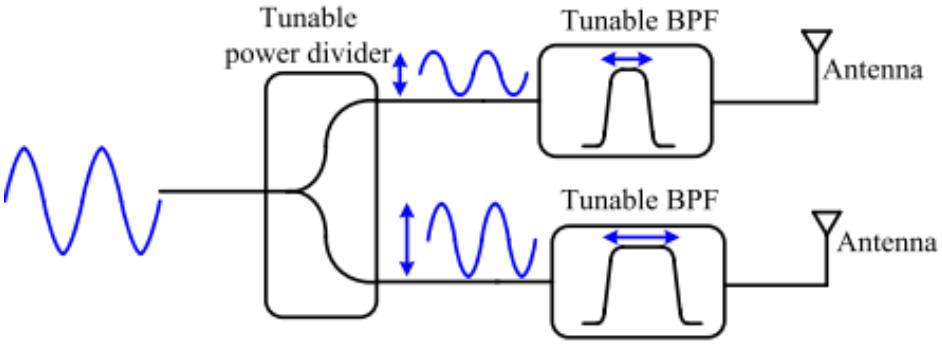

Fig. 2. 17 Reconfigurable RF front end with tunable power dividing and controllable filtering for antennas.

For example, in a reconfigurable RF front end, as shown in **Fig. 2. 17**, a tunable PD and two tunable bandpass filters are usually cascaded. The tunable PD can control the power dividing ratios for each output terminals, while the tunable filters can control the spectrum of the transmitting signals to eliminate interferences. To simplify the system and avoid unnecessary transmitting loss, hybrid reconfigurable PDs are very attractive. However, so far a reconfigurable wideband filtering PD having a simultaneous frequency, bandwidth, and power division control is less explored.

The design in [73] proposed a wideband in-phase PD with tunable power division ratio and filtering response as depicted in **Fig. 2. 18**(a) (b). The design consists of a three-line coupled structure loaded with a pair of varactors in between a pair of short-ended stubs at two outputs. A variable power division is achieved by changing the coupling factors between the centre-line and side-lines of the three-line coupled structure using a pair of varactors. The centre frequency

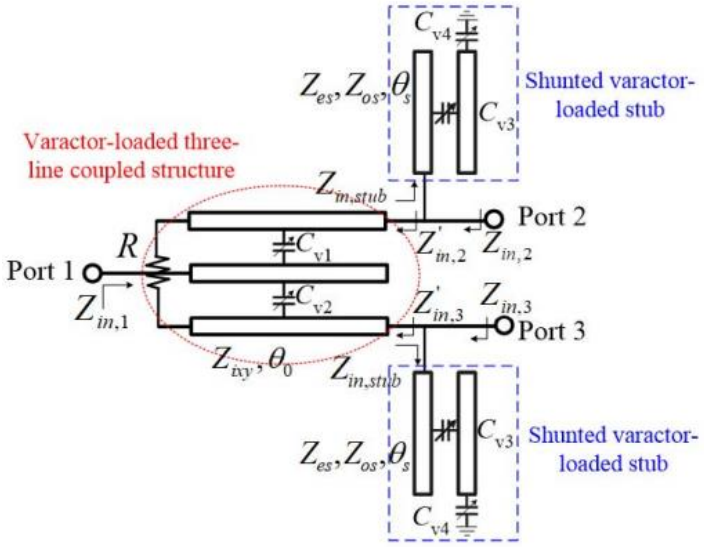

(a)

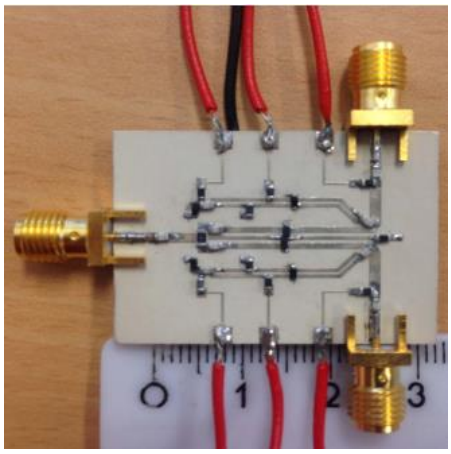

(b)

Fig. 2. 18 (a) From cascaded structure to an integrated tunable filtering PD, (b) proposed design configuration, and (c) fabricated circuit ($0.24\lambda_g \times 0.12\lambda_g$) for [73].

and corresponding operating bandwidth are tuned by the varactors; one at the centre of the loaded short-ended stub, and another one connecting the end of the stub to the ground. The power division ratio is a function of capacitances. Once the mode impedance and loaded varactors are defined, the power division ratio can be controlled easily by the two varactors between the three coupled-line.

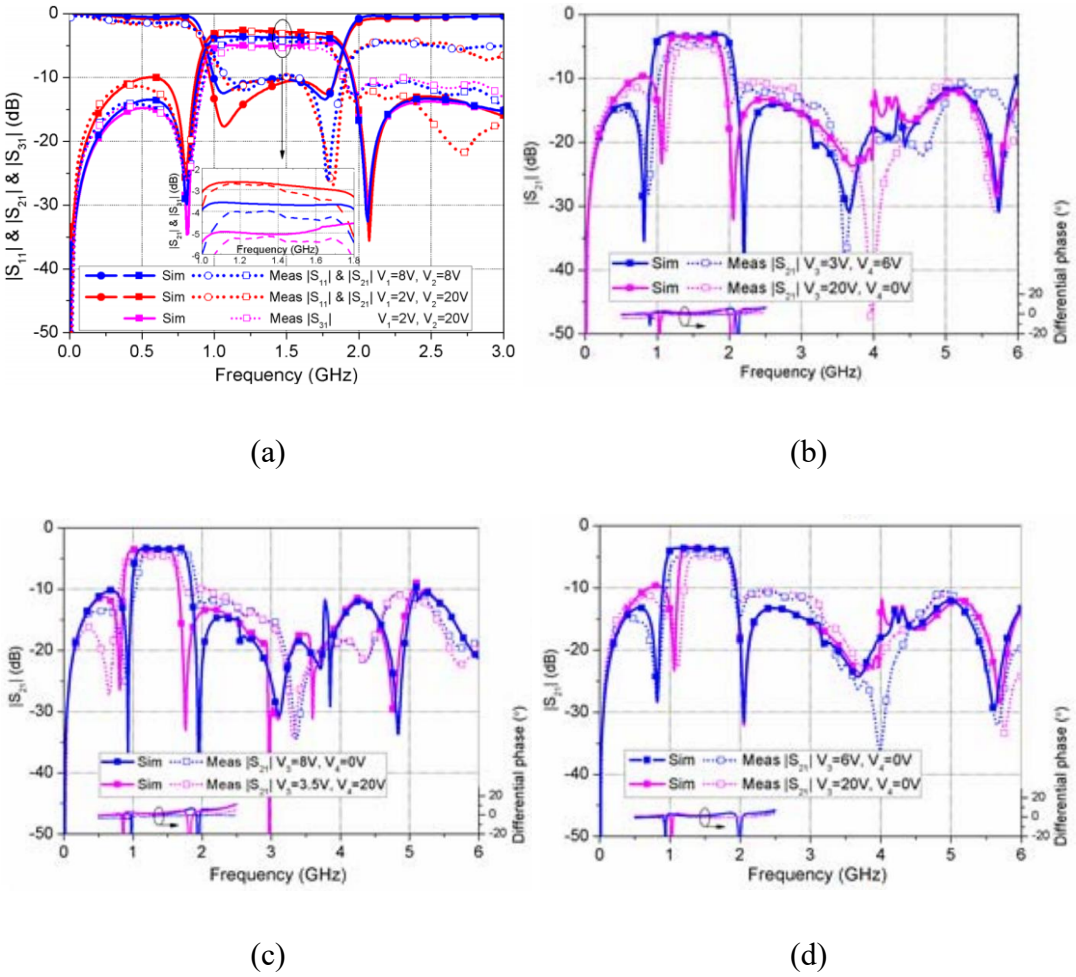

Fig. 2. 19 Simulations and measurements results for demonstrating (a) different power division ratio, (b) bandwidth tunability, (c) centre frequency tunability, and (d) cut-off edge tunability and in-band differential phase of [73].

To investigate the filtering response, the loaded varactors are kept at the same value. A series of transmission zeros that located at harmonic frequencies $2f_0$, $4f_0$ to $2nf_0$ (n = 1, 2,.) are generated due to the three-line coupled structure. Similar to the two-line structure, reflection-zeros result from the cancellation of phase at these frequencies. Moreover, more transmission zeros can be produced by the shunted varactors loaded at the short-ended stubs. The bandwidth and the centre frequency of the tunable filtering band highly depend on the position of transmission zeros. In the experiment of [73], the bandwidth tuning range achieved 1.29:1 to 2.2:1 as shown in **Fig. 2. 19**(a)-(d), which is substantial. For the isolation circuit analysis, the mutual coupling between the two side lines is extremely weak, and the equivalent capacitances

of the coupled lines do not vary significantly from their values at the centre frequency. Therefore, the isolation remains almost the same under equal or unequal power division ratio.

To sum up, the proposed design has a controllable filtering bandwidth, relocatable cut-off zeros, and tunable centre frequency. The Tunability of power division ratio ranges from 0.5:1 to 2:1; controllable filtering bandwidth from 1.42:1 to 1.92:1; tunable centre frequency from 1.3 to 1.48 GHz; sharp cut-off with relocatable transmission zeros; and upper stopband harmonic suppressions up to more than 6 GHz in the whole measurement process. The experimental performance is slightly different from the simulated one due to the nonlinearity of the tuning elements as well as losses in fabrication and measurements processes.

It is noted that the tunability of the centre frequency comes from the shunted varactor-loaded stubs, while the resonant modes are related to both three-line coupled structure and shunted stubs. This is the reason why the tunability of the centre frequency is limited to some extent. This design can serve a range of narrowband to wideband applications where the tunability of the bandwidth is more significant than that of the centre frequency.

Similar work using the same method is reported in [74]; the structure and tuning mechanism is the same as shown in **Fig. 2. 20**(a) (b). The circuit consists of two tri-mode stub-loaded resonators, a three-line coupled structure loaded two varactors, and two output parallel-coupled lines loaded a lumped capacitor. The centre frequency and operating bandwidth of wideband filtering response can be tuned by controlling the varactor diodes loaded onto the open end of tri-mode resonators. Meanwhile, the power division ratio is controlled by tuning the coupling strength between the centre line and two side-line of three-line coupled structure. The capacitor loaded onto the parallel-coupled line of two output ports is to enlarge the coupling between them, which can increase the return loss S_{11}, and then can relieve the limitation of the line space between two coupled lines. The advance of [74] over [73] is the wider centre frequency tuning range, from 0.86 GHz to1.32 GHz. However, the occupied area for this design is slightly larger than [73].

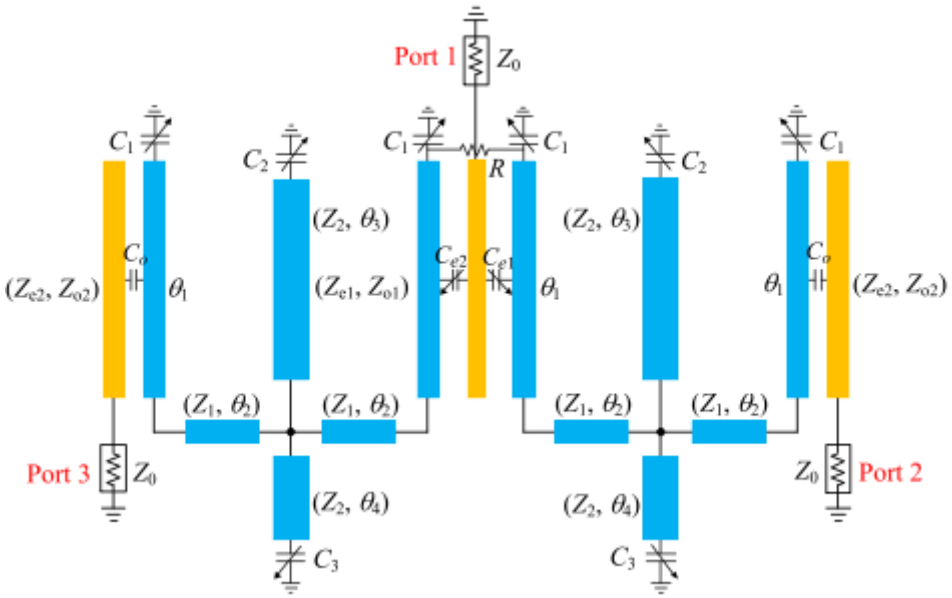

(a)

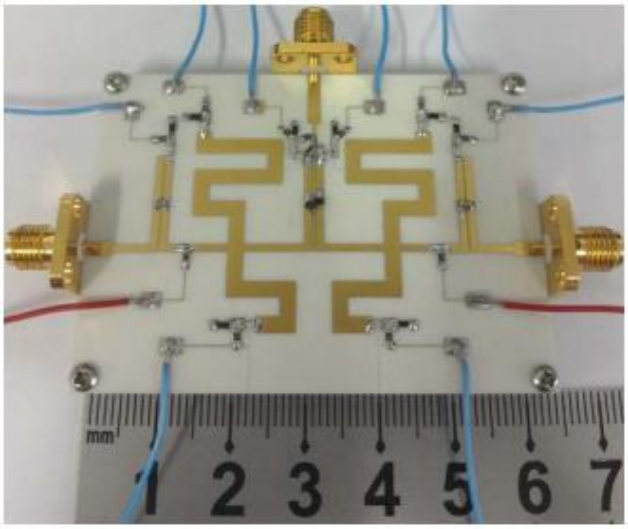

(b)

Fig. 2. 20 (a) Circuit model of reconfigurable wideband filtering PD and (b) fabricated circuit for [74].

2.3 Coupled Resonator PDs

Resonant-coupled PDs exhibit a great prospect in communication systems due to the compact size, harmonic suppression [75] [76], and high passband selectivity [77]. The quarter-wavelength sections of a conventional Wilkinson PD can be replaced by coupled resonators to reduce circuit size [78]. Furthermore, the critical resonant coupling condition between resonators will only be achieved at certain frequencies, contributing the harmonics suppression. Cross-coupling between the resonators will introduce transmission zeros. If the introduced transmission zeros are located at the end of the passband, the transition between the passband and the stopband will be sharpened. The selectivity of the passband can be enhanced by increasing external coupling between resonators. Some design examples in terms of size miniaturization and passband selectivity enhancement are discussed in this section. The work in [79] has demonstrated a compact PD design with a filtering response using spiral resonators. The spiral resonators are utilised for miniaturisation due to its curled structure. The coupling scheme of the PD is shown in **Fig. 2. 21**(a).

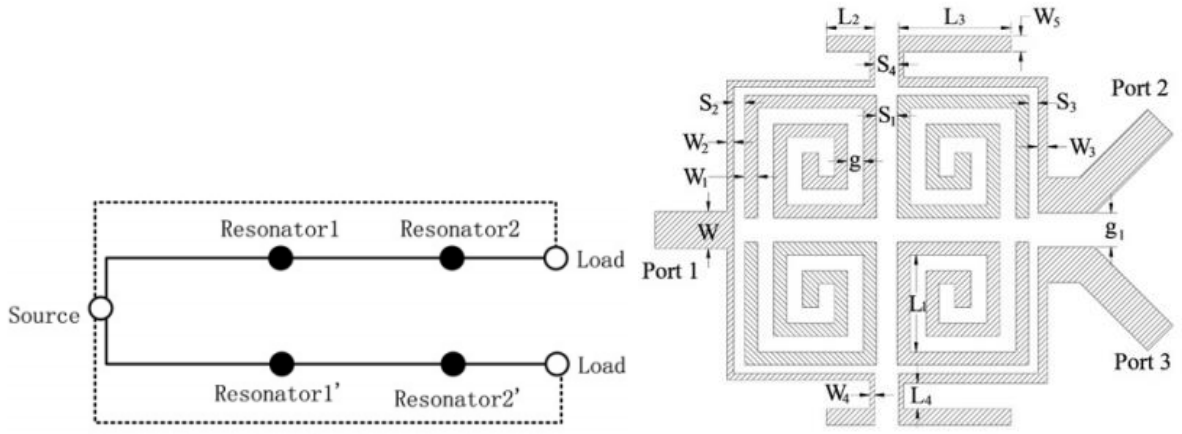

(a) (b)

Fig. 2. 21 The (a) coupling scheme, and (b) the structure of the in-phase PD in [79].

The source-load cross-coupling is employed to create a pair of transmission zeros on both ends of the passband. The PD is composed of four half-wavelength spiral resonators. Signals transmitted from input will be split into two ways directly by the T-shape feedlines (represented

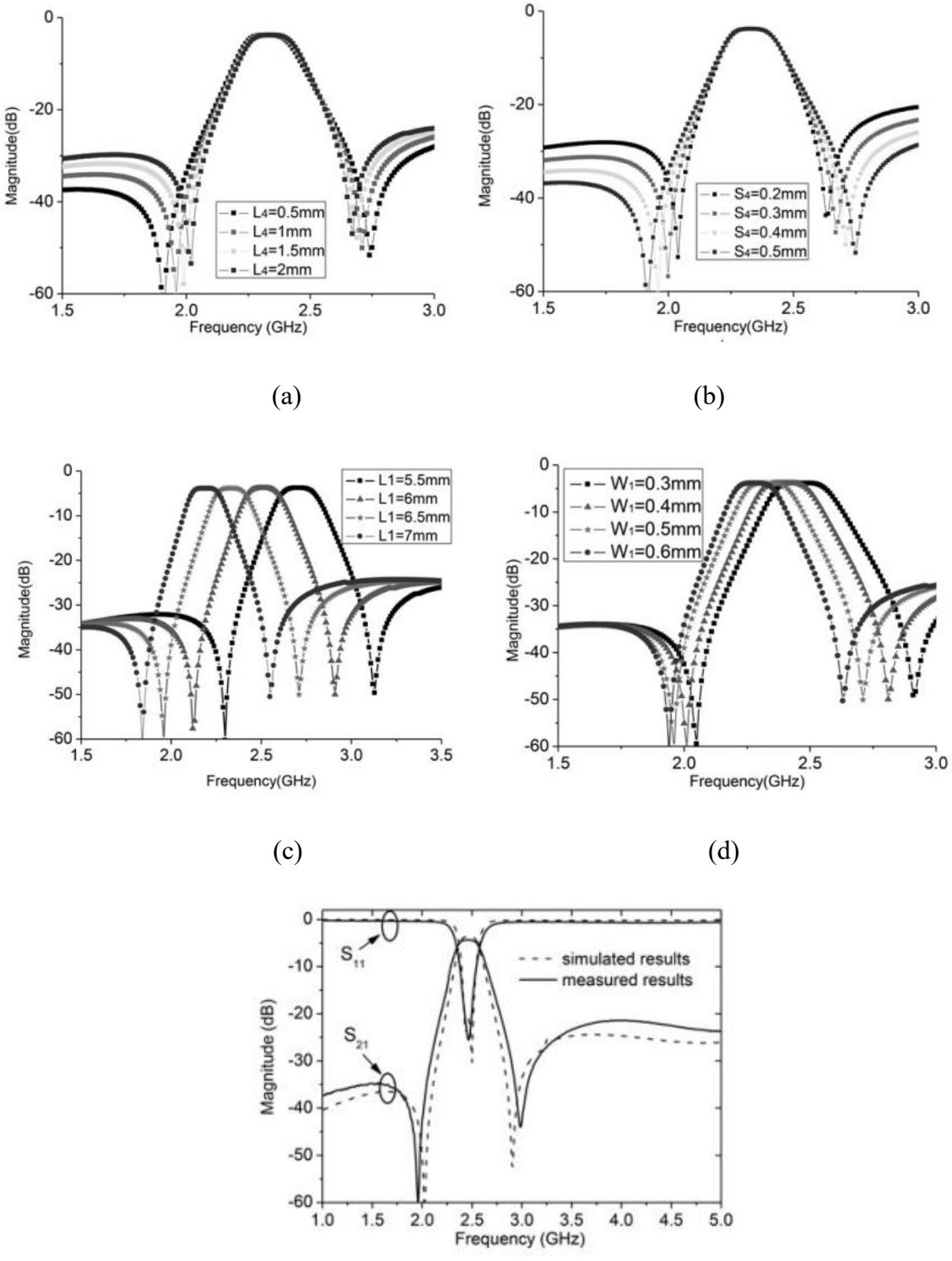

Fig. 2. 22 Selective band-edge regarding (a) L_4 and (b) S_4, and tuning frequency band regarding (c) L_1, and (d) W_1, (e) comparison of simulated and measured results [79].

by the dash lines in **Fig. 2. 21**(a)). The feedlines will couple with the two pairs of spiral resonators as shown in **Fig. 2. 21**(b). It is suggested in [79] that this type of resonator-coupling scheme can provide strong operating-passband enhancement around the resonant frequency. In addition to filtering response and high selectivity, the passband and the two transmission zeros can be controlled by properly choosing the lengths and gaps of the resonators. A comprehensive demonstration of the frequency responses with varied coupling stength can be seen in **Fig. 2. 22**(a)-(e). The transmission zeros can be controlled by changing the gaps between two input/output feedlines, as shown in **Fig. 2. 22** (a). The variation of the gap widths will change the source-load cross-coupling conditions. Higher selectivity can be achieved by enhancing the cross-coupling strength. The pictures in **Fig. 2. 22**(c) (d) illustrate that the centre frequency of the passband can be tuned by changing the width and length of the spiral resonators. The dimension of the resonators determines the resonant frequency so that leads to a change of centre frequency. The measured results of the PD in **Fig. 2. 22**(e) show good agreement with simulations. The fabricated circuit is a second order PD with a compact size of 0.15 $\lambda_g \times 0.3\ \lambda_g$. However, the isolation between the output ports is relatively poor due to the cross-coupling between each port.

A compact and high in-band isolation resonator-based PD with a second-order Chebyshev filtering response is proposed in [80]. The coupling scheme is shown in **Fig. 2. 23**(a). The size can be reduced by modifying the structural frame of the quarter-wavelength unit-impedance resonators. The traditional unit-impedance resonator shown in **Fig. 2. 23**(b) can be evolved into the net-type resonator with two open-ended stubs and two shorted-ended stubs. For further miniaturization, the net-type resonator is folded to a square box shape where the size is approximately $0.09\lambda_g$ by $0.09\lambda_g$. Moreover, the electric and magnetic coupling can be easily achieved due to the configuration of the resonator. It should be noted that the coupling coefficient M_{34} in **Fig. 2. 23**(a) is realised by the magnetic coupling, while the others are realized by the electric coupling. Herein, the electric coupling can be realised when the open-ended line sections of two folded net-type resonators are closely placed, and the magnetic coupling can be achieved if the short-ended line sections of two folded net-type resonators are closely allocated. The proposed coupling scheme is symmetric with respect to the two output ports. When an incident signal is applied at output Port 2, the signal will be evenly split into two out-of-phase parts. These two parts can cancel each other at output Port 3 and thus no

power is coupled to Port 3. This results in enhanced in-band isolation. The measurement results in **Fig. 2. 24**(a) (b) depict a narrow bandwidth of input return loss with only 1.036:1 at the centre frequency. The measured results show very good in-band isolation, which is better than 30 dB. It should be mentioned that the circuit has an extremely compact size of $0.19\lambda_g \times 0.19\lambda_g$ which was achieved by curving quarter wavelength transmission lines into spiral resonators. An in-band performance deterioration is obtained, which might be caused by fabrication and measurement errors.

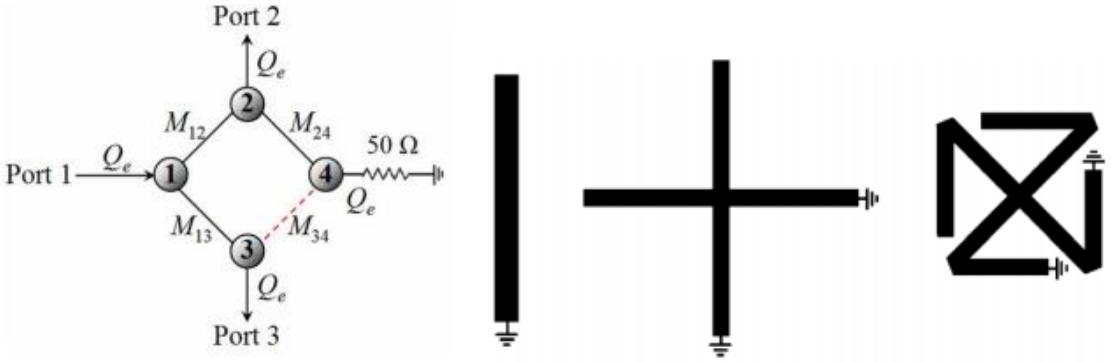

(a) (b)

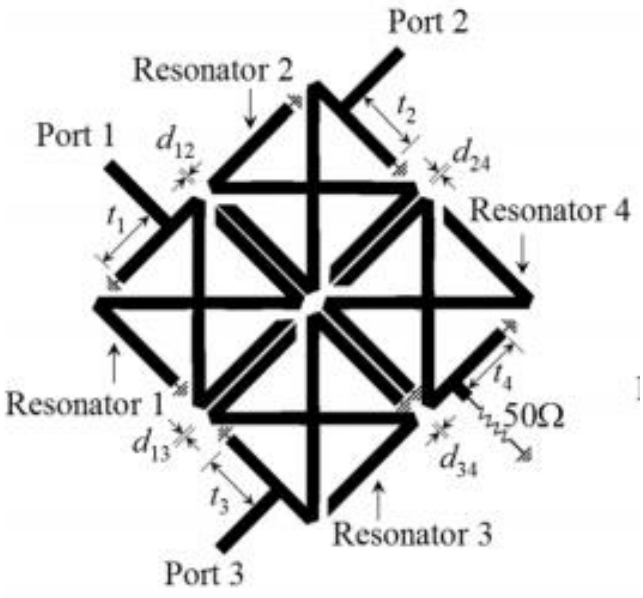

(c)

Fig. 2. 23 (a) Coupling scheme of the PD in [80], and the (b) quarter-wavelength unit-impedance resonator, and the (c) configuration of the PD in [80].

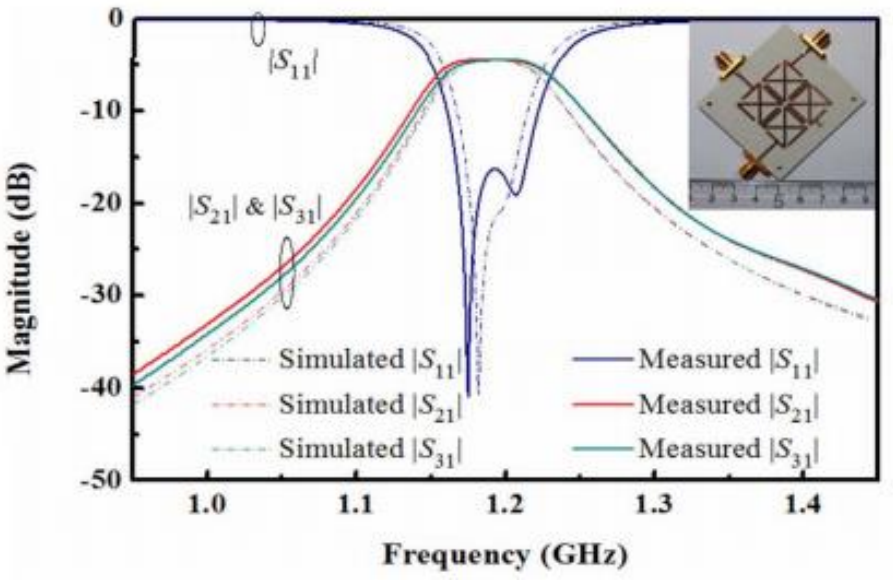

(a)

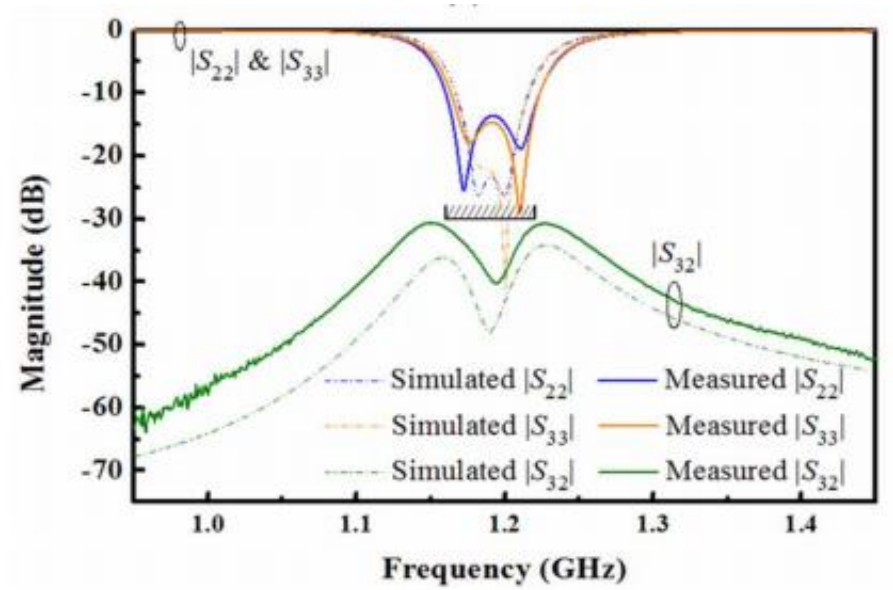

(b)

Fig. 2. 24 Comparison of simulation and measurement in terms of (a) $|S_{11}|$ and $|S_{21}|$, and (b) $|S_{22}|$, $|S_{33}|$ and $|S_{23}|$.

In general, resonator-based PDs exhibit remarkable features such as compact sizes, high passband selectivity, and harmonic suppression. These features are realised by using the coupling mechanism between the resonators. The majority of the resonator-based PDs have

these characteristics and as a result possess filtering responses. The resonator-based PD design methods can be borrowed from filter designs. However, the isolation performance highly depends on the coupling scheme.

2.4 Millimetre-Wave PDs

Millimetre-Wave (mm-Wave), as indicated by the name, has a frequency that ranges from 30 GHz to 300 GHz with such a small wavelength. Mm-Wave devices were exotic and only been used as specialised applications such as military space. As low-frequency bands have been assigned to numerous wireless communication systems and the number will subsequently keep growing, high-frequency bands are becoming increasingly attractive and necessary. Mm-Wave bandwidths have long been employed for military radar systems and are frequently being used in commercial automotive collision-avoidance radar systems. Achieving mm-Wave circuit designs on reliable Printed Circuit Boards (PCB) materials in a practical manner will be the challenge in making these higher frequencies affordable.

Several Design Examples

1) Microstrip

A novel Monolithic Hybrid Microwave Integrated Circuit mm-Wave PD/combiner was proposed in [81]. A ring PD/combiner was used, and it was integrated on a ceramic substrate. The structure showed in **Fig. 2. 25**(a) enhances the traditional Wilkinson design by adding two half-wave transmission lines to connect the integrated resistor, converting the layout in a ring circuit of $1.5\lambda_g$ length. These additional lines create the ideal framework for this isolation resistor, reducing undesirable mutual coupling between the main transmission arms. The measured transmission magnitudes that are less than 3.5 dB which can be seen from **Fig. 2. 25**(b), while the overall imbalance is less than 0.25 dB. Also, from **Fig. 2. 25**(c) the matching of all ports is less than -15 dB, and the measured isolation factor between the two output ports is at least 25 dB. Overall, this work shows an outstanding performance, but the bandwidth is relatively narrow.

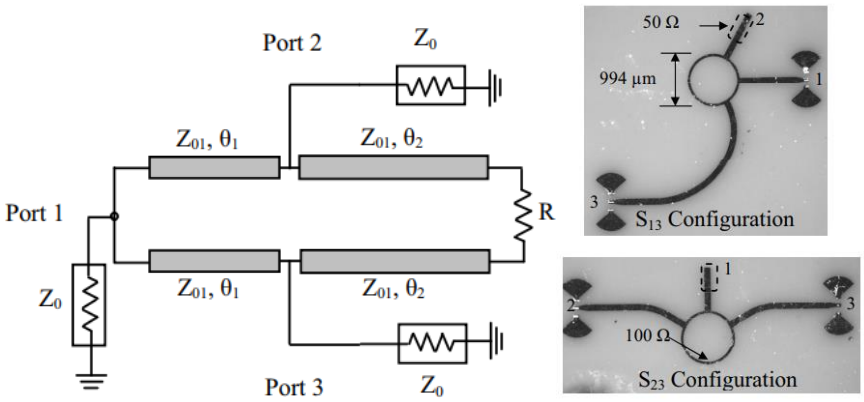

(a)

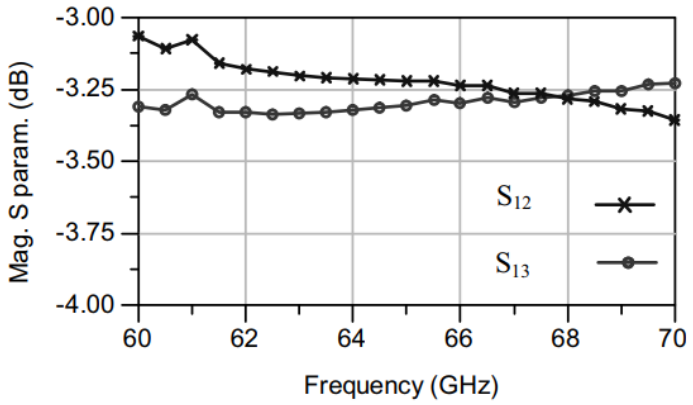

(b)

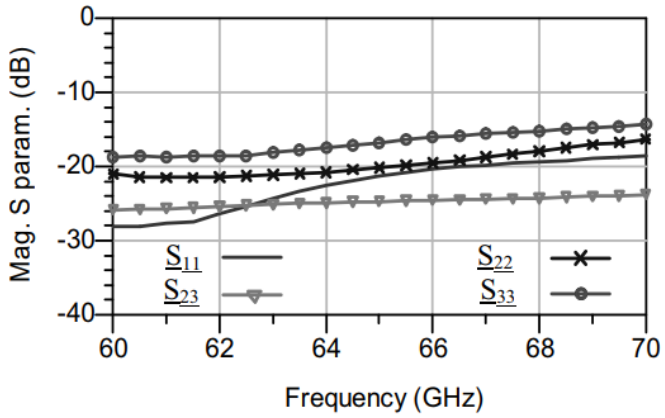

(c)

Fig. 2. 25 (a) Modified Wilkinson PD and micro-photographs of the PD in [81], and measured results of (b) transmission, and (c) return losses and isolation.

2) Substrate Integrated Waveguide

Since the conventional microstrip structure will cause incredible energy loss in mm-Wave frequencies, Substrate Integrated Waveguide (SIW) technology may be one of the solutions. Traditional metallic waveguides exhibit excellent properties in designing high frequency, high Q, and deficient loss devices. As modern communication systems require lightweight and miniaturized components, one of the main drawbacks for metallic waveguide is the massive size, which involves complex transitions to integrated planar circuits. The transitions always consist of two or more separate pieces that need accurate assembly, and a tuning mechanism is also generally essential. Furthermore, the planar substrate has to be cut into a specific shape. These constraints make integration difficult and costly. The concept of integrated microstrip and rectangular waveguide in planar form was firstly proposed by D. Deslandes and K. Wu [82]. A basic SIW structure is shown in **Fig. 2. 26**: the rows of metallised via holes form the electrical side walls, while the substrate is in between the top and bottom metal plates to allow propagation of TE modes. This form of the waveguide will inevitably reduce the factor of the waveguide due to dielectric filling and volume reduction. However, the entire circuit, including planar circuit, transition, and waveguide can be constructed using standard PCB or other planar processing techniques. In other words, SIW converts 3D bulky metallic waveguides to planar ones and preserves the advantages of conventional waveguides.

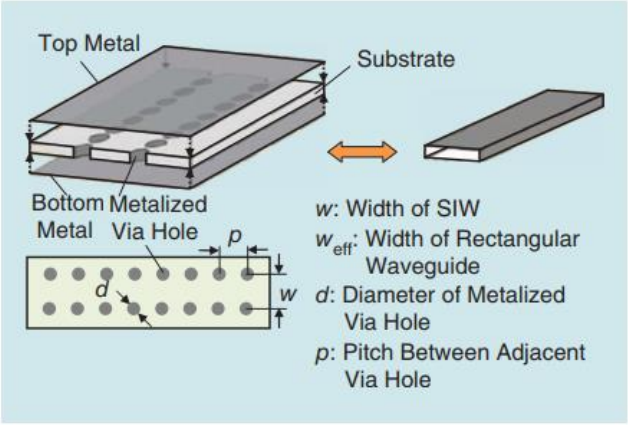

Fig. 2. 26 Structure of SIW and its equivalent rectangular waveguide.

The SIW has recently become very popular for the design and development of high-performance and cost-sensitive filters over a very large frequency range from sub-gigahertz to sub-terahertz. Plenty of works [83]-[86] have focused on designing SIW filters with smaller

sizes and better performances. The mechanism of designing a PD is similar to a filter; energy is transmitted to outputs within assigned frequency bands. Many SIW PDs [87]-[91] have been proposed, but few of them concentrated on mm-Wave applications. The design in [92] reported a broadband H-plane Wilkinson PD that makes use of the half-mode substrate integrated waveguide (HMSIW) technique for the first time (see **Fig. 2. 27**(a)). This broadband PD utilizes the half-mode structure of SIWs to achieve a half-size reduction. In addition, the lossy network or resistor branch is integrated with the SIW structure in order to obtain good output matching and isolation if unbalanced signals are combined or divided.

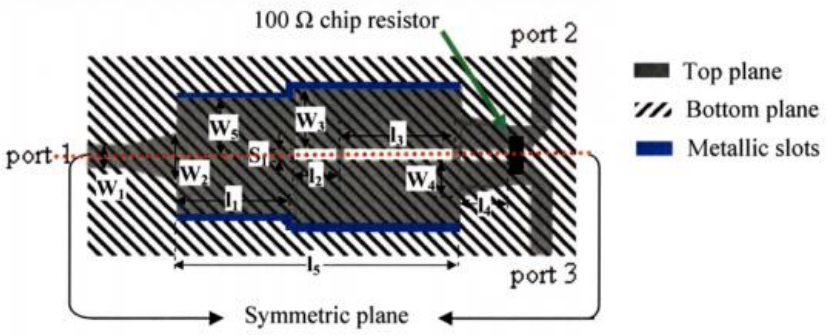

(a)

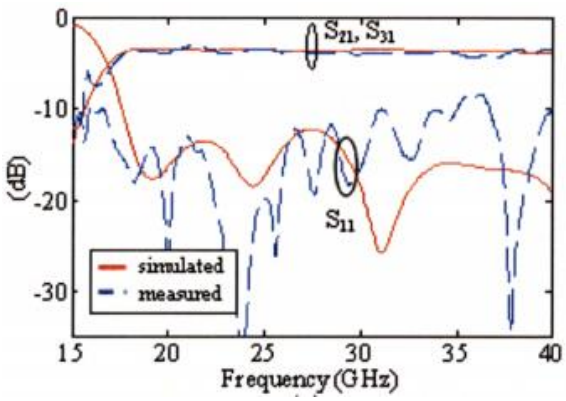

(b)

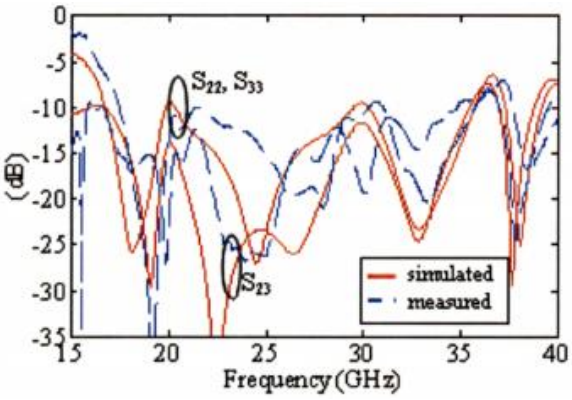

(c)

Fig. 2. 27 (a) A prototype of the proposed HMSIW PD, and simulations and measurements for (b) S_{11}, S_{21} and S_{31}, and (c) S_{22}, S_{33} [92].

The design takes the advantages of SIW, such as low profile, low insertion loss, and little interference, however the resulting structure becomes smaller in size. It should be noted that the half-mode configuration does not support higher-order mode TE_{20} as in the case of SIW.

Therefore, a broader bandwidth is another side product of the proposed PD in contrast with its counterparts. The proposed PD can easily be used at mm-Wave frequencies and favourable for the microwave integrated circuit applications. Measured results in **Fig. 2. 27**(b) (c) suggest that good input return loss S_{11} and S_{21} and S_{31} performances can be achieved across a broad bandwidth from 18 GHz up to 40 GHz. Meanwhile, S_{22}, S_{33}, and S_{23} better than 10-dB are also ensured across a 1.94:1 bandwidth from 18 GHz to 35 GHz. However, the design is critical for power combining or non-equal power dividing due to the potentially poor output port matching.

3) Coplanar Waveguide

Several works [93]-[95] focus on the design of a conventional Wilkinson PD using coplanar waveguides. The circuit consists of four quarter-wave coupled lines that are cleverly connected in a ring configuration as shown in **Fig. 2. 28**.

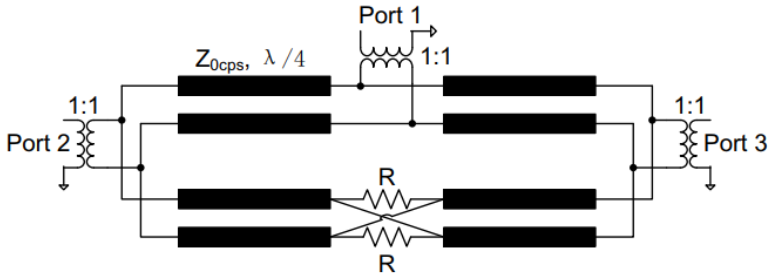

(a)

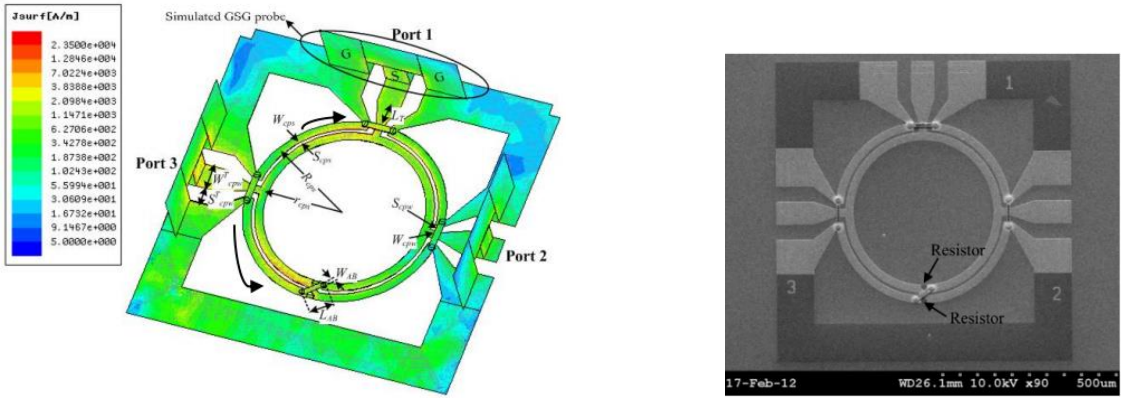

(b)

Fig. 2. 28 (a) Simplified schematic of the coplanar ring divider [91], (b) Simulated surface current flow at 80 GHz.

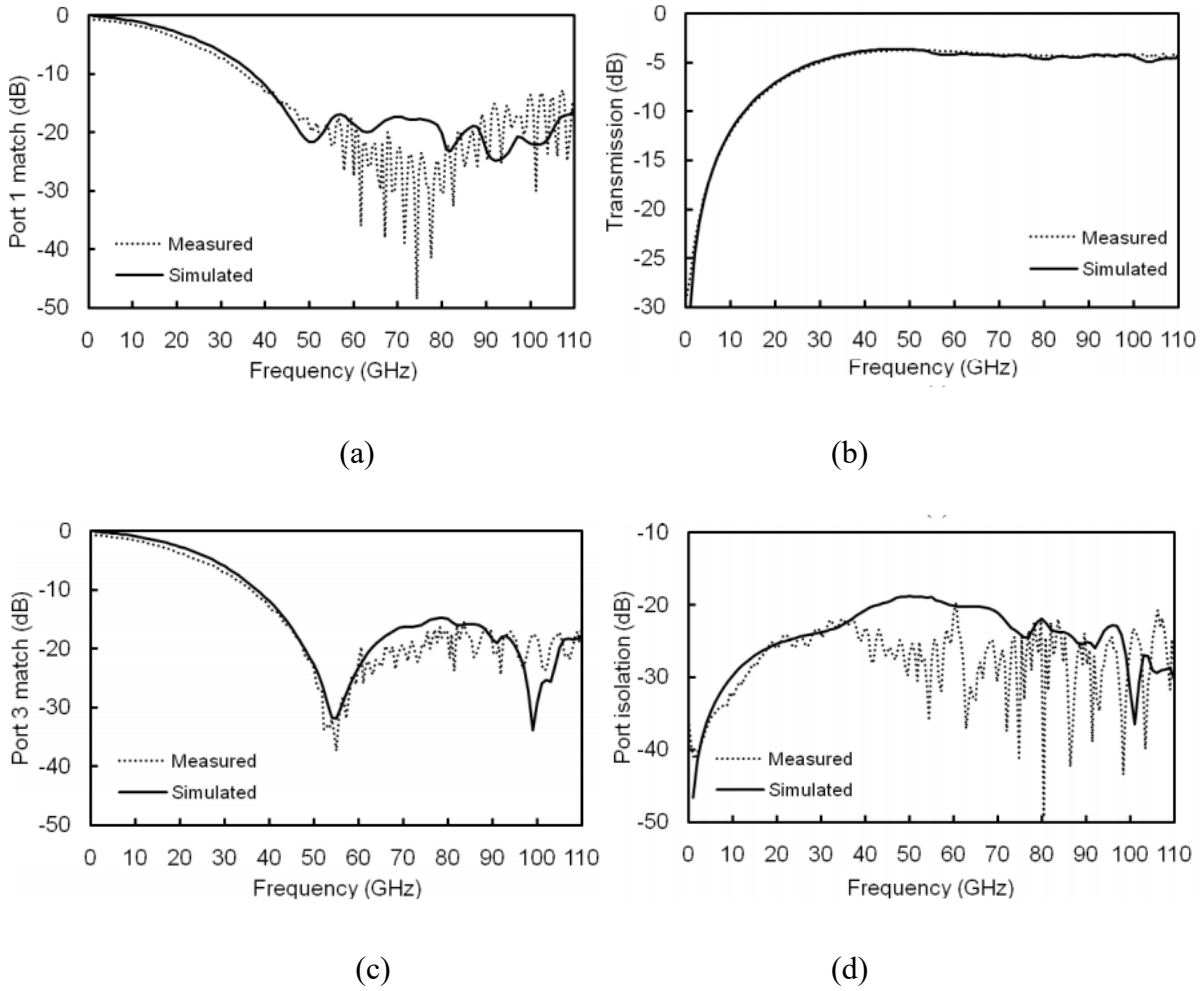

Fig. 2. 29 Measured results compared with Simulations of (a) S_{11}, (b) S_{21}, (c) S_{33} and (d) S_{23}.

The design is uniplanar and was fabricated on a thick GaAs substrate. The isolation resistor was formed by using 33 nm thick of NiCr to give approximately 50 Ω/square. The air-bridge connecting the ground planes of the CPW and the symmetric CPS crossover is used to prevent odd-mode generation. Unlike the conventional Wilkinson divider, which has a pair of lumped resistors, the proposed divider has two quarter-wave symmetric CPSs, a coplanar stripline crossover, and a pair of 100 Ω resistors between the two output ports. The crossover forms a phase inverter, which provides 180º non-frequency selective phase inversions; the two quarter-wave CPSs ensure an open-circuit at the output port when looked into the other ports. The divider is thus expected to have broadband isolation performance. The two resistors provide a good port matching comparing to conventional Wilkinson PDs. The measurements in **Fig. 2. 29**(a)-(d) indicate a transmission loss lower than 1.3 dB and S_{11} better than 15 dB. The S_{23} is

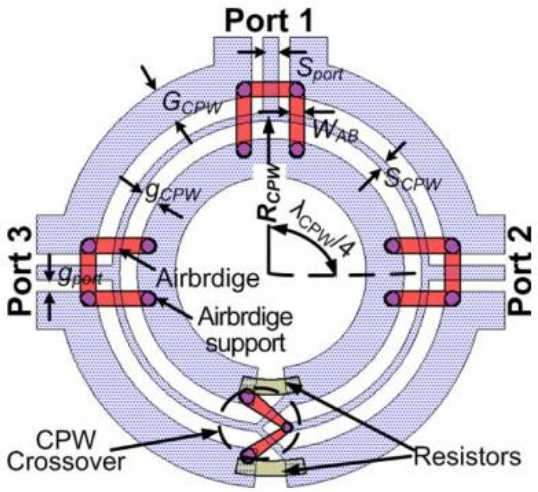

(a)

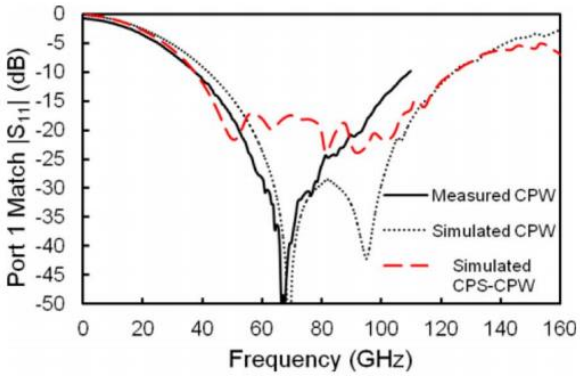

(b)

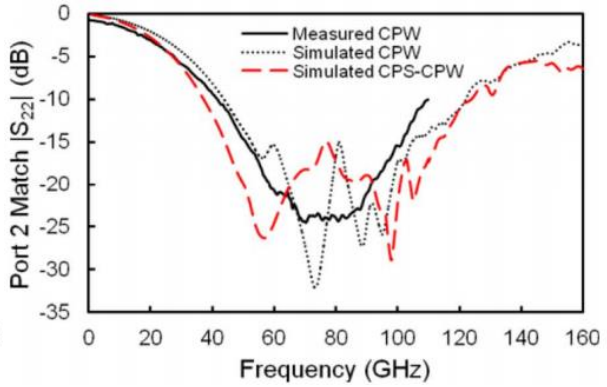

(c)

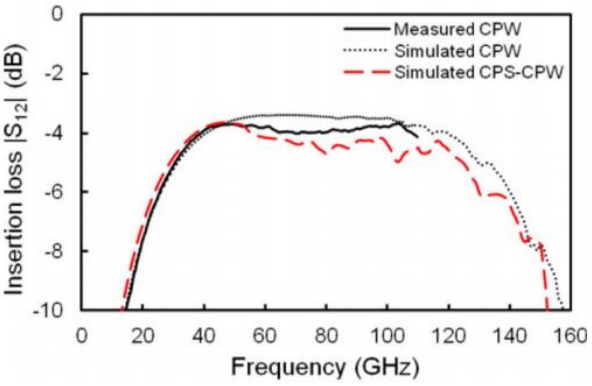

(d)

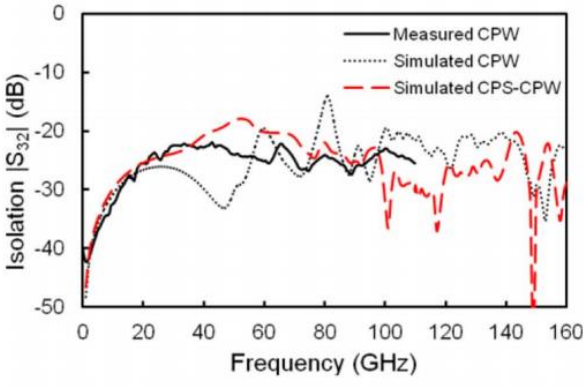

(e)

Fig. 2. 30 (a) Structure of CPW ring PD and (b) S-parameters simulation and measurement comparison of (b) S_{11}, (c) S_{22}, (d) S_{S21} and (e) S_{23} [95].

kept below 18-dB in the entire V and W bands. The performance is comparable to the devices that used at lower frequencies, and the fabrication process is more straightforward compared to studies at similar bands. Similar work has been conducted in [95]. A wideband CPW power combiner is shown in **Fig. 2. 30**(a) using two upper quarter-wave CPWs and two lower quasi quarter-wave CPWs with an impedance of 70.7 Ω. Compared to [93], this structure avoids high insertion loss caused by CPW and CPS transitions.

Experimental results in **Fig. 2. 30**(b)-(e) indicate less than 0.8 dB transmission loss (less than 0.5 dB from simulation may cause by the transition of CPWs and ports). S_{11} and S_{22} are greater than 15 dB, and S_{23} is better than 22 dB in the frequency range of 50 and 100 GHz. The results have demonstrated that even in such high frequencies, efficient wideband power dividing and combing can be achieved by using standard GaAs MMIC process and air-bridges.

2.5 Summary

This chapter has presented and discussed a large amount of state-of-the-are PDs from conventional prototypes to multi-functional PDs. Different aspects of PD's performance are discussed in this chapter including operating bandwidth, power division and frequency selectivity, etc. Normally, a variable bandwidth and power dividing ratio and broad frequency selective range are desired. However, the circuits will have high complexity and larger size when pursuing good performance. In this case, realizing excellent performance while maintaining small electrical size and simply layout is a challenge for PD design. In addition to performance, abundant functionality is the other remarkable challenge. Engineers always facing specifications that require PD to have multi-function. In general, versatility is implemented by cascading different components which sacrifices transmission efficiency. Multi-functional PDs can integrate power dividing with filtering response. Besides, RF components at mm-Wave frequencies have attracted more and more attention and can be extensively investigated due to the promising applications in modern wireless communications. Maintaining promising performance and avoiding unnecessary loss at mm-Wave frequencies are also very challenging.

The work to be presented in **Chapter 3** has remarkable operating bandwidths by using a variable form of a conventional Wilkinson PD. It exhibits excellent performance with a simply

layout. Comparing to other similar work presented in this chapter, the proposed design can achieve a wider bandwidth but the size is less than 2/3 of that of a conventional PD. The design in **Chapter 4** based on a Horst-type Wilkinson power divider can provide a great frequency tuning range. Thus, high frequency selectivity and a simple structure are implemented at the same time. The proposed design in **Chapter 5** can be applied at mm-Wave frequencies. Additionally, the proposed coupling strategy can provide filtering response and get rid of T- or Y- junction at the common port for loss reduction. This design integrates good performance, multi-function and low loss together at the same time. The proposed design method has a great potential for the development of various mm-Wave components.

References

[1] E. Wilkinson, "An N-way hybrid power divider," *IEEE Trans. Microw. Theory Thech*., pp. 116-118, 1960.

[2] U. Gysel, "A new N-way power divider/combiner suitable for high power applications," in 1975 MTsymp. Dig., pp.116-118.

[3] Y. Wu, Y. Liu, and X. Liu, "Dual-frequency power divider with isolation stubs,'' *Electronics Letters*, vol. 44, no. 24, pp. 1407-1408, 2008.

[4] Y. Wu, Y. Liu, Y. Zhang, J. Gao, and H. Zhou, "A dual band unequal Wilkinson power divider without reactive components,'' *IEEE Transactions on Microwave Theory and Techniques*, vol. 57, no. 1, pp. 216-222, Jan. 2009.

[5] M. Bemani and S. Nikmehr, "Nonradiating arbitrary dual-band equal and unequal 1:4 series power dividers based on CRLH-TL structures,'' *IEEE Transactions on Industrial Electronics*, vol. 61, no. 3, pp. 1223-1234, Mar. 2014.

[6] N. Gao, G. Wu, and Q. Tang, "Design of a novel compact dual-band Wilkinson power divider with wide frequency ratio,'' *IEEE Microwave and Wireless Components Letters*, vol. 24, no. 2, pp. 81-83, Feb. 2014.

[7] M. Liao, Y. Wu, Y. Liu, and J. Gao, "Impedance-transforming dual-band out-of-phase power divider,'' *IEEE Microwave and Wireless Components Letters*, vol. 24, no. 8, pp. 524-526, Aug. 2014.

[8] C. Cai, J. Wang, Y. Deng, and J.-L. Li, "Design of compact dual-mode dual-band filtering power divider with high selectivity,'' *Electronics Letters*, vol. 51, no. 22, pp. 1795-1796, 2015.

[9] X. Ren, K. Song, M. Fan, Y. Zhu, and B. Hu, "Compact dual-band Gysel power divider based on composite right- and left-handed transmission lines,'' *IEEE Microwave and Wireless Components Letters*, vol. 25, no. 2, pp. 82-84, Feb. 2015.

[10] C.-W. Tang and Z.-Q. Hsieh, "Design of a planar dual-band power divider with arbitrary power division and a wide isolated frequency band,'' *IEEE Transactions on Microwave Theory and Techniques*, vol. 64, no. 2, pp. 486-492, 2016.

[11] X. Wang, I. Sakagami, Z. Ma, A. Mase, M. Yoshikawa, and M. Ichimura, "Miniaturized dual-band Wilkinson power divider with self-compensation structure,'' *IEEE Transactions on Components, Packaging and Manufacturing Technology*, vol. 5, no. 3, pp. 389-397, Mar. 2015.

[12] T. Zhang, W. Che, H. Chen, and W. Feng, "A compact four-way dual-band power divider using lumped elements,'' *IEEE Microwave and Wireless Components Letters*, vol. 25, no. 2, pp. 94-96, Feb. 2015.

[13] W. Zhang, Z. Ning, Y. Wu, C. Yu, S. Li, and Y. Liu, "Dual-band out-of-phase power divider with impedance transformation and wide frequency ratio,'' *IEEE Microwave and Wireless Components Letters*, vol. 25, no. 12, pp. 787-789, Dec. 2015.

[14] H. S. Gharehaghaji and H. Shamsi, ''Design of unequal dual band Gysel power divider with isolation bandwidth improvement,'' *IEEE Microw. Wireless Compon. Lett*., vol. 27, no. 2, pp. 138–140, Feb. 2017.

[15] M.-J. Park, ''Coupled line Gysel power divider for dual-band operation,'' *Electron. Lett*., vol. 47, no. 10, pp. 599–601, May 2011.

[16] Z. Sun, L. Zhang, Y. Liu, and X. Tong, ''Modified Gysel power divider for dual-band applications,'' *IEEE Microw. Wireless Compon. Lett*., vol. 21, no. 1, pp. 16–18, Jan. 2011.

[17] M. A. Maktoomi and M. S. Hashmi, ''A performance enhanced port extended dual-band Wilkinson power divider,'' *IEEE Access*, vol. 5, pp. 11832–11840, 2017.

[18] M. H. Maktoomi, D. Banerjee, M. S. Hashmi, "An enhanced frequency-ratio coupled-line dual-frequency Wilkinson power divider", *IEEE Trans. Circuits Syst. II Exp. Briefs.* vol. 65, no. 7, pp. 888-892, July 2018.

[19] R. Gomez-Garcia, R. Loeches-Sanchez, D. Psychogiou, and D. Peroulis, "Single/multi-band Wilkinson-type power dividers with embedded transversal filtering sections and application to channelized filters,'' *IEEE Transactions on Circuits and Systems I: Regular Papers*, vol. 62, no. 6, pp. 1518-1527, Jun. 2015.

[20] Q. X. Chu and F. Lin, "Design of multi-band microstrip power dividers," in Proc. EDAPS, Dec. 2011, pp. 1–4.-

[21] Li, Y.C., Xue, Q., Zhang, X.Y.: 'Single- and dual-band power dividers integrated with bandpass filters', *IEEE Trans. Microw. Theory Techn*., 2013, 61, (1), pp. 69–76

[22] K. Song, Y. Mo, Q. Xue, and Y. Fan, "Wideband four-way out-of-phase slotline power dividers,' *IEEE Transactions on Industrial Electronics*, vol. 61, no. 7, pp. 3598-3606, Jul. 2014

[23] M. M. Honari, L. Mirzavand, R. Mirzavand, A. Abdipour, and P. Mousavi, "Theoretical design of broadband multisection Wilkinson power dividers with arbitrary power split ratio,'' *IEEE Transactions on Components, Packaging and Manufacturing Technology*, vol. 6, no. 4, pp. 605-612, 2016.

[24] W. Feng, H. Zhu, W. Che, and Q. Xue, "Wideband in-phase and out-of-phase balanced power dividing and combining networks,'' *IEEE Transactions on Microwave Theory and Techniques,* vol. 62, no. 5, pp. 1192-1202, May 2014.

[25] M. Strackx, K. Janssen, E. D'Agostino, G. Vandenbosch, P. Reynaert, and P. Leroux, "Ultra-wideband antipodal Vivaldi antenna array with Wilkinson power divider feeding network," in Proc. *IEEE ICUWB*, 2011, pp. 1–4.

[26] Liu, W.-Q., Wei, F., Pang, C.-H., and Shi, X.-W.: 'Design of a compact ultra-wideband power divider'. Int. Conf. Microwave Millimeterwave Tech. (ICMMT), Shenzhen, China, May 2012, pp. 1–3

[27] Zhu, H., Abbosh, A., and Guo, L.: 'Wideband four-way filtering power divider with sharp selectivity and wide stopband using looped coupledline structures', *Microw. Wirel. Compon. Lett.,* 2016, 26, (6), pp. 413–415.

[28] U. Ahmed and A. Abbosh. "Compact power divider for wideband in-phase and out-of-phase performances using parallel coupled lines," *Electronic Letters*, vol: 53, issue: 19. Pp.1312-1314. Spe, 2017.

[29] Packiaraj, D., M. Ramesh, and A. T. Kalghatgi. "Broadband Equal Power Divider." *Journal of Microwaves, Optoelectronics and Electromagnetic Applications* 16, no. 2 (2017): pp. 363-370.

[30] Y. Wu, L. Jiao, Z. Zhuang, and Y. Liu, "The art of power dividing: A review for state-of-the-art planar power dividers," *China Communications*, vol. 14, no. 5, pp.1-16, May 2017.

[31] S. B. Cohn, "A class of broadband three-port TEM-mode hybrids," *IEEE Trans. Microw. Theory Techn*., vol. MTT-16, no. 2, pp. 110-116, Feb. 1968.

[32] J.-Q. Gong, K. Gao, and C.-H. Liang, "Synthesis of a miniaturised wireless local area network dual-band microstrip Wilkinson power divider through a general three-step optimisation process," *IET Microw., Antennas Propag*., vol. 9, no. 12, pp. 1274–1278, Sep. 2015.

[33] L. Young, "Tables for cascaded homogeneous quarter-wave transformers (correction)", *IRE Trans. Microw. Theory Tech.*, vol. MTT-8, no. 3, pp. 243-244, Mar. 1960.

[34] S. W. Lee, C. S. Kim, K. S. Choi, J. S. Park, D. Ahn, "A general design formula of multi-section power divider based on singly terminated filter design theory", *IEEE MTT-S Int. Microw. Symp. Dig.*, vol. 2, pp. 1297-1300, 2001.

[35] T, Yu, “A broadband Wilkinson power divider based on the Segmented Structure”, *IEEE Trans. Microw. Theory Techn.*, vol:66, Issue: 4, pp. 1902-1911, Feb. 2018.

[36] L. Young, "Stepped-impedance transformer and filter prototypes," *IRE Trans. Microwave Theory Tech*., vol. MTT-10, pp. 339-359, Sept. 1962.

[37] Hong, J.S.G. and Lancaster, M.J., 2004. Microstrip filters for RF/microwave applications (Vol. 167). John Wiley & Sons.

[38] S.-H. Chien & Y.-S. Lin. “Novel Wideband Absorptive Bandstop Filters With Good Selectivity” *IEEE Access*, 2017. Vol 5, pp. 18847-18861.

[39] M. M. Nizam, P. J. Soh and A.H.M Suhaizal “"Design of a Modified L-shaped Bandstop Filter for UWB applications." In Microwave and Optoelectronics Conference (IMOC), 2009 SBMO/IEEE MTT-S International, pp. 177-182. IEEE, 2009.

[40] F.-C. Chen, R.-S. Li, J.-M. Qiu, and Q.-X. Chu, ‘‘Sharp-rejection wideband bandstop filter using stepped impedance resonators,’’ *IEEE Trans. Compon., Packag., Manuf. Technol*., vol. 7, no. 3, pp. 444–449, Mar. 2017.

[41] S. W. Lee, C. S. Kim, K. S. Choi, J. S. Park, D. Ahn, "A general design formula of multi-section power divider based on singly terminated filter design theory", *IEEE MTT-S Int. Microw. Symp. Dig.*, vol. 2, pp. 1297-1300, 2001.

[42] A. M. Abbosh, "A compact UWB three-way power divider", *IEEE Microw. Wireless Compon. Lett.*, vol. 17, no. 8, pp. 598-600, Aug. 2007.

[43] H. Y. Yee, F.-C. Chang, and N. F. Audeh, “ N-way TEM-mode broadband power dividers,” *IEEE Trans. Microw. Theory Tech*., vol. MTT-18, no. 10, pp. 682–688, Oct. 1970.

[44] J. Zhou and K. Morris, “Effects of interconnecting transmission lines on four-way Wilkinson power divider,” Microw. Opt. Technol. Lett., vol. 51, no. 12, pp. 2850–2852, 2009.

[45] J. Zhou, K. A. Morris, and M. J. Lancaster, “General design of multi-way multi-section power dividers by interconnecting two-way dividers,” *IEEE Trans. Microw. Theory Tech*., vol. 55, no. 10, pp. 2208–2215, Oct. 2007.

[46] Y. Xu and R. G. Bosisio, “Design of multiway power divider by using stepped-impedance transformers,” *IEEE Trans. Microw. Theory Tech*., vol. 60, no. 9, pp. 2781–2790, Sep. 2012.

[47] L. Young, “Tables for cascaded homogeneous quarter-wave transformers,” *IRE Trans. Microw. Theory Tech*., vol. MTT-7, no. 3, pp. 233–237, Apr. 1959.

[48] L. Young, “Tables for cascaded homogeneous quarter-wave transformers (correction),” *IRE Trans. Microw. Theory Tech.*, vol. MTT-8, no. 3, pp. 243–244, Mar. 1960.

[49] G. L. Matthaei, L. Young, and E. M. T. Jones, *Microwave Filters, Impedance Matching Networks and Coupling Structures*. New York: McGraw-Hill, 1980.

[50] W.-J. Feng, M.-L. Hong, W.-Q. Che, Q. Xue. "Dual-Band Microstrip Bandstop Filter With Multiple Transmission Poles Using Coupled Lines" *IEEE Microwave and Wireless Components Letters*. Pp. 236-238, Vol: 27, Issue: 3, March 2017.

[51] W. Wang, M. Liao, Y. Wu, Y. Liu." Small-size high-selectivity bandstop filter with coupled-line stubs for dual-band applications." *Electronics Letters* [serial on the Internet]. (2014, Feb 13), 50(4): 286-288

[52] J. Hong, "Microstrip filters for RF/microwave applications." [electronic book]. Hoboken, N.J.: Wiley, 2011.

[53] J. Hong & J. M. Lancaster, "Couplings of microstrip square open-loop resonators for cross-coupled planar microwave filters." *Microwave Theory and Techniques, IEEE Transactions on*, 44(11), (1996): 2099-2109

[54] Y. Luo,& Q. Chu. "A Compact High Selectivity Dual-Band Bandstop Filter Using Bent L-Resonators." Microwave Conference (EuMC), 2013 European.

[55] H. Lee, C. Kim, W. Lim. "Compact wideband bandstop filters with electrically coupled open stubs." *Microwave And Optical Technology Letters* [serial on the Internet]. (2013, Nov 1), 55(11): 2701-2703.

[56] K. Song, Y. Zhu, Q. Duan, M. Fan, and Y. Fan, "Extremely compact ultra-wideband power divider using hybrid slotline/microstrip-line transition,'' *Electronics Letters*, vol. 51, no. 24, pp. 2014-2015, 2015.

[57] K. Song, Y. Mo, Q. Xue, and Y. Fan, "Wideband four-way out-of-phase slotline power dividers,'' *IEEE Transactions on Industrial Electronics*, vol. 61, no. 7, pp. 3598-3606, Jul. 2014.

[58] U. T. Ahmed and A. M. Abbosh, "Wideband out-of-phase power divider using tightly coupled lines and microstrip to slotline transitions,'' *Electronics Letters*, vol. 52, no. 2, pp. 126-128, 2016.

[59] K. Song, Y. Zhu, Q. Duan, M. Fan, and Y. Fan, "Extremely compact ultra-wideband power divider using hybrid slotline/microstrip-line transition,'' *Electronics Letters*, vol. 51, no. 24, pp. 2014-2015, 2015.

[60] S. Avrillon, I. Pele, A. Chousseaud, and S. Toutain, "Dual-band power divider based on semiloop stepped-impedance resonators," *IEEE Trans. Microw. Theory Tech*., vol. 51, no. 4, pp. 1269–1273, Apr.2003.

[61] C.Wang and V. F. Fusco, "Passive broadband millimeter-wave uniplanar MMIC balun," *IEEE Electronics Lett*., vol. 44, no. 21, October 2008.

[62] L. Wu, Z. Sun, H. Yilmaz and M. Berroth, "A dual-frequency Wilkinson power divider," *IEEE Trans. Microwave Theory Tech.*, vol.56, no. 1, pp. 278-284, January 2000.

[63] L. Chiu and Q. Xue, "A parallel strip ring power divider with high isolation and arbitrary power-dividing ratio," *IEEE Trans. Microwave Theory Tech*., vol.55, no. 11, pp. 2419-2462, November 2000.

[64] W. Feng, X. Ma, W. Che and Y. Wu. "Narrow-band balanced filtering network using coupled lines loaded with stubs," *Electronics Letters*. Vol: 54, issue: 6, pp. 366-368. March, 2018.

[65] Y. Wu and Y. Liu, "A novel wideband coupled-line Gysel power divider with function of impedance matching,'' *Journal of Electromagnetic Waves and Applications*, vol. 26, no. 14- 15, pp. 2012-2021, Oct. 2012.

[66] R. B. Ekinge, "A new method of synthesizing matched broadband TEM mode three-ports," *IEEE Trans. Microw. Theory Tech*., vol. MTT-19, no. 1, pp. 81–88, Jan. 1971.

[67] X. Tang and K. Mouthaan, "Analysis and design of compact two-way Wilkinson power dividers using coupled lines," in Asia–Pacific Microw. Conf., Dec. 7–10, 2009, pp. 1319–1322.

[68] Wong, S.W., and Zhu, L.: 'Ultra-wideband power divider with good in-band splitting and isolation performances', *IEEE Microw. Wirel. Compon. Lett.,* 2008, 18, (8), pp. 518–520.

[69] C.-W. Tang and J.-T. Chen, ''A design of 3-dB wideband microstrip power divider with an ultra-wide isolated frequency band,'' *IEEE Trans. Microw. Theory Techn.,* vol. 64, no. 6, pp. 1806–1811, Jun. 2016.

[70] L. Guo, H. Zhu, and A. M. Abbosh, "Wideband tunable in-phase power divider using three-line coupled structure," *IEEE Microw. Wireless Compon. Lett*., vol. 26, no. 6, pp. 404–406, Jun. 2016.

[71] T. Zhang and W. Che, "Compact tunable power divider with wide tuning frequency range and good reconfigurable responses,'' *IEEE Transactions on Circuits and Systems II: Express Briefs*, pp. 1-1, 2016.

[72] L. Gao, X. Y. Zhang, and Q. Xue, "Compact tunable filtering power divider with constant absolute bandwidth,*'' IEEE Transactions on Microwave Theory and Techniques*, vol. 63, no. 10, pp. 3505-3513, Oct. 2015.

[73] H. Zhu, A M. Abbosh, and L. Gao, "Planar In-Phase Filtering Power Divider With Tunable Power Division and Controllable Band for Wireless Communication Systems," *IEEE Transactions on Components, Packaging and Manufacturing Technology*, vol. 8, no. 8, pp. 1458-1468, Aug. 2018.

[74] C. Zhu, J. Xu and W. Kang, "Microstrip Multifunctional Reconfigurable Wideband Filtering Power Divider with Tunable Center Frequency, Bandwidth, and Power Division," *IEEE Transactions on Microwave Theory and Techniques*, VOL. 66, NO. 6, JUNE 2018

[75] Y. Wang, X. Y. Zhang, F. X. Liu and J. C. Lee, "A compact bandpass wilkinson power divider with ultra-wide band harmonic suppression," *IEEE Microw. Wireless Compon. Lett.*, vol. 27, no. 10, pp. 888-890, 2017.

[76] Gao, S.S., Sun, S., and Xiao, S.: 'A novel wideband bandpass power divider with harmonic-suppressed ring resonator', *Microw. Wirel. Compon. Lett*., 2013, 23, (3), pp. 119–121.

[77] Zhang, B., and Liu, Y.: 'Wideband filtering power divider with high selectivity', *Electron. Lett.,* 2015, 51, (23), pp. 1950–1952.

[78] C.-F. Chen, T.-Y. Huang, T.-M. Shen, and R.-B. Wu, "Design of miniaturized filtering power dividers for system-in-a-package," *IEEE Trans. Comp., Packag., Manufact. Technol.*, vol. 3, no. 10, pp. 1663–1672, Oct. 2013.

[79] K. Song, X. Ren, F. Chen, and Y. Fan, "Compact in-phase power divider integrated filtering response using spiral resonator," *IET Microw. Antennas Propag.,* vol. 8, no. 4, pp. 228–234, 2014.

[80] Chen, C.F., and Lin, C.Y.: 'Compact microstrip filtering power dividers with good in-band isolation performance', *IEEE Microw. Wirel. Compon. Lett*., 2014, 24, (1), pp. 17–19.

[81] D. Hammou, E. Moldovan, and S. O. Tatu, "Novel MHMIC millimeter wave power divider/combiner," in Proc. CCECE, Niagara Falls, ON, Canada, May 2011, pp. 280–283.

[82] D. Deslandes and K. Wu, "Integrated Microstrip and Rectangular Waveguide in Planar Form", *Microwave and Wireless Components Letters, IEEE*, vol. 11, no. 2, Feb. 2001, pp 68 -70.

[83] Zhang, Q.-L., Yin, W.-Y., He, S., and Wu, L.-S.: 'Compact substrate integrated waveguide (SIW) bandpass filter with complementary split-ring resonators (CSRRs)', *IEEE Microw. Wirel. Compon. Lett*., 2010, 20, (8), pp. 426–428, doi: 10.1109/ LMWC.2010.2049258

[84] F. Huang, J.Y. Zhou, W. Hong, 'Ku band continuously tunable circular cavity SIW filter with one parameter,' *IEEE Microw. Wirel. Compon. Lett.*, 26 (4) (2016), pp. 270-272.

[85] M. Li, C. Chen, and W. Chen, "Miniaturized dual-band filter using dual-capacitively loaded SIW cavities," *IEEE Microw. Wireless Compon. Lett.*, vol. 27, no. 4, pp. 344–346, Apr. 2017.

[86] X. Xu, J. P. Wang, and L. Zhu, "A new approach to design differentialmode bandpass filters on SIW structure," *IEEE Microw. Wireless Compon. Lett*., vol. 23, no. 12, pp. 635–637, Dec. 2013.

[87] H. Chen, W. Che, X. Wang and W. Feng, "Size-Reduced Planar and Nonplanar SIW Gysel Power Divider Based on Low Temperature Cofired Ceramic Technology," in *IEEE Microwave and Wireless Components Letters*, vol. 27, no. 12, pp. 1065-1067, Dec. 2017.

[88] J. Wang, J. Ni, Y.-X. Guo, and D. Fang, "Miniaturized microstrip Wilkinson power divider with harmonic suppression," *IEEE Microw. Wireless Compon. Lett.*, vol. 19, no. 7, pp. 440–442, Jul. 2009.

[89] H. Chen, W. Che, Y. Cao, W. Feng, and K. Sarabandi, "Functionreconfigurable between SPDT switch and power divider based on switchable HMSIW unit," *IEEE Microw. Wireless Compon. Lett.*, vol. 27, no. 3, pp. 275–277, Mar. 2017.

[90] X. Wang and X.-W. Zhu, ‘‘Quarter-mode circular cavity substrate integrated waveguide filtering power divider with via-holes perturbation,’’ *Electron. Lett*., vol. 53, no. 12, pp. 791–793, Aug. 2017.

[91] Danaeian, M., Moznebi, A.-R., Afrooz, K., and Hakimi, H.: ‘Miniaturized equal/unequal SIW power divider with bandpass response loaded by CSSRs’, *Electron. Lett.,* 2016, 52, (10), pp. 1864–1866.

[92] Z.-Z. Yu and K. Wu. “Broadband half-mode substrate integrated waveguide (HMSIW) Wilkinson power divider.” *2008 IEEE MTT-S International Microwave Symposium Digest (2008)*: 879-882.

[93] C. Li, , L. B. Lok, A. Khalid, V. Papageorgiou, J. Grant, and D. R. S. Cumming, “A coplanar ring power divider with high isolation for Vband and W-band applications,” Proceedings of the 42nd European Microwave Conference, 57–60, 2012.

[94] C. Li, L. B. Lok, A. Khalid, and D. R. S. Cumming, “Coplanar ring divider with wideband high isolation performance,” *Progress Electromagn. Res. Lett*., vol. 25, pp. 1–10, 2011.

[95] C. Li, A. Khalid, V. Papageorgiou, L. B. Lok, and D. R. S. Cumming, “A Wideband CPW Ring Power Combiner With Low Insertion Loss and High Port Isolation,” *IEEE Microw. Wirel. Compon. Lett*., vol. 22, no 11, pp. 580-582, November 2012.

Chapter 3 Design of a Broadband Wilkinson Power Divider with Wide Range Tunable Bandwidths

This chapter presents a novel two-way and a cascaded eight-way power divider with a wide range of tunable bandwidths. The proposed two-way power divider is designed based on adding a pair of capacitors in parallel with the transmission lines in a Trantanella-type of Wilkinson PD. This PD has an additional zero-reflection frequency which will significantly increase the bandwidth compared with a conventional Wilkinson PD. Moreover, the added zero- reflection frequency is sensitive to the capacitances so that the bandwidth can be tuned by tuning the capacitors. Analytic design methods and formulas are derived and presented in detail. A two-way PD is designed and measured to validate the proposed method. The measurement indicates that the device can achieve a 15 dB bandwidth of $\boldsymbol{f_H/f_L}$=2.73:1 (0.75 GHz to 2.05 GHz). The proposed method can be applied for the design of multi-way multi-section PDs. Meanwhile, an eight-way PD is designed and fabricated. The measured response has a 13 dB bandwidth of $\boldsymbol{f_H/f_L}$=2.67:1 (0.75 GHz to 2 GHz). The proposed PDs exhibit wide bandwidths, compact sizes, and good physical and electrical isolation features. The measurement agrees well with the theoretical prediction which validates the proposed design theory.

3.1 Introduction

The features of PDs regarding bandwidth, circuit size, insertion loss, and isolation will significantly influence the overall performance of the communication system. A Wilkinson-type PD [1] is one of the most widely used dividers due to its simple structure and low insertion loss. However, there are several drawbacks for the conventional Wilkinson PD. One is the narrow bandwidth, and the other weakness is the lack of physical isolation for the two outputs. In 2010, Trantanella [2] presented a novel PD by placing the isolation elements between the λ/4 transmission lines at an arbitrary phase angle instead of 90° as in a conventional Wilkinson divider to enhance both electrical isolation and physical separation. The structure has been investigated in depth in [3]. Although the layout of the Trantanella Wilkinson PD has been simplified, the bandwidth is limited to 1.5:1. Since there has been a sustained increase in the

demand of the wideband PDs, researches on broadband PDs have been proposed [4]-[6] to increase the effective bandwidth. However, most of them are designed based on quarter-wave transmission lines so that they suffer from the lack of compactness. Large sizes will make the integration very challenging in some wireless devices. Nowadays, frequency-tunable devices are attracting more and more attention because they can integrate diverse operating frequency bands in a single device [4] [5] to satisfy multi-standard systems. A reconfigurable PD based on the Trantanella structure was presented in [6] where the centre frequency can be changed from 0.85 GHz to 2.4 GHz by tuning the bias voltage on the varactor diodes. However, the effective bandwidth for each operational band is narrow. A few works [4]-[6] have been proposed to provide tunable centre frequency and tunable bandwidth features within one component, where the 10 dB bandwidth can achieve 2.32:1. These reconfigurable PDs have a high potential to be widely used in multi-standard systems. But unfortunately, the complexity of the circuit has been greatly increased, and also the10 dB in-band performance is normally not sufficient to many systems.

A new broadband PD with a wide range of tunable bandwidths is presented in this chapter. The idea is to add a pair of capacitors in parallel with the transmission lines as shown in **Fig. 3. 1**. The proposed structure introduces an additional zero-reflection frequency to broaden the operational bandwidth and make the bandwidth tunable. The idea of inserting a parallel capacitor has been reported in [7] to improve the out-of-band selectivity. The relationship between the variations of capacitance and the return loss has not yet been analytically discussed. This chapter provides mathematic proof and design guidance on controlling the added zero-reflection frequency for tunable bandwidths. The structure and design theory are discussed in Section 3.2. The relationships between the electrical length of transmission lines, zero-reflection frequency, and capacitance of added capacitors are illustrated and analysed in Section 3.3. In Section 3.4, a two-way and an eight-way three-section PD are designed, fabricated and measured to validate the proposed design method. Conclusions are drawn finally in Section 3.5.

3.2 Design of the PD

A conventional Wilkinson PD is perfectly matched at all ports at the centre frequency so that there is only one reflection-zero in the passband. To broaden the bandwidth, an additional reflection-zero at f_z can be generated by adding a pair of capacitors. As shown in **Fig. 3. 1**. C_P denotes the added capacitors. Z_0 stands for the port impedance which is 50 Ω here. θ_1, θ_2, and θ_3 represent the electrical lengths of the transmission lines at the initial centre frequency, which is assumed to be 1 GHz here. Z_1, Z_2, and Z_3 are the characteristic impedances of the transmission lines. Z_{ISO} represents the complex impedance isolation component. There will be two minimum-reflection frequencies for the proposed divider. One is near the original zero-reflection frequency $f_o = 1$ GHz and the other is the additional zero-reflection frequency f_z. By carefully choosing the values of the capacitors, the additional zero-reflection frequency f_z can significantly extend the operational bandwidth of the device. Details will be discussed in the following subsections.

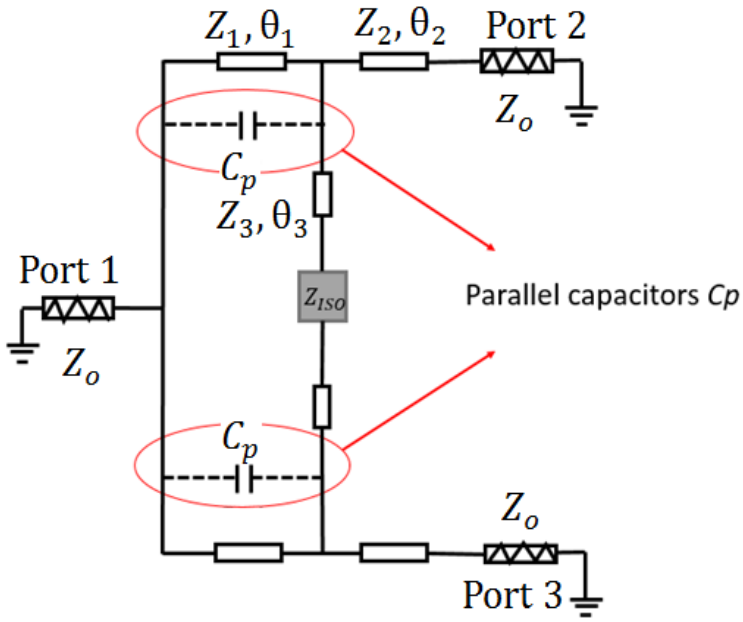

Fig. 3. 1 The proposed broadband bandwidth tunable PD.

3.2.1 Return Loss

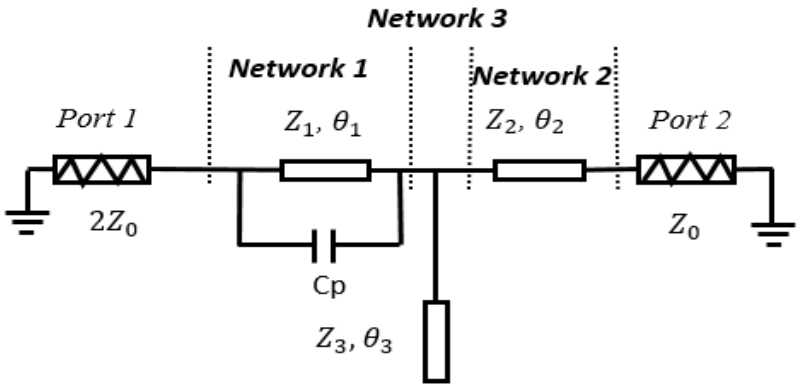

Fig. 3. 2 Even-mode equivalent circuit for the proposed divider.

The equivalent circuit of the proposed PD under even-mode excitation is shown in **Fig. 3. 2**. The circuit can be divided into three sub-networks. Network 1 in the even-mode circuit contains one front transmission and a capacitor that are connected to the front transmission line in parallel. Network 2 is a single transmission line, and Network 3 is an open stub in the isolation branch. To analyze the even-mode equivalent circuit, ABCD parameters for the first network need to be calculated. Firstly, the normalized Y matrix of capacitor C_p and the front transmission line can be derived:

$$\left|\overline{Y_{C_p}}\right| = \begin{vmatrix} j\bar{Y} & -j\bar{Y} \\ -j\bar{Y} & j\bar{Y} \end{vmatrix} \tag{3.1}$$

where $\bar{Y} = 2\pi\bar{f} \cdot \bar{C}_P$ is the normalized admittance of the capacitor C_P, and $\bar{f}$ is an arbitrary frequency. The normalized Y matrix for the front transmission line is

$$|\mathrm{Y}_{Tx1}| = \begin{vmatrix} -\dfrac{j}{\overline{Z_1}\cdot\tan(\theta_1\bar{f})} & \dfrac{j}{\overline{Z_1}\cdot\sin(\theta_1\bar{f})} \\ \dfrac{j}{\overline{Z_1}\cdot\sin(\theta_1\bar{f})} & -\dfrac{j}{\overline{Z_1}\cdot\tan(\theta_1\bar{f})} \end{vmatrix} \tag{3.2}$$

The ABCD matrix of the Network 1 can be derived by adding the Y matrixes in (1) and (2) and then convert the sum to the ABCD matrix.

$$\left|\overline{Y_{C_p}}\right| + |\overline{Y_{Tx1}}| = \begin{vmatrix} j\bar{Y} - \frac{j}{\overline{Z_1}\cdot\tan(\theta_1\bar{f})} & -j\bar{Y} + \frac{j}{\overline{Z_1}\cdot\sin(\theta_1\bar{f})} \\ -j\bar{Y} + \frac{j}{\overline{Z_1}\cdot\sin(\theta_1\bar{f})} & j\bar{Y} - \frac{j}{\overline{Z_1}\cdot\tan(\theta_1\bar{f})} \end{vmatrix} \tag{3.3}$$

$$\begin{vmatrix} \bar{A} & \bar{B} \\ \bar{C} & \bar{D} \end{vmatrix}_{\text{network1}} = \begin{vmatrix} \frac{j\bar{Y} - \frac{j}{\overline{Z_1}\cdot\tan(\theta_1\bar{f})}}{j\bar{Y} - \frac{j}{\overline{Z_1}\cdot\sin(\theta_1\bar{f})}} & \frac{1}{j\bar{Y} - \frac{j}{\overline{Z_1}\cdot\sin(\theta_1\bar{f})}} \\ \frac{\left(j\bar{Y} - \frac{j}{\overline{Z_1}\cdot\tan(\theta_1\bar{f})}\right)^2 - \left(j\bar{Y} - \frac{j}{\overline{Z_1}\cdot\sin(\theta_1\bar{f})}\right)^2}{j\bar{Y} + \frac{j}{\overline{Z_1}\cdot\sin(\theta_1\bar{f})}} & \frac{j\bar{Y} - \frac{j}{\overline{Z_1}\cdot\tan(\theta_1\bar{f})}}{j\bar{Y} - \frac{j}{\overline{Z_1}\cdot\sin(\theta_1\bar{f})}} \end{vmatrix} \tag{3.4}$$

Then the ABCD matrices for Network 2 and 3 can be expresses as:

$$\begin{vmatrix} \bar{A} & \bar{B} \\ \bar{C} & \bar{D} \end{vmatrix}_{\text{network2}} = \begin{vmatrix} \cos(\theta_2\bar{f}) & jZ_2\sin(\theta_2\bar{f}) \\ \frac{j\sin(\theta_2\bar{f})}{Z_2} & \cos(\theta_2\bar{f}) \end{vmatrix} \tag{3.5}$$

$$\begin{vmatrix} \bar{A} & \bar{B} \\ \bar{C} & \bar{D} \end{vmatrix}_{\text{network3}} = \begin{vmatrix} 1 & 0 \\ j\frac{\tan(\theta_3\bar{f})}{Z_3} & 1 \end{vmatrix} \tag{3.6}$$

According to the sequence of these three networks, the ABCD matrix of the circuit can be obtained by multiplying the ABCD matrices of the networks:

$$\begin{vmatrix} \bar{A} & \bar{B} \\ \bar{C} & \bar{D} \end{vmatrix} = \begin{vmatrix} \bar{A} & \bar{B} \\ \bar{C} & \bar{D} \end{vmatrix}_{\text{network1}} \cdot \begin{vmatrix} \bar{A} & \bar{B} \\ \bar{C} & \bar{D} \end{vmatrix}_{\text{network3}} \cdot \begin{vmatrix} \bar{A} & \bar{B} \\ \bar{C} & \bar{D} \end{vmatrix}_{\text{network2}} \tag{3.7}$$

Hence:

$$\begin{vmatrix} \overline{A} & \overline{B} \\ \overline{C} & \overline{D} \end{vmatrix} = \begin{vmatrix} \frac{\overline{Y} - \frac{1}{\sqrt{2}\tan(\theta_1\overline{f})}}{\overline{Y} - \frac{1}{\sqrt{2}\sin(\theta_1\overline{f})}} & \frac{1}{j(\overline{Y} - \frac{1}{\sqrt{2}\sin(\theta_1\overline{f})})} \\ \frac{(\overline{Y} - \frac{1}{\sqrt{2}\sin(\theta_1\overline{f})})^2 - (\overline{Y} - \frac{1}{\sqrt{2}\tan(\theta_1\overline{f})})^2}{j(\overline{Y} - \frac{1}{\sqrt{2}\sin(\theta_1\overline{f})})} & \frac{\overline{Y} - \frac{1}{\sqrt{2}\tan(\theta_1\overline{f})}}{\overline{Y} - \frac{1}{\sqrt{2}\sin(\theta_1\overline{f})}} \end{vmatrix} \bullet \begin{vmatrix} 1 & 0 \\ j\frac{\tan(\theta_3\overline{f})}{\sqrt{2}} & 1 \end{vmatrix} \bullet \begin{vmatrix} \cos(\theta_2\overline{f}) & j\sqrt{2}\sin(\theta_2\overline{f}) \\ j\frac{\sin(\theta_2\overline{f})}{\sqrt{2}} & \cos(\theta_2\overline{f}) \end{vmatrix} \tag{3.8}$$

where the characteristic impedance of the transmission lines are normalized to 50 Ω, and the frequency is normalized to the original centre frequency $f_o = 1\,\text{GHz}$. To simplify the calculation, the transmission lines have equal normalized characteristic impedances $\overline{Z_1} = \overline{Z_2} = \overline{Z_3} = \sqrt{2}$. $\theta_i \bar{f}$ (where i=1, 2, 3) represents the electrical length of each transmission line at normalized frequency $\bar{f}$. The normalized input impedance of Port 1 at f_z should satisfy:

$$\overline{Z_{in}^{ev}} = \frac{\overline{A} + \overline{B}}{\overline{C} + \overline{D}} = 2 + j0 \tag{3.9}$$

The real part of the input impedance should satisfy $\text{Re}\left(\overline{Z_{in}^{ev}}\right) = 2$. The capacitance C_P can be obtained by:

$$\overline{Y} = 2\pi \overline{f_z} \cdot \overline{C_P} = \frac{\tan(\theta_3 \overline{f_z})(\tan(\theta_1 \overline{f_z}) \tan(\theta_2 \overline{f_z}) + 1)}{\sqrt{2}(\tan(\theta_1 \overline{f_z}) \tan(\theta_3 \overline{f_z}) + \frac{2}{\cos(\theta_1 \overline{f_z})} - 2)} \tag{3.10}$$

where $\overline{f_z}$ is the normalized zero-reflection frequency. The imaginary part of the input impedance should satisfy $\text{Im}\left(\overline{Z_{in}^{ev}}\right) = 0$. The relationship between θ_i (i=1, 2, 3) and $\overline{f_z}$ can be expressed as:

$$\frac{\frac{\tan(\theta_3 \overline{f_z}) \tan(\theta_1 \overline{f_z}) + 1}{\tan(\theta_2 \overline{f_z})} - 2\tan(\theta_3 \overline{f_z}) - \tan(\theta_1 \overline{f_z})}{\frac{\tan(\theta_1 \overline{f_z})}{\tan(\theta_2 \overline{f_z})} - 2\tan(\theta_3 \overline{f_z}) \tan(\theta_1 \overline{f_z}) + 4 - \frac{4}{\cos(\theta_1 \overline{f_z})}} = \frac{\tan(\theta_2 \overline{f_z}) \tan(\theta_1 \overline{f_z}) + 1}{\frac{2}{\frac{\cos(\theta_1 \overline{f_z})}{\tan(\theta_3 \overline{f_z})} - 2} + \tan(\theta_1 \overline{f_z})} \tag{3.11}$$

To simplify the equation, the formulas can assume some restrictive conditions. For example, for Trantanella dividers, there is usually the condition of $\theta_2 = 90° - \theta_1$. For practical applications, the electrical length of the additional transmission lines θ_3 could be any value but is usually

chosen between 0° to 15° referring to [3]. In this chapter, θ_3 is 7°. For any chosen zero-reflection frequency $\bar{f}_z$ ($1 < \bar{f}_z < 3$), θ_1 can be obtained from (3.11), given that $\theta_2 = \pi/2 - \theta_1$ and θ_3 is a fixed value. Now the value of C_P can be calculated by (3.10).

3.2.2 Isolation Circuit

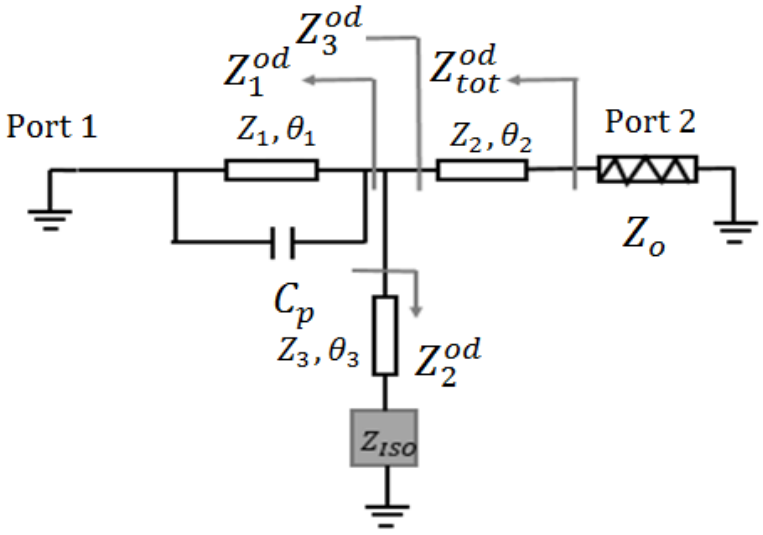

Fig. 3. 3 Odd-mode equivalent circuit for the proposed divider.

The performance of isolation can be obtained by using the odd-mode analysis method. The theoretical values of components in the isolation circuit Z_{ISO} can be found under the condition of perfect matching for port 2 and port 3 at the centre frequency $f_c = (f_0 + f_z)/2$. **Fig. 3. 3** shows the odd-mode equivalent circuit of the proposed PD. $\overline{Z_1^{od}}$, $\overline{Z_2^{od}}$, $\overline{Z_3^{od}}$, and $\overline{Z_{tot}^{od}}$ are the normalized output impedances of the circuit respectively, and they can be obtained by using:

$$\overline{Z_1^{od}} = \frac{j\sqrt{2}\tan(\theta_1 \overline{f_c}) \cdot \frac{1}{j\overline{Y}}}{j\sqrt{2}\tan(\theta_1 \overline{f_c}) + \frac{1}{j\overline{Y}}} \tag{3.12}$$

$$\overline{Z_2^{od}} = \sqrt{2}\frac{\frac{\overline{Z_{ISO}}}{2} + j\sqrt{2}\tan(\theta_3 \overline{f_c})}{\sqrt{2} + j\frac{\overline{Z_{ISO}}}{2}\tan(\theta_3 \overline{f_c})} \tag{3.13}$$

$$\overline{Z_3^{od}} = \frac{\overline{Z_1^{od}} \cdot \overline{Z_2^{od}}}{\overline{Z_1^{od}} + \overline{Z_2^{od}}} \tag{3.14}$$

$$\overline{Z_{tot}^{od}} = \sqrt{2}\,\frac{\overline{Z_3^{od}} + j\sqrt{2}\tan(\theta_2\,\overline{f_c})}{\sqrt{2} + j\overline{Z_3^{od}}\tan(\theta_2\,\overline{f_c})} \tag{3.15}$$

$$\overline{Z_{ISO}} = -\frac{2\sqrt{2}(\tan(\theta_1\overline{f_c}) + \tan(\theta_3\overline{f_c}) - \tan(\theta_1\overline{f_c})\tan(\theta_2\overline{f_c})\tan(\theta_3\overline{f_c}) - \sqrt{2}\overline{Y}\tan(\theta_1\overline{f_c})\tan(\theta_3\overline{f_c}))}{\sqrt{2}(\tan(\theta_1\overline{f_c})\tan(\theta_2\overline{f_c})\tan(\theta_3\overline{f_c}) + \sqrt{2}\overline{Y}\tan(\theta_1\overline{f_c})\tan(\theta_2\overline{f_c}) - \tan(\theta_1\overline{f_c}) - \tan(\theta_2\overline{f_c})) + j[\tan(\theta_1\overline{f_c})(\sqrt{2}\overline{Y} + \tan(\theta_2\overline{f_c}) + \tan(\theta_3\overline{f_c})) - 1]}$$
$$-\frac{2j(\sqrt{2}\overline{Y}\tan(\theta_1\overline{f_c})\tan(\theta_2\overline{f_c})\tan(\theta_3\overline{f_c}) - \tan(\theta_1\overline{f_c})\tan(\theta_2\overline{f_c}) - \tan(\theta_2\overline{f_c})\tan(\theta_3\overline{f_c}) - \tan(\theta_1\overline{f_c})\tan(\theta_3\overline{f_c}))}{\sqrt{2}(\tan(\theta_1\overline{f_c})\tan(\theta_2\overline{f_c})\tan(\theta_3\overline{f_c}) + \sqrt{2}\overline{Y}\tan(\theta_1\overline{f_c})\tan(\theta_2\overline{f_c}) - \tan(\theta_1\overline{f_c}) - \tan(\theta_2\overline{f_c})) + j[\tan(\theta_1\overline{f_c})(\sqrt{2}\overline{Y} + \tan(\theta_2\overline{f_c}) + \tan(\theta_3\overline{f_c})) - 1]} \tag{3.16}$$

The output impedance $\overline{Z_{tot}^{od}}$ equals to 1 at the centre frequency $\bar{f}_c$ for perfect matching at output ports. Thus, the total impedance of the isolation circuit can be derived by (3.16). The impedance $\overline{Z_{ISO}}$ can be calculated by substituting the design parameters of the transmission lines that described in the previous section. Since a series RLC circuit is used in this design, the real part and imaginary part of $\overline{Z_{ISO}}$ should satisfy:

$$\begin{cases} \mathrm{Re}\left(\overline{Z_{ISO}}\right) = \dfrac{\overline{R}}{2} \\ \mathrm{Im}\left(\overline{Z_{ISO}}\right) = 2\overline{\omega_C}\,\overline{L} - \dfrac{1}{2\overline{\omega_C}\,\overline{C}} \end{cases} \tag{3.17}$$

where $\overline{\omega_c}$ is the normalized centre angle frequency. The relationship between design parameters (such as the values for RLC) and perfect isolation performance among the circuit ports can be found through analysing the network isolation using the method that was presented in [4] [10] [11]. The summation admittances of both circuit branches are zero when the circuit is entirely isolated.

3.2.3 Design Parameters and Simulation

Theoretical equations in Section 3.2.1 and Section 3.2.2 are derived to determine design parameters. Firstly, the electrical length of the first and second transmission lines θ_1 and θ_2 should be determined based on the original centre frequency. The original centre frequency f_0 is designed to be 1 GHz and all the terminal loads are 50 Ω. Firstly, $\theta_3 = 7°$ and $Z_1 = Z_2 = Z_3 = 70.7\ \Omega$ are selected in the design. Then, to introduce an additional zero reflection frequency f_Z at 1.8 GHz for a 20 dB bandwidth, the electrical length of the transmission

lines $\theta_1 = 53°$, $\theta_2 = 37°$ (where $\theta_1 + \theta_2 = 90°$ is assumed in this design) can be determined using (3.11). Therefore, the capacitance C_P can be calculated by substituting $\theta_1 = 53°$, $\theta_3 = 7°$ and $f_Z = 1.8$ GHz into (3.10).

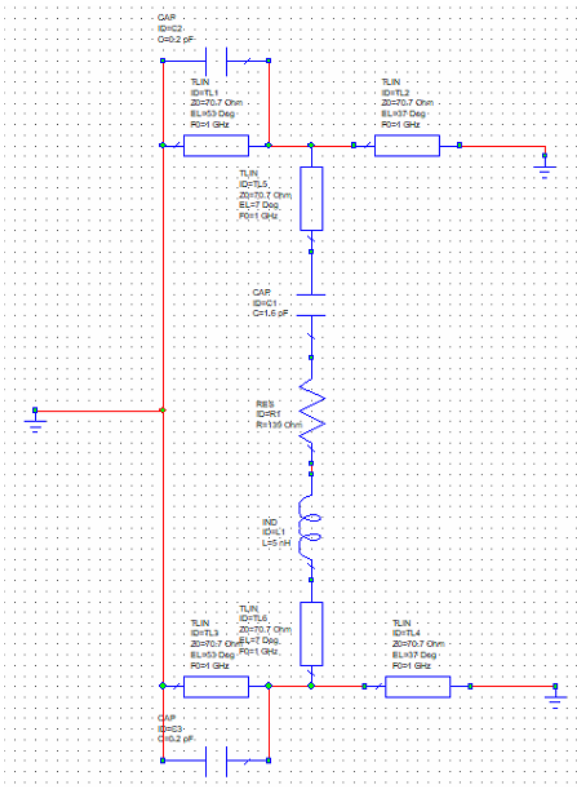

(a)

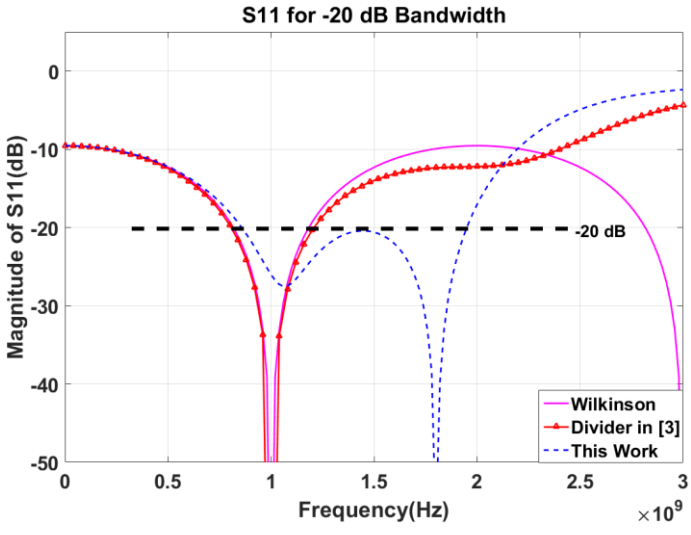

(b)

Fig. 3. 4 (a) AWR schematic circuit, (b) comparison of the simulated 20 dB bandwidth of S_{11} between the proposed divider and previous works [1], [3] using AWR.

To work out the values of lumped elements on isolation circuit, $\theta_1, \theta_2, \theta_3$, C_p and centre frequency f_c (where $f_c = {(f_o + f_z)}/{2}$) are substituted into (3.16) to obtain the total impedance Z_{ISO}. Then according to (3.17), the real part of Z_{ISO} is half of the resistance while the imaginary part of Z_{ISO} is the sum of the inductance and capacitance on the isolation circuit. As a result, R, L and C can be obtained respectively. **Fig. 3. 4**(a) shows the schematic circuit for the proposed PD. The component values of the schematic circuit can be obtained by using (3.10),(3.11), (3.16) and (3.17). The return loss S_{11} can be calculated and shown as the blue dash curve in **Fig. 3. 4**(b). The proposed design was simulated and optimized using AWR to achieve a wider 20 dB bandwidth than a Trantanella-type PD or a conventional Wilkinson PD. Then schematic circuit was realized using distributed elements of transmission lines. Sonnet was used in this design. The PD was designed on a Rogers RT/5880 substrate with ε_r=2.2. The thickness of the substrate is 0.79 mm, and the copper cladding is 35 μm thick. The layout is shown in **Fig. 3. 5.** The front transmission lines are bent to fit in the capacitors. The widths of all transmission lines are the same in this design. The lengths of the transmission lines were finely adjusted for optimized results. All the calculated and optimized design parameters are listed in **Table 3.1**.

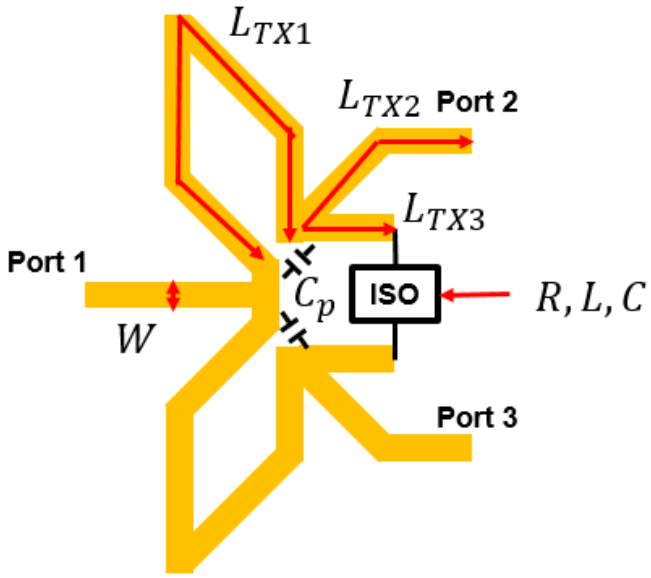

Fig. 3. 5 Fabrication layout of proposed two-way PD.

Table 3. 1 COMPARISON OF CALCULATED AND OPTIMIZED PARAMETERS.

Items	Cal.	Opt.	Items	Cal	Opt.
L_{TX1}	35.9 mm	38 mm	C_P	0.19 pF	0.2 pF
L_{TX2}	19.8 mm	22 mm	R	139Ω	130Ω
L_{TX3}	6.3 mm	8 mm	L	5 nH	3.9 nH
W	1.34 mm	1.35 mm	C	1.6 pF	1 pF

3.3 Parametric Studies Regarding Bandwidth

The bandwidth of the proposed PD can be affected by choosing different parameters such as θ_1 (under the condition of $\theta_1 + \theta_2 = 90°$) and capacitance C_p. Parametric studies regarding bandwidth are conducted in this section. Although the bandwidth cannot be tuned in a linear behaviour, the control of the bandwidth can be guided by sketching the bandwidth plot against the variation of θ_1 and C_p. Simulations are conducted using Matlab and AWR.

3.3.1 Bandwidth Regarding θ_1

The bandwidth changes result from the additional reflection-zero. If the reflection-zero is located far from the original reflection minimum (around 1 GHz) then the bandwidth could be broadened significantly. Theoretically, the S_{11} response varies depending on different θ_1 ($\theta_1 + \theta_2 = 90°$). **Fig. 3. 6** describes the additional reflection-zero f_z changes as a function of θ_1 and corresponding C_P with all the other parameters fixed. All sets of design parameters are calculated as described in **Section 3.2.3,** the curves in **Fig. 3. 6** are plotted using Matlab. The figure illustrated that a larger θ_1 can produce a reflection-zero at the higher frequency with a decrease of C_P. However, a trade-off should be made for bandwidth and overall in-band performance. The ripple between f_o andf_c is described as worst in-band S_{11}. As it shown is **Table 3.2**, the worst in-band S_{11} deviates with the increase of θ_1.

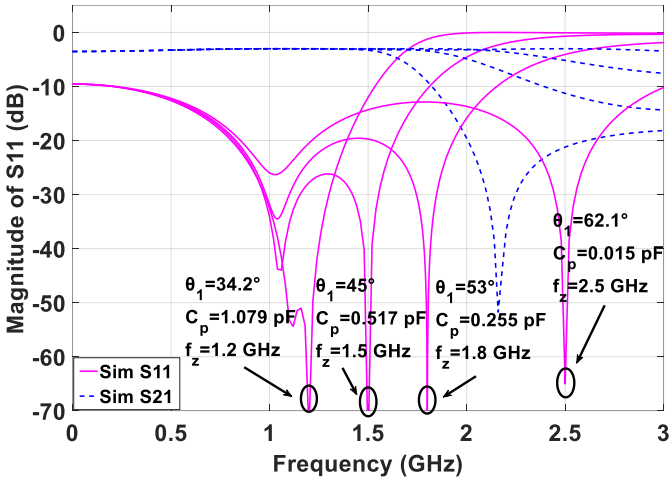

Fig. 3. 6 Circuit parameters for realising different additional zero-reflection frequencies.

Table 3. 2 CALCULATED DESIGN PARAMETERS FOR DIFFERENT ADDITIONAL ZERO REFLECTION FREQUENCIES.

Additional Zero Reflection Frequency f_Z (GHz)	**θ_1 (°)**	**Capacitance C_P (pF)**	**Worst S_{11} In-Band (dB)**
1.2	34.2°	1.079	-50.4
1.4	41.6°	0.661	-30.11
1.6	48.0°	0.408	-26.2
1.8	53.0°	0.256	-19.6
2.0	56.8°	0.158	-17.02
2.2	59.6°	0.088	-15.11
2.4	61.5°	0.037	-13.56
2.5	62.1°	0.015	-12.86

A contour map is shown in **Fig. 3. 7** to give a comprehensive understanding of θ_1 and the corresponding bandwidth. The two concentrated areas indicate two S_{11} reflection-zeros that locate at around 1 GHz and 1.8 GHz, respectively. Take -20 dB as the measure of bandwidth,

the achievable S_{11} bandwidth can be observed by drawing a horizontal line on the contours. For example, a horizontal line can be drawn at $\theta_1 = 55°$ in **Fig. 3. 7**. This line has two intersections with the 20-dB contour and a wide 20 dB bandwidth is achievable when θ_1 varies from 54° to 58°. A much wider 15-dB bandwidth can be achieved when θ_1 varies from 44° to 65° with a broad distance between intersections on the 15-dB contour. Those intersections are represented by $f_{H_{-20\,dB}}$, $f_{L_{-20\,dB}}$, $f_{H_{-15\,dB}}$, and $f_{L_{-15\,dB}}$ in **Fig. 3. 7**, respectively. Hence the 20 dB S_{11} bandwidth can be read from the horizontal difference between $f_{H_{-20\,dB}}$ and $f_{L_{-20\,dB}}$. While the difference between $f_{H_{-15\,dB}}$ and $f_{L_{-15\,dB}}$ represents the 15-dB bandwidth. For $\theta_1 = 55°$, the achievable 20 dB bandwidth is from 0.8 GHz to 1.9 GHz (bandwidth equals to2.37:1), while the achievable 15 dB bandwidth is from 0.65 GHz to 2.1 GHz (bandwidth equals to 3.2:1).

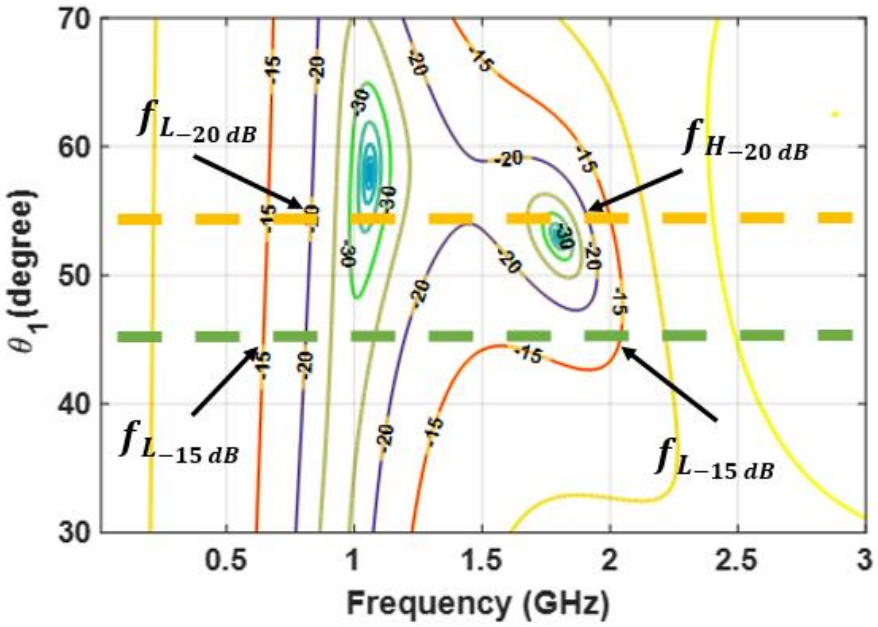

Fig. 3. 7 The contour of S_{11} with frequency as a function of θ_1 when $\theta_2 = \pi/2 - \theta_1$ C_P = 0.256 pF and $\theta_3 = 7°$.

In practice, it is challenging to vary the value of $\theta_1$once the PD is fabricated. Thus, choosing appropriate θ_1 at the first place is essential for the design. **Fig. 3. 8**(a)-(c) depict the bandwidth contours regarding a changing θ_1 with $C_p = 0.2$ pF, 0.4 pF and 0.8 pF, respectively. It can be seen from **Fig. 3. 8**(a) when $C_p = 0.2$ pF, although the two reflection minima are wide apart, the 20 dB bandwidth is divided into two parts. In this case, a wide -20 dB bandwidth is not

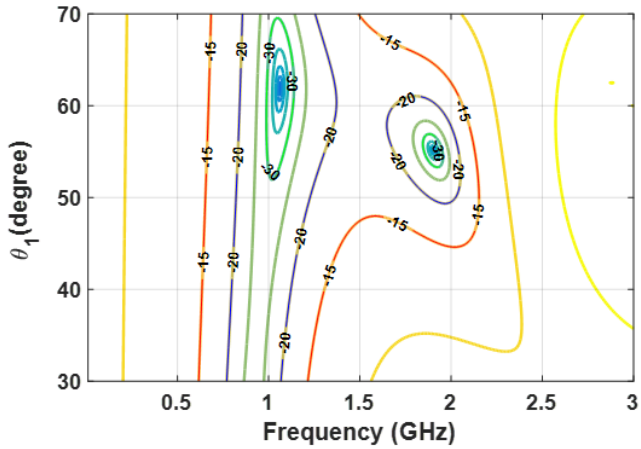

(a)

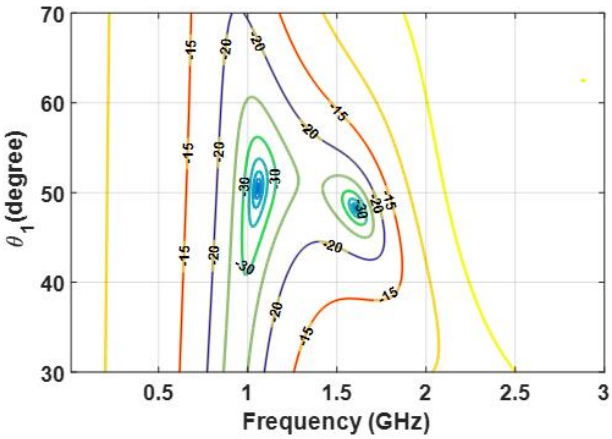

(b)

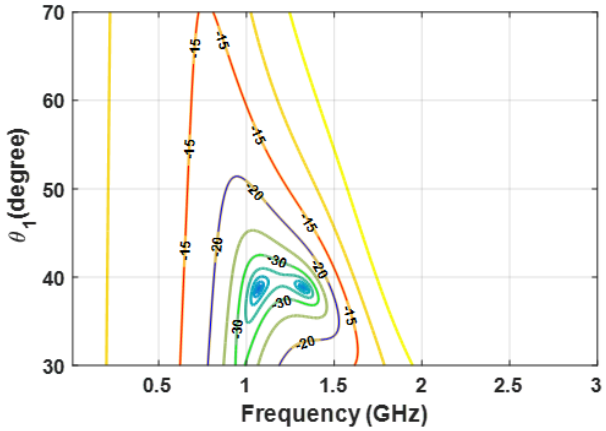

(c)

Fig. 3. 8 The contour of S_{11} with frequency as a function of θ_1 when $\theta_2 = \pi/2 - \theta_1$, $\theta_3 = 7°$ and (a) C_p=0.2 pF, (b) C_p=0.4 pF and (c) C_p=0.8 pF.

achievable no matter what value of θ_1 is chosen, but the 15 dB bandwidth could be comparably large. So compromise is needed. **Fig. 3. 8**(b) shows that the two dark areas are falling for a smaller θ_1 which means a smaller θ_1 is sufficient to produce two reflection minima, hence realising the widest bandwidth. **Fig. 3. 8**(c) illustrates that by further increasing C_p, a better in-band performance but a narrower bandwidth can be achieved with even smaller θ_1. To summarize **Fig. 3. 8**, generally speaking, a smaller C_p can provide a larger 20 dB bandwidth when θ_1 is around 45° to 50°. While using a higher C_p can obtain a narrower bandwidth but a better in-band performance with θ_1 around 35°.

3.3.2 Bandwidth Regarding Capacitance C_p

This section studies the effects of different C_p with a fixed θ_1, θ_2 and θ_3. For a conventional quarter-wavelength Wilkinson PD, the reflection zero locates at the centre frequency of 1 GHz. This reflection-zero becomes a reflection minimum in the proposed design due to the added capacitors. As mentioned above, the location of the additional reflection-zero determines the relationship between bandwidth and capacitance C_p. The larger the distance between the additional reflection zero and the reflection minimum (slightly larger than 1 GHz), the wider the bandwidth could be. However, that is not always the case because the in-band ripple will get higher with the increase of f_z. The bandwidth is limited by the 'worst' in-band S_{11} which is the peak value of the in-band ripple. As is discussed in the previous section, each θ_1 corresponds to a single value of C_P that can produce an additional reflection-zero f_z but the bandwidth can still be changed by tuning C_P.

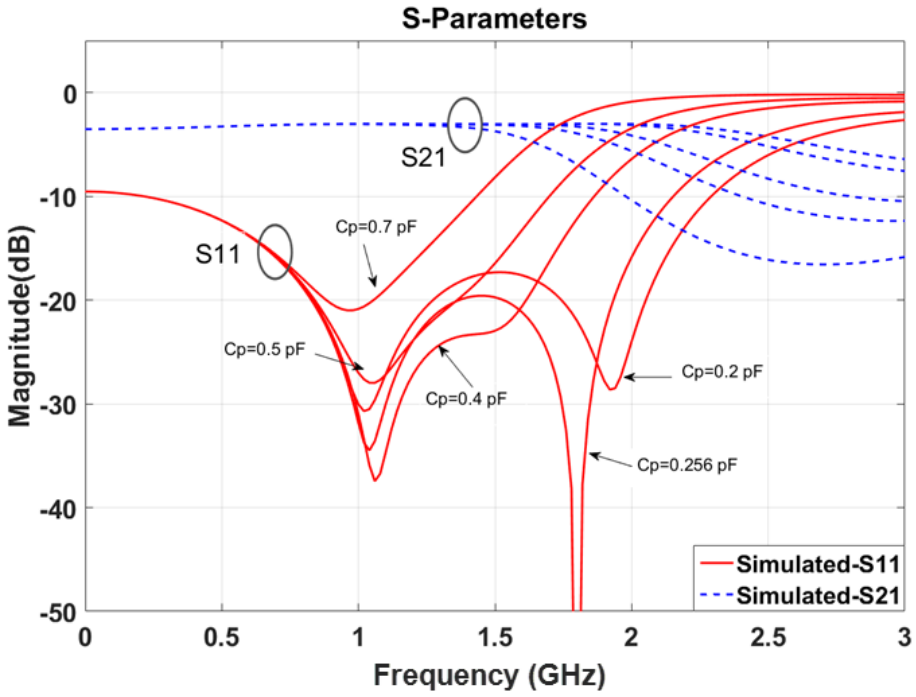

Fig. 3. 9 Changing C_P produces varying S_{11} and S_{21} with $\theta_1 = 53°, \theta_2$ 37° and $\theta_3 = 7°$.

Some design examples are shown in **Fig. 3. 9**. The original centre frequency is assumed to be 1 GHz, and the additional transmission minimum varies from 1.2 GHz to 2.5 GHz by changing $C_p$under the condition of $\theta_1 = 53°, \theta_2 = 37°$ and $\theta_3 = 7°$. The reflection coefficient at the original centre frequency 1GHz is no longer zero (-∞ in dB) by adding a pair of capacitors C_P, but the return loss is still very low (< -20 dB). The reflection minimum frequency moves slightly from the original centre frequency (1GHz), but it is still very close to 1 GHz ($1 < \bar{f} < 1.12$) according to (3.3), (3.4). It can be seen that an additional reflection-zero is generated by adding a $C_P = 0.256$ pF, and the in-band ripple is exactly on 20 dB. When C_P is increasing, the ripple will descend but the bandwidth will shrink. A wider bandwidth can be achieved by reducing C_P but the in-band performance will deteriorate simultaneously. In other word, for a given layout, increasing C_P will obtain a better in-band performance with either a narrower bandwidth or a wider bandwidth while a compromised in-band performance can be achieved by decreasing C_P.

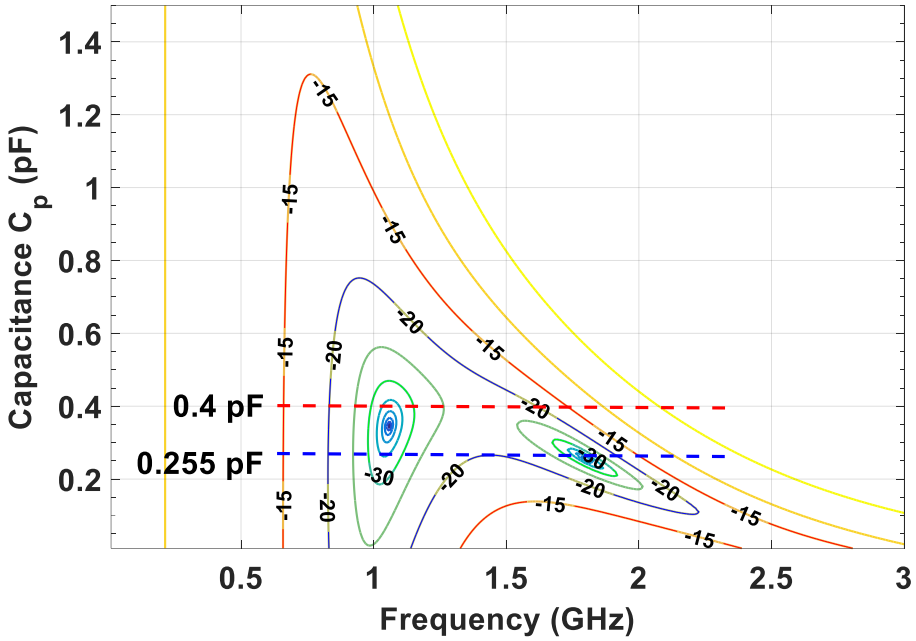

Fig. 3. 10 The contours of S_{11} as a function of frequencies and C_P when $\theta_1 = 53°$ and $\theta_3 = 7°$.

To emphasize the bandwidth and in-band performance changing in terms of different C_P, **Fig. 3. 10** shows the contours of S_{11} as a function of the capacitance C_P with $\theta_1 = 53°$ and $\theta_3 = 7°$. The two dark areas represent the two low-reflection frequency zones at around 1.1 GHz and 1.8 GHz in this case. The -30 dB, -20 dB, and -15 dB contours are shown in the figure. When $\theta_1 = 53°$ and $\theta_3 = 7°$, the calculated C_P equals to 0.255 pF, as shown in **Fig. 3. 10**, S_{11} is slightly worse than 20 dB at around 1.4 GHz. If C_P is chosen to be 0.4 pF, S_{11} is better than -20 dB from $f_{L-20\,dB} = 0.8$ GHz to $f_{H-20\,dB} = 1.6$ GHz. Slightly decreasing C_P, the distance between $f_{L-20\,\mathrm{dB}}$ and $f_{H-20\,\mathrm{dB}}$ can be further extended. On the contrary, the bandwidth will shrink when C_P increases. Therefore, the bandwidth of the proposed divider can be controlled in a wide range by alternating the capacitance C_P. It can be concluded that when the capacitance of C_P is small (but not smaller than 0.255 pF), the bandwidth is large while if C_P is increasing towards 0.8 pF, then the passband will attenuate. However, if -15 dB S_{11} is sufficient for the design, the tunable range of C_P will be large. Also, if C_P is smaller than 0.2 pF, then the performance will become a dual-band response. It can be concluded that for a fixed layout, C_P has a value range to maintain an effective bandwidth, and the bandwidth can vary from zero to maximum when

C_P is in this range. If a tunable bandwidth is preferred, a varactor can be employed to the circuit to have reconfigurable responses.

To sum up, if both C_P and θ_1 are considered in the design, the theoretical maximum 20 dB bandwidth has the trend as shown in **Fig. 3. 11**. The maximum bandwidth in this figure is 2.32:1 with $C_p = 0.25$pF and $\theta_1 = 55°$. In general, a small C_p and a large $\theta_1$can contribute to a wide bandwidth, but an overlarge θ_1 will result in a worse in-band performance which limits the extension of the bandwidth.

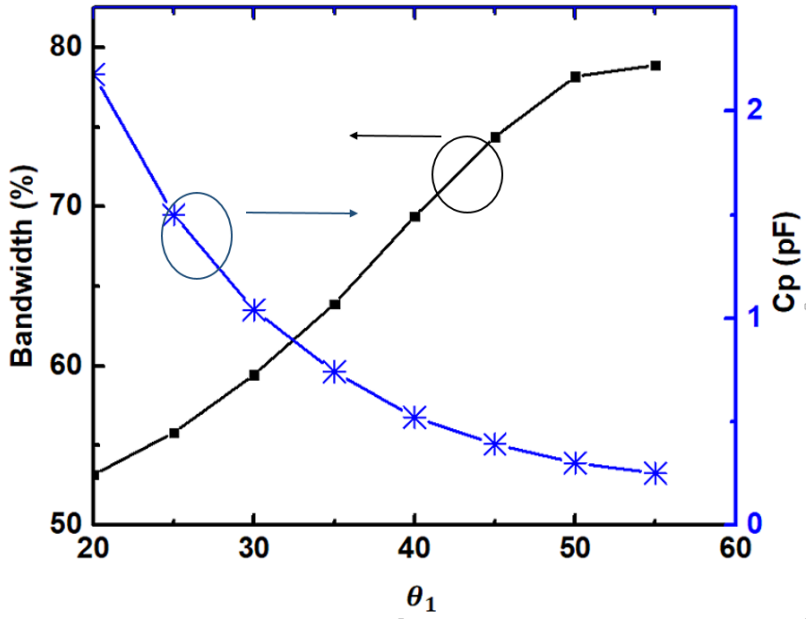

Fig. 3. 11 The maximum 20 dB bandwidth regarding θ_1 and corresponding C_p.

3.4 General Cases

In the previous sections of this chapter, impedances Z_1, Z_2 and Z_3 are assumed to be 70.7 Ω and $\theta_1 + \theta_2 = 90°$ is defined for the ease of calculation. However, it sacrifices the freedom of the design. Generally, for the proposed PD, the impedances and electrical lengths of Z_1, Z_2 and Z_3 could be different from each other instead of being 70.7Ω. Moreover, the sum of θ_1 and θ_2 is not necessarily to be 90°. The calculation process for the capacitance C_p is the same with (3.3), but the impedances Z_1, Z_2 and Z_3 are variables instead of being $\sqrt{2}Z_0$. Thus, the relationship between these parameters can be derived as:

$$\frac{\frac{\sin(\theta_2\bar{f})-\cos(\theta_1\bar{f})\mathrm{YZ}_1}{\tan(\theta_1\bar{f})^2}+\frac{\cos(\theta_2\bar{f})-2\sin(\theta_2\bar{f})\mathrm{YZ}_1}{\tan(\theta_1\bar{f})}+\frac{\cos(\theta_2\bar{f})\mathrm{YZ}_1-\sin(\theta_2\bar{f})}{\sin(\theta_1\bar{f})^2}}{\mathrm{A}+\mathrm{B}} =$$

$$\frac{\frac{\cos(\theta_2\bar{f})\,\mathrm{Z}_1-\sin(\theta_2\bar{f})\,\mathrm{YZ}_1^2-2\sin(\theta_2\bar{f})\,\mathrm{Z}_2}{\tan(\theta_1\bar{f})^2}+\frac{2\sin(\theta_2\bar{f})\mathrm{YZ}_1\mathrm{Z}_2-2\cos(\theta_2\bar{f})\mathrm{Z}_2-\sin(\theta_2\bar{f})\mathrm{Z}_1}{\tan(\theta_1\bar{f})}+\frac{2\sin(\theta_2\bar{f})\mathrm{Z}_2+\sin(\theta_2\bar{f})\mathrm{YZ}_1^2-\cos(\theta_2\bar{f})\mathrm{Z}_1}{\sin(\theta_1\bar{f})^2}}{(\mathrm{B}-\mathrm{A}-\cos(\theta_2\bar{f}))\,\mathrm{Z}_2-\sin(\theta_2\bar{f})\,\mathrm{Z}_1}$$

(3.18)

$$Y=\frac{\frac{\sin(\theta_2\bar{f})-\cos(\theta_1\bar{f})\mathrm{YZ}_1}{\tan(\theta_1\bar{f})^2}+\frac{\cos(\theta_2\bar{f})-2\sin(\theta_2\bar{f})\mathrm{YZ}_1}{\tan(\theta_1\bar{f})}+\frac{\cos(\theta_2\bar{f})\mathrm{YZ}_1-\sin(\theta_2\bar{f})}{\sin(\theta_1\bar{f})^2}}{\mathrm{Z}_1(\mathrm{A}+\mathrm{B})} \quad (3.19)$$

$$\mathrm{A}=\cos(\theta_2\bar{f})-2\sin(\theta_2\bar{f})\mathrm{YZ}_1$$

$$\mathrm{B}=\frac{4\sin(\theta_2\bar{f})(1-\cos(\theta_2\bar{f}))}{\sin(\theta_1\bar{f})}$$

$$\alpha=\frac{\tan(\theta_3\bar{f})}{\mathrm{Z}_3}$$

To find suitable C_p, all the parameters have to satisfy (3.11) at a selected reflection-zero frequency f_z. Then, Y can be calculated using (3.12), hence C_p=Y/$(2\pi\bar{f_z})$ can be found. It should be noted that although the length of the transmission line Z_3 is much shorter compared to Z_1 and Z_2, the changes of α can also affect the input impedance of the circuitry. So the changes of α cannot be ignored. Since $\tan(\theta_3\bar{f})$ and Z_3 have a ratio of α, if θ_3 changes, then the value of Z_3 needs be changed to maintain the same α. By doing so, the divider can achieve an identical performance. The calculation for the parameters in general cases is much complicated than the calculation in the previous section. It is preferred to substitute predefined parameters into the equations for simplification.

3.5 Experimental Results

3.5.1 Fabrication and Measurement

A two-way PD is fabricated and measured as shown in **Fig. 3. 12**. LPKF ProtoMat S62 is used for circuit fabrication. The circuit layout was exported from Sonnet and imported to the easy-

to-use LPKF CircuitCAM software for working process. The layout is printed on top of a Rogers RT/5880 0.031" substrate while the bottom is covered by copper as the ground of the circuit. The fabricated circuit has a compact size of 29 mm × 32 mm while the two output ports can be placed widely apart. A pair of surface amount capacitors and R, L, C on the isolation circuit are soldered on to the circuit. Three SMA connectors are soldered to the ports for measurement.

The circuit is measured by using a VNA (vector network analyser) Agilent FieldFox N9917A. The frequency sweeping range of the VNA is from 30 KHz to 18 GHz which is suitable for the proposed design. Firstly, the NA (network analyzer) mode is chosen to operate the equipment. Then S-parameter measurement was carried out. Before recording data, the measurement system (the VNA with two SMA cables) is calibrated by using a SOLT (Short-Open-Load-Thru) calibration kit. S_{11}, S_{21} and S_{22} can be measured by connecting cables to Port 1 and Port 2. S_{31} and S_{33} are measured by connecting cables to Port 1 and Port 3. The isolation S_{23} is measured between Port 2 and Port 3. A 50 Ω male load is always connected to the spare port that is not measured. The measurement was repeated several times, and the precision is around ± 0.1 dB. The measured magnitude of S-parameters versus sweeping frequencies are saved in corresponding files which can be imported to Matlab or Origins to plot measured results.

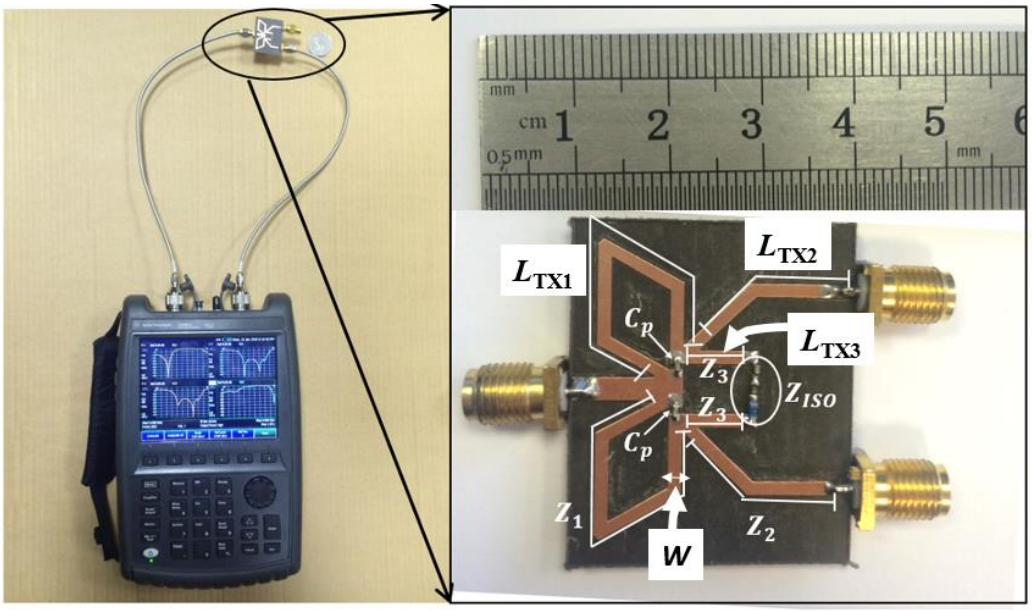

Fig. 3. 12 Photographs of the measurement set up and the fabricated two-way divider.

3.5.2 Two-way PD

The measured results of the proposed PD with C_P=0.2 pF are shown in **Fig. 3. 13**. It can be seen that a reflection-zero is generated as expected, and the operational bandwidth of the divider is significantly increased. As analyzed in **Section 3.3.2**, f_Z can be controlled by C_P. Two sets of S_{11} curves that correspond to $C_P = 0.4$ pF and $C_P = 0.8$ pF are also shown in **Fig. 3. 13**(a). When $C_P = 0.8$ pF, there is only one reflection minimum that locates at around 1 GHz which results in a narrow bandwidth. Decrease the capacitance of C_P to 0.4 pF, an additional reflection minimum appears in the upper passband at around 1.6 GHz, and the measured 20 dB bandwidth is 2.1:1. Then continually reducing the capacitance of C_P to 0.2 pF, the additional zero-reflection frequency moves to around 1.9 GHz. The 20 dB bandwidth cannot be realised because the in-band ripple is worse than 20 dB. The measurement shows a 15 dB bandwidth of 3.5:1 with C_P equal to 0.2 pF. This is much greater than that of traditional Wilkinson PDs or typical Trantanella ones. The measured reflection and isolation performances are also very good (<-15 dB) in the desired operational band. The measured insertion loss S_{21} is flat at around 3 dB over the whole operational band as **Fig. 3. 13**(b) shows. The measured results are in very good agreement with the simulations shown in **Fig. 3. 14**(a) (b). **Table 3.3** compares the measured performances of the two-way with other similar works. For two-way dividers, the effective bandwidth of the proposed one is much wider than all other works.

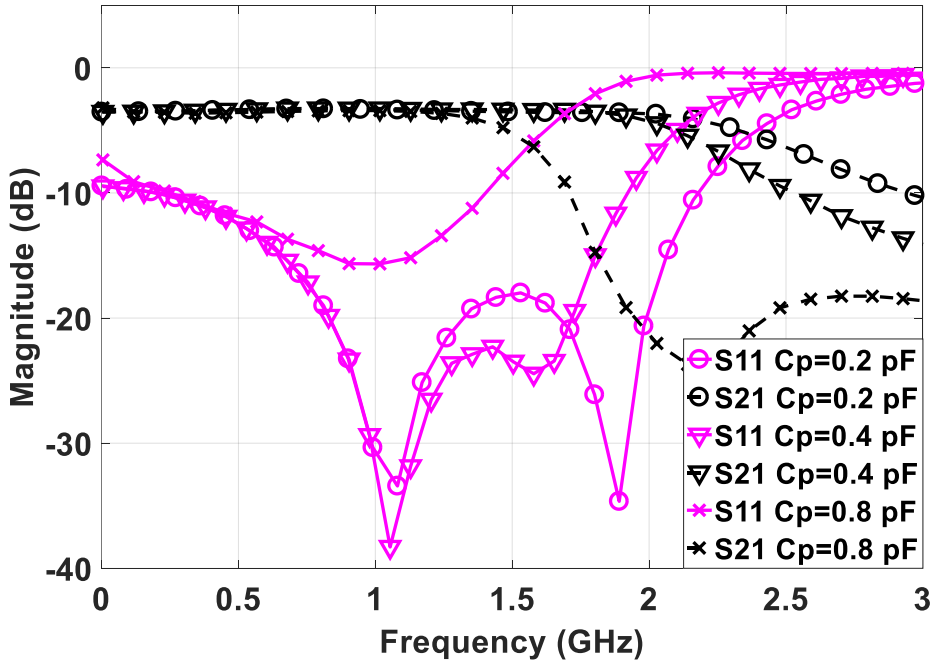

(a)

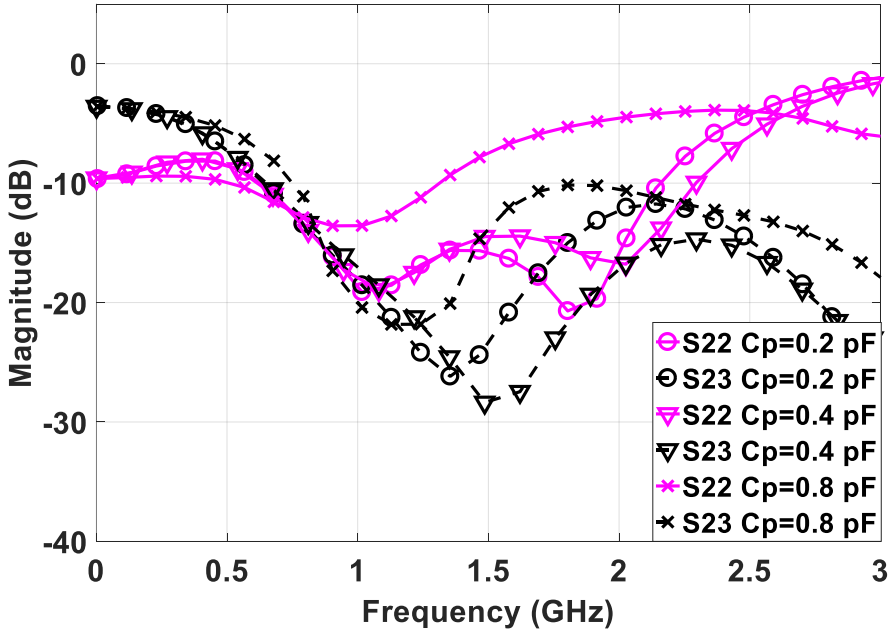

(b)

Fig. 3. 13 Measured results of (a) S_{11} & S_{21}, (b) S_{22} & S_{23} for proposed two-way PD.

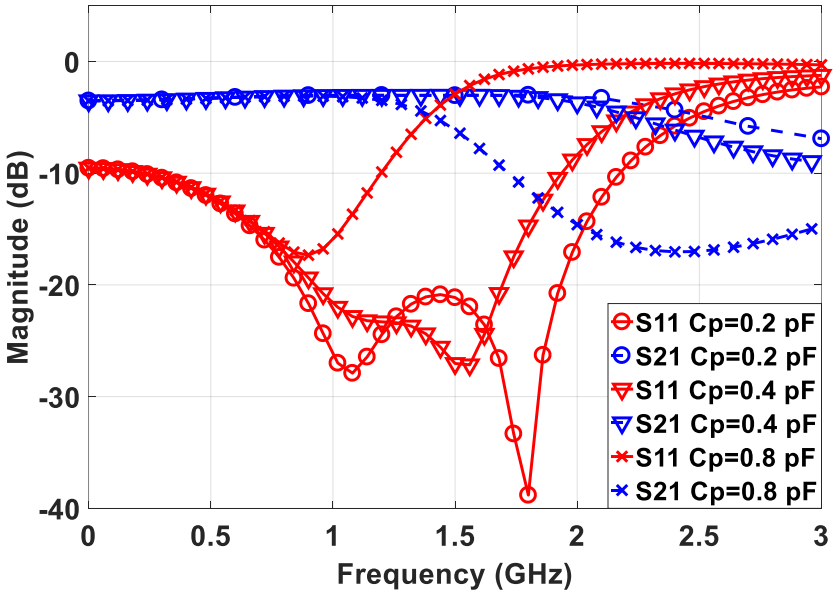

(a)

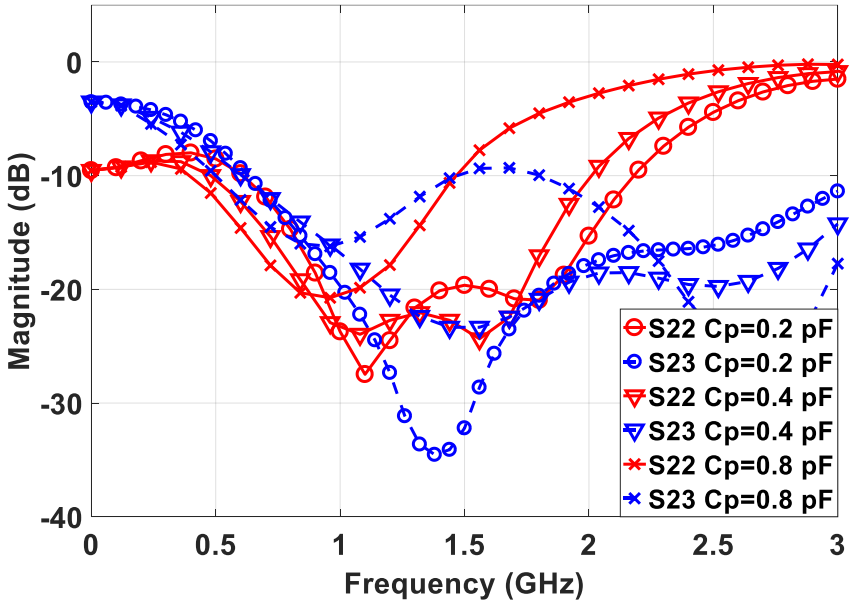

(b)

Fig. 3. 14 Simulated results of (a) S_{11} & S_{21}, (b) S_{22} & S_{23} for proposed two-way PD.

Table 3. 3 PERFORMANCE COMPARISON OF TWO-WAY WILKINSON-TYPE POWER DIVIDERS WITH OTHER WORKS.

Reference	Circuit Size	Physical Isolation	Bandwidth (15 dB)
[1]	$0.25\lambda_g$[1] *$0.02\lambda_g$	NO	2:1
[2]	$0.2\lambda_g$ *$0.05\lambda_g$	YES	NA
[3]	$0.25\lambda_g$*$0.06\lambda_g$	YES	1.45:1
[5]	$0.34\lambda_g$ *$0.2\lambda_g$	YES	1.85:1
This work	$0.12\lambda_g$ *$0.1\lambda_g$	YES	2.73:1

[1]: λ_g is the guided wavelength at the centre frequency of the bandwidth.

3.5.3 Eight-way PD

This method can also be applied to design multi-way PDs. The challenges are the complexity of design parameter calculations, and how to avoid deterioration of in-band performance by cascading more stages with such a wide bandwidth. An eight-way PD is designed and fabricated on the same substrate for further demonstration as shown in **Fig. 3. 15**.

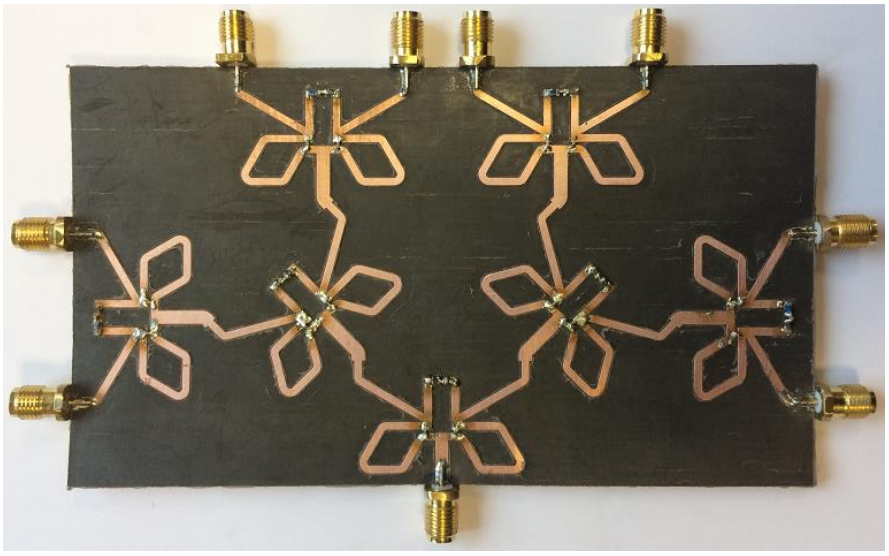

Fig. 3. 15 The fabricated circuit of eight-way PD.

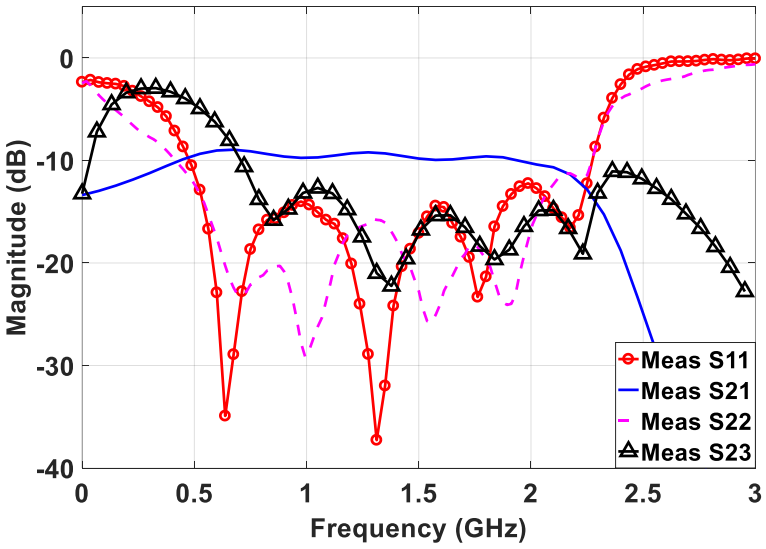

(a)

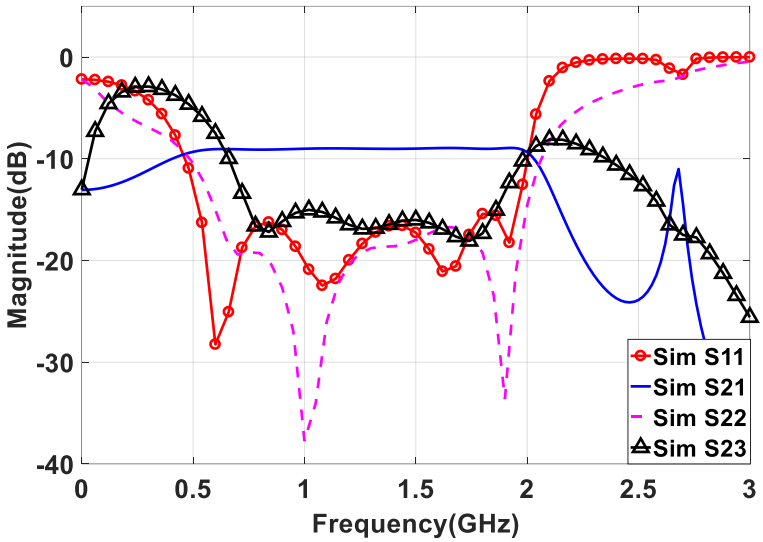

(b)

Fig. 3. 16 (a) Measured response and (b) simulated results of S_{11}, S_{21}, S_{22} and S_{23} for the eight-way PD.

The eight-way PD has three stages so that analytical solutions for design parameters are more difficult to work out. To simplify the calculation, the design parameters in every single section of the eight-way divider are almost identical (except for the lumped elements) to the two-way divider, which means no further changes on transmission lines are needed for multi-way PDs.

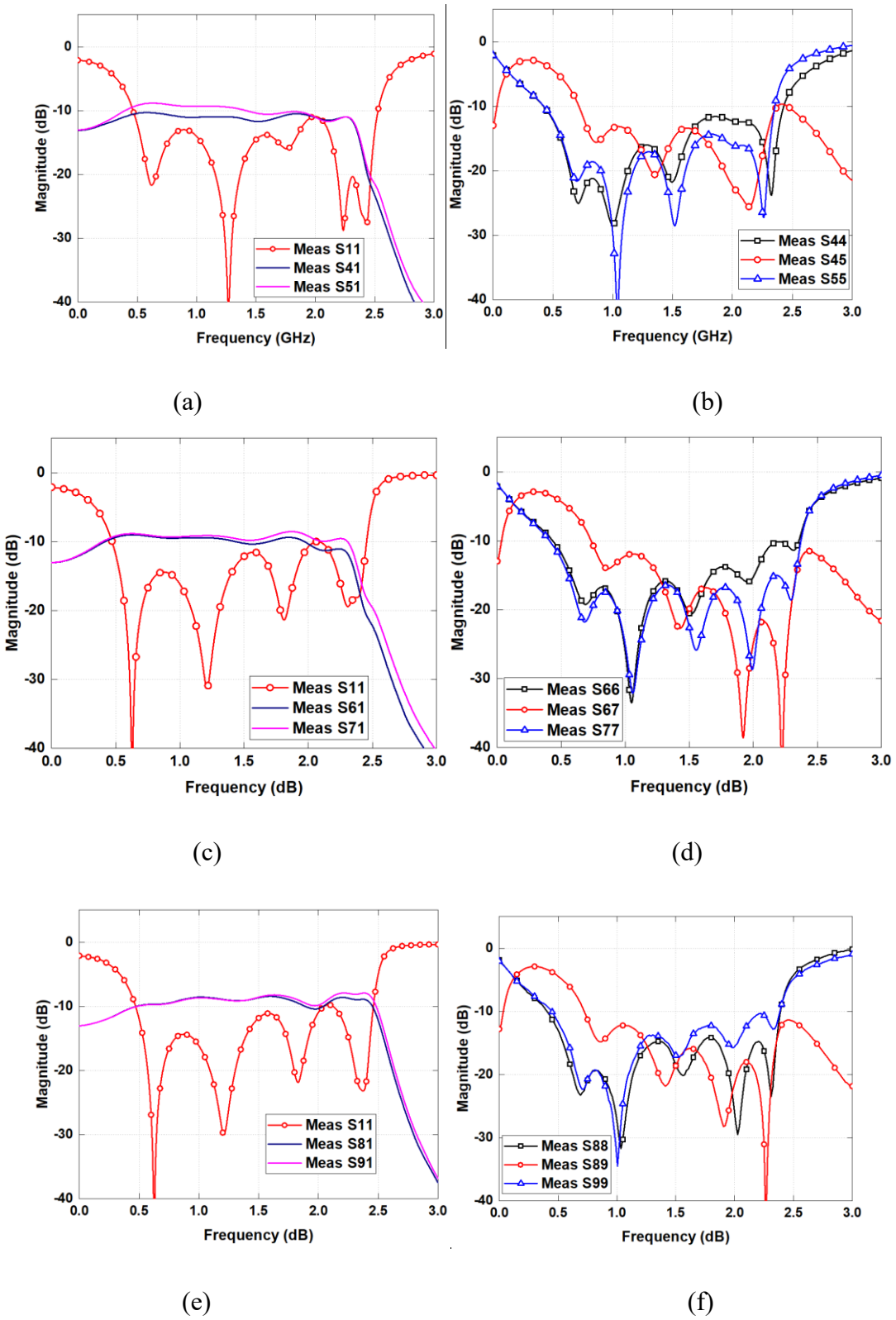

Fig. 3. 17 (a) S_{11}, S_{41}/S_{51}, and (b) S_{44}, S_{45} and S_{55} for ports 4&5, (c) S_{11}, S_{61}/S_{71}, and (d) S_{66}, S_{67} and S_{77} for ports 6&7, (e) S_{11}, S_{81}/S_{91}, and (f) S_{88}, S_{89} and S_{99} for ports 8&9.

The values of C_P and the lumped elements for the isolation circuits in different stages are optimized by simulation. The measured and simulated results for the eight-way PD between Port 1 to Port 2 & 3 can be seen in **Fig. 3. 16**(a) and (b), respectively. The simulated S_{11} is below 17 dB from 0.5 GHz to 2 GHz while the return losses, S_{22}/S_{33} are all below 18 dB over 0.6 GHz to 2 GHz. The isolation S_{23} is better than 16 dB over 0.75 GHz to 1.9 GHz. The measured return loss S_{11} and the output reflection S_{22} are better than 15 dB while the measured isolation S_{23} remains better than 13 dB. Compared with the simulation, the frequency shift and deviation of *S*-parameters are mainly caused by the fabrication error and the inaccuracy of the lumped elements. The rest ports (ports 4&5, ports 6&7 and ports 8&9) are also tested, and the measured results are plotted in **Fig. 3. 17**(a)-(c)**.** Ideally the results should be identical, however, due to the fabrication error and cable rotations, the measured results are slightly different. Overall, the bandwidth of the eight-way PD is wider than previouse similar works [12]-[15]. The measured results show very good agreement with the simulated ones.

3.6 Summary

Compact and wideband PDs are more and more desirable in modern microwave communication systems. The Trantanella-type PDs with the isolation circuit moved from the output ports to the middle of the transmission line can provide a compact size and additional physical isolation. A new design method has been proposed in this chapter that a pair of capacitors are added in parallel with the front-section transmission lines to broaden the operational bandwidth. The added capacitors have significantly increased the bandwidth of the PD. The design guidance regarding choosing the lengths and characteristic impedances of transmission lines, and the capacitance C_p are discussed in detail. The bandwidth can be enlarged by properly choosing design parameters, but the increment is limited by the deteriorated in-band performance. Experiments have been conducted to verify the design. For the proposed two-way PD, the measured 15-dB-return-loss bandwidth of the two-way divider is 3:1 while the effective bandwidth regarding all the *S*-parameters (S_{11}, S_{21}, S_{22}, S_{33} and S_{23}) is 2.73:1. For the eight-way PD, the measured 13-dB bandwidth is 2.67:1 considering return losses and isolation while the return loss bandwidth can achieve 4.5:1. The simulated and measured results confirm that this proposed method can provide a broadband response compared to other works. Also, changing the added capacitors will result in a broad tunable

bandwidth (from 0 to 2.73: 1) of the dividers. Apart from the extensive and tunable bandwidth, the proposed divider also has a compact size and can provide physical separation as well as electrical isolation among output ports. Moreover, the measurement on the eight-way PD has proved that this proposed method can be easily extended to multi-way divider designs.

References

[1] E. Wilkinson, "An N-way hybrid power divider," *IEEE Trans. Microw. Theory Thech*., pp. 116-118, 19060.

[2] C-.J-.Trantanella, "A novel power divider with enhanced physical and electrical port isolation," *IEEE MTT-S Int*., pp. 129-132, 2010.

[3] X. Wang, I. Sakagami, A. Mase, and M. Ichimura, "Trantanella Wilkinson power divider with additional transmission lines for simple layout.," *IET Microwaves, Antennas & Propagation,* vol. 8, no. 9, pp. 666-672, 2014.

[4] S.-W. Lee, C.-S. Kim, K. S. Choi, J.-S. Park, and D. Ahn, "A general design formula of multi-section power divider based on singly terminated filter design theory," in *IEEE Microw. Symp. Dig*., Jun. 2001, pp. 1297–1300.

[5] K. Song and Q. Xue, "Novel ultra-wideband (UWB) multilayer slotline power divider with bandpass response," *IEEE Microw. Wireless Compon. Lett*., vol. 20, no. 1, pp. 13–15, Jan. 2010.

[6] M. A. Maktoomi, M. S. Hashmi, and F. M. Ghannouchi, "Theory and design of a novel wideband DC isolated Wilkinson power divider," *IEEE Microw. Wireless Compon. Lett.,* vol. 26, no. 8, pp. 586–588, Aug. 2016.

[7] W.-J. Feng, Y. Zhang and W.-Q. Che, "Tunable Dual-Band Filter and Diplexer Based on Folded Open Loop Ring Resonators," *IEEE Trans. Circuits Syst. II Exp. Briefs,* vol. 64, no. 9, pp. 1047-1051, 2017.

[8] T.Zhang and W.-Q. Che, "A compact Tunable Power Divider With Wide Tuning Frequency Range and Good Reconfigurable Resources," *IEEE Trans. Circuit Syst.II, Exp. Briefs,* vol. 63, no. 11, pp. 1054-1058, 2016.

[9] W.-D. Lin, R.-C. Liu, B.-L. Chen, P.-H. Deng and S.-F. Chao, "A Wilkinson power divider with transmission zero in desired stopband using embedded parallel resonator," in *Microwave Conference (APMC), 2014 Asia-Pacific*, Sendai, Japan , 2015.

[10] S.-Y. Hu, K. Song, and Y. Fan, "Planar ultra-wideband eight way power divider with improved isolation bandwidth," in *Microwave Confrence (APMC)*, Asia-Pacific. vol 2. IEEE, 2015.

[11] Mohammad A. M, Mohammad S. H and Fadhel M. G, "Theory and Design of a Novel Wideband DC Isolated," *Microwave and Wireless,* vol. 26, no. 8, pp. 586-588, 2016.

[12] M. Elsbury et al., "Integrated broadband lumped-element symmetrical hybrid N-way power dividers," in *IEEE IMS Dig*., Jun. 2009.

[13] C. Zhu, W. Kang and W. Wu, "Quasi-lumped dual-mode reconfigurable eight-way FPD," *Electronic Lett.* Vol: 53, no. 25, pp1657-1659, 2017.

[14] R. Kazemi and A. E. Fathy, ''Design of a wideband eight-way single ridge substrate integrated waveguide power divider,'' *IET Microw. Antenna Propag*., vol. 9, no. 7, pp. 648–656, Jul. 2015.

[15] T. Yu, "Design of Length-Saving Multiway Wilkinson Power Dividers," *IEEE Access*, vol:6, pp:14093-14105. March, 2018.

Chapter 4 A Horst-type PD with Wide Frequency Tuning Range Using Varactors

This chapter presents a novel PD with a wide frequency tuning range. In the previous work that presented in Chapter 3, a pair of capacitors were connected in parallel with the front transmission lines of a Trantanella-type PD introducing an additional reflection minimum together with the original reflection zero to broaden the bandwidth. In this design, the latter transmission lines are removed. The added capacitors generate a reflection minimum which can be easily controlled by varactors. Thus, the frequency band of the PD can be flexibly tuned by altering the varactors. Design parameters are carefully chosen to eliminate the effect of the original reflection zero. By doing so, the PD will have a tunable centre frequency instead of a tunable bandwidth. Theoretical formulas for the characteristic impedances and electric lengths of the transmission lines of the PD are derived and analyzed. A PD has been designed and fabricated to demonstrate the validity of the proposed design. The measured results indicate that the PD can achieve a frequency tuning range of 0.9-4.2 GHz ($\boldsymbol{f_H/f_L}$= 4.67:1), with in-band input and output return losses both better than 22 dB, and an insertion loss S_{21} of 3.2-4 dB. The measured in-band isolation is better than 15 dB. The PD has a simple layout and a compact size of $0.2\boldsymbol{\lambda_g} \times 0.16\boldsymbol{\lambda_g}$which demonstrates the excellent potential of the proposed PD for modern communication systems.

4.1 Introduction

Modern communication systems usually need to support multi-standard communications, which require the components with multiple operational bands. PDs are essential components in communication systems for power splitting and combining. The features of a PD regarding the operational frequency band, input/output return loss, and isolation between the output ports will significantly affect the overall performance of the communication system. Although many designs [1], [2], [3] of multi-band PDs have been reported, their circuit size is usually bulky. Modern wireless communication prefers tunable RF components instead of multiplexing into separated frequency bands due to the size and cost reduction. As the demand for spectrally cognitive microwave system is rising, more and more researches are focusing on frequency

agile devices, such as reconfigurable couplers [4], resonators and filters [5]-[9]. With the rapidly increasing demands on multi-band feature of the PDs, there is growing attention paid on PDs with compact size and wide tunable frequency ranges. Filtering tunable PDs [10]-[12] have been investigated over the past years. In these designs, a filter and a PD are cascaded to achieve filtering PD response. The filter replaces the quarter-wavelength transmission lines in Wilkinson PDs. The main contribution of such designs is to provide a filtering response to the PDs. However, there are drawbacks. The insertion loss is relatively high (1.8-2.4 dB) due to the limited unloaded quality factor of microstrip resonators. Moreover, the port matching and isolation conditions are usually not satisfactory. To maintain better performance in the entire tunable frequency band, [13] [14] introduced coupled-line tunable Wilkinson PDs which have excellent input and output matching ($|S_{11}|, |S_{22}| < -17$ dB) and isolation ($|S_{23}| < -25$ dB). The aforementioned PDs are good to be used in many filtering PD applications. However, the limitation of the 20 dB tuning range (normally less than 2:1) is still a challenge. Modern transceivers like software defined radios require a wide range of radio spectrum. The designs in [15] and [16] have a tunable frequency range of 2.9:1 by employing short-electrical transmission lines along with a shunt varactor to the Wilkinson-type PD, but no analytical solutions to describe the relationship of capacitance and the corresponding frequency were provided.

A novel PD with a wide frequency tuning range and a compact footprint is presented in this section. Similar to [17], a pair of varactors are introduced in parallel with the front transmission lines. The main difference is that the design in [17] has an extra pair of transmission lines that connect the outputs with the isolation networks so that the varactors can tune the frequency tuning range of the divider. The proposed divider in this work utilises a Horst Divider structure [18], [19] to simplify the calculation. In this design, the extra transmission lines were removed to eliminate the original reflection-zero in [17] and maintain the additional reflection minimum which is introduced by the varactors. As a result, the proposed design can achieve a very wide frequency tuning range. The reflection minimum is very sensitive to the capacitance change. The centre frequency of the operational band can be defined as the frequency of the corresponding reflection minimum. The centre frequency moves along a locus. In other words, the centre frequency tuning range can be controlled flexibly by the varactors. An example in this chapter demonstrated an available frequency tuning range of 0.9-4.2 GHz by tuning the

varactors. Excellent output return loss and isolation response are retained over the whole tuning range.

Moreover, good physical isolation between two output ports can be realised by using a Horst structure which is a pair of short-length-transmission lines connected between the front transmission lines and the isolation circuit. Excellent physical isolation not only separates two output ports but also suppresses the undesirable coupling between them. The design equations and analysis of the proposed structure are presented in Section 4.2. Then the parametric studies regarding tuning range are discussed in Section 4.3. In Section 4.4, a prototype of the proposed PD is fabricated and measured to validate the proposed theory. In the end, conclusions will be drawn in Section 4.5.

4.2 Analytical Design Equation for the Proposed Horst-type PD

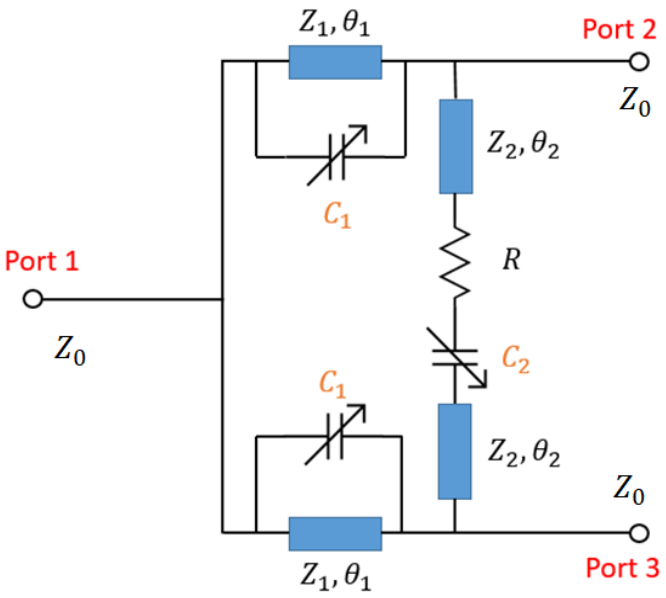

Fig. 4. 1 Structure of the proposed Horst-type PD.

Fig. 4. 1 presents the equivalent circuit of the proposed two-way reconfigurable PD. A pair of varactors are added in parallel to the main transmission lines to realise tunability, and a single varactor is inserted in the isolation circuit to compensate the output return losses and isolation. As **Fig. 4. 1** shows, Z_0 represents the port impedance. Z_1 and Z_2 are the characteristic impedances of the front transmission lines and the transmission lines in the isolation circuit,

respectively. C_1 represents the capacitance of the added varactors on the front transmission lines, C_2 is the capacitance of the varactor on the isolation circuit connected in series with a resistor. The electrical lengths of the transmission lines are defined as θ_1 and θ_2 at frequency f in the same way as θ_0 at the centre frequency f_0. The relationship among the characteristic impedances, electrical lengths of the transmission lines and the varactors can be derived by an even-mode analysis method. To design the isolation circuit, the odd-mode analysis method can be applied to calculate the lumped resistor R and varactor C_2.

4.2.1 Even-mode Analysis

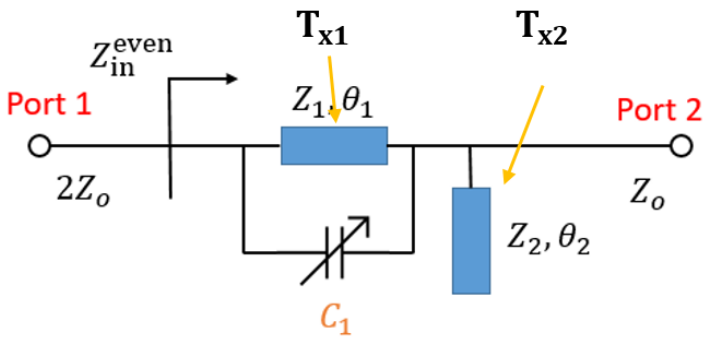

Fig. 4. 2 The equivalent circuit of the proposed structure for even-mode analysis.

The even-mode equivalent circuit of the proposed PD is depicted in **Fig. 4. 2**. The normalised ABCD matrix of the structure is used to calculate the total input impedance of the circuit. The normalised ABCD matrix for the network of the front transmission line with parallel-loaded capacitors can be obtained referring to (3.4) in Chapter 3.

$$\left|\begin{matrix}\bar{A} & \bar{B}\\ \bar{C} & \bar{D}\end{matrix}\right|_{C_p+\mathrm{Tx1}} = \left|\begin{matrix}\dfrac{j\bar{Y}-\dfrac{j}{\overline{Z_1}\cdot\tan(\theta_1\bar{f})}}{j\bar{Y}-\dfrac{j}{\overline{Z_1}\cdot\sin(\theta_1\bar{f})}} & \dfrac{1}{j\bar{Y}-\dfrac{j}{\overline{Z_1}\cdot\sin(\theta_1\bar{f})}}\\ \dfrac{\left(j\bar{Y}-\dfrac{j}{\overline{Z_1}\cdot\tan(\theta_1\bar{f})}\right)^2-\left(j\bar{Y}-\dfrac{j}{\overline{Z_1}\cdot\sin(\theta_1\bar{f})}\right)^2}{j\bar{Y}+\dfrac{j}{\overline{Z_1}\cdot\sin(\theta_1\bar{f})}} & \dfrac{j\bar{Y}-\dfrac{j}{\overline{Z_1}\cdot\tan(\theta_1\bar{f})}}{j\bar{Y}-\dfrac{j}{\overline{Z_1}\cdot\sin(\theta_1\bar{f})}}\end{matrix}\right| \tag{4.1}$$

Where $\overline{Y} = 2\pi\,\overline{f}\cdot\overline{C_1}$

The ABCD matrix for the other transmission line can be expressed as

$$\left|\begin{matrix}\bar{A} & \bar{B}\\ \bar{C} & \bar{D}\end{matrix}\right|_{\mathrm{Tx2}} = \left|\begin{matrix}1 & 0\\ j\frac{\tan(\theta_3 \bar{f})}{\bar{Z_3}} & 1\end{matrix}\right| \tag{4.2}$$

$$\left|\begin{matrix}\overline{A} & \overline{B}\\ \overline{C} & \overline{D}\end{matrix}\right| = \left[\begin{matrix}\dfrac{\overline{Y}-\dfrac{1}{\overline{Z_1}\tan(\theta_1\overline{f})}}{\overline{Y}-\dfrac{1}{\overline{Z_1}\sin(\theta_1\overline{f})}} & \dfrac{1}{j\left(\overline{Y}-\dfrac{1}{\overline{Z_1}\sin(\theta_1\overline{f})}\right)}\\ \dfrac{\left(\overline{Y}-\dfrac{1}{\overline{Z_1}\sin(\theta_1\overline{f})}\right)^2-\left(\overline{Y}-\dfrac{1}{\overline{Z_1}\tan(\theta_1\overline{f})}\right)^2}{j\left(\overline{Y}-\dfrac{1}{\overline{Z_1}\sin(\theta_1\overline{f})}\right)} & \dfrac{\overline{Y}-\dfrac{1}{\overline{Z_1}\tan(\theta_1\overline{f})}}{\overline{Y}-\dfrac{1}{\overline{Z_1}\sin(\theta_1\overline{f})}}\end{matrix}\right]\cdot\left[\begin{matrix}1 & 0\\ j\frac{\tan(\theta_2\overline{f})}{\overline{Z_2}} & 1\end{matrix}\right] \tag{4.3}$$

where the frequency f is normalised to 1 GHz. The terminal impedance Z_0 is normalised to 1, impedances Z_1 and Z_2 are normalised to Z_0, respectively. The normalised $\overline{C_1}$ equals to $C_1 \cdot Z_0$. The normalised input impedance of the circuit can be calculated by using the ABCD matrix as:

$$\overline{Z_{in}}^{\,\mathrm{even}} = \frac{\overline{\mathrm{A}}\cdot 1+\overline{B}}{\overline{C}\cdot 1+\overline{D}} \tag{4.4}$$

And the magnitude of the return loss can be expressed as:

$$|\mathrm{S}_{11}| = \left|\frac{\overline{\mathrm{A}}+\overline{B}/1-\overline{C}\cdot 1-2\cdot\overline{D}}{\overline{\mathrm{A}}+\overline{B}/1+\overline{C}\cdot 1+2\cdot\overline{D}}\right| = \sqrt{\frac{c^2+d^2}{a^2+b^2}} \tag{4.5}$$

where

$$\begin{cases} a = \left(\left(1\text{-}2\overline{P}\overline{Y}\right)\overline{Z_1}^{\,2}+2\right)\sin(\theta_1\overline{f})+\overline{Z_1}\left(\left(4\overline{Y}+2\overline{P}\right)\cos(\theta_1\overline{f})+4\overline{Y}\right)\\ b = \left(3\overline{Y}+\overline{P}\right)\overline{Z_1}^{\,2}\sin(\theta_1\overline{f})-3\cos(\theta_1\overline{f})\overline{Z_1}^{\,2}\\ c = \left(\left(2\overline{P}\overline{Y}+1\right)\overline{Z_1}^{\,2}-2\right)\sin(\theta_1\overline{f})+\overline{Z_1}\left(4\overline{Y}-\left(4\overline{Y}+2\overline{P}\right)\cos(\theta_1\overline{f})\right)\\ d = \left(\overline{P}-\overline{Y}\right)\overline{Z_1}^{\,2}\sin(\theta_1\overline{f})+\overline{Z_1}\cos(\theta_1\overline{f})\end{cases}$$

$$\overline{P} = \frac{\tan(\theta_2\overline{f})}{\overline{Z_2}}$$

The $|S_{11}|$ in (4.5) equals to zero if the input terminal is perfectly matched at $\overline{f_Z}$. Hence, the relationship between impedance $\overline{Z_1}, \overline{Z_2}$ and the zero-reflection frequency $\overline{f_Z}$ can be expressed by:

$$\overline{Z_1} = \frac{\left(2\overline{P} + \sqrt{8\overline{P}^2 + 2}\right)\sin(\theta_1 \overline{f_Z})}{\left(\cos(\theta_1 \overline{f_Z}) + 1\right) \cdot \left(2\overline{P}^2 + 1\right)} \tag{4.6}$$

(4.6) gives the equation for determining $\overline{Z_1}$ and $\overline{Z_2}$, and values that satisfy the equation can produce a reflection-zero at $\overline{f_Z}$. Let θ_1 and θ_2 be independent variables that varying from 0° to 90°. Since θ_1 is the electrical length of the main transmission line, it can be assigned to determine the proper tuning band. While θ_2 should be chosen from small values such as $0^\circ \leq \theta_2 \leq 20^\circ$ to simplify the layout for practical applications. Moreover, it is necessary to bend the front transmission lines for placing the varactors in parallel with them, and to achieve a compact size of the topology. Hence, the ratio of length and width for the front transmission lines need to be sufficiently large for bending. Specifically, a larger θ_1 indicates longer transmission lines while lager $\overline{Z_1}$ implies narrower width of the transmission lines. Therefore, θ_1 and $\overline{Z_1}$ should be chosen appropriately for fabrication purposes.

4.2.2 Odd-mode Analysis

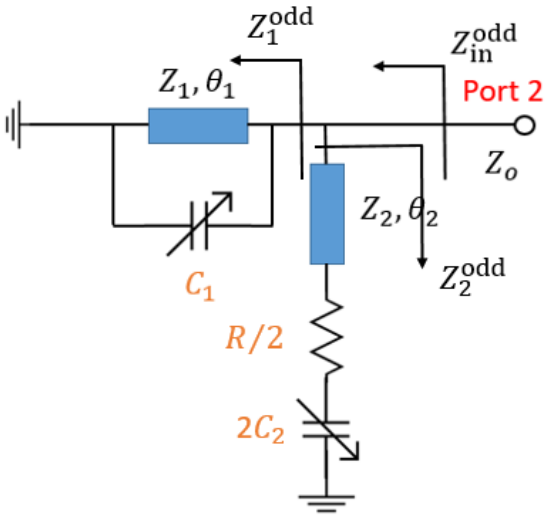

Fig. 4. 3 The equivalent circuit of the proposed structure for the odd-mode analysis.

To determine the parameters in the isolation circuit, odd-mode analysis is adopted. The odd-mode equivalent circuit of the PD is shown in **Fig. 4. 3**. The normalized input impedance for the odd-mode equivalent circuit is denoted by $\overline{Z_{\text{in}}^{\text{odd}}}$, and the total impedance can be seen as $\overline{Z_1^{\text{odd}}}$ and $\overline{Z_2^{\text{odd}}}$ is in parallel.

$$\overline{Z_1^{\text{odd}}} = \frac{\frac{j\overline{Z_1}\tan(\theta_1\overline{f_Z})}{j\overline{Y}}}{j\overline{Z_1}\tan(\theta_1\overline{f_Z})+\frac{1}{j\overline{Y}}} \tag{4.7}$$

$$\overline{Z_2^{\text{odd}}} = \overline{Z_2}\frac{\frac{\overline{Z_{\text{ISO}}}}{2}+j\overline{Z_2}\tan(\theta_2\overline{f_Z})}{\overline{Z_2}+j\frac{\overline{Z_{ISO}}}{2}\tan(\theta_2\overline{f_Z})} \tag{4.8}$$

where $\overline{Z_{\text{ISO}}} = \bar{R}/2 + 1/(2\pi\overline{f_z}\overline{C_1})$. The input impedance of Port 2 can be derived.

$$\overline{Z_{\text{in}}^{\text{odd}}} = \frac{\overline{Z_1^{\text{odd}}}.\overline{Z_2^{\text{odd}}}}{\overline{Z_1^{\text{odd}}}+\overline{Z_2^{\text{odd}}}} \tag{4.9}$$

To guarantee perfect impedance matching at outputs, the following conditions should be satisfied.

$$\begin{cases} \text{Re}\left(\overline{Z_{in}^{odd}}\right)=1 \\ \text{Im}\left(\overline{Z_{in}^{odd}}\right)=0 \end{cases} \tag{4.10}$$

By substituting design parameters to (4.10), the total impedance of the isolation circuit can be calculated as:

$$\overline{Z_{ISO}} = \frac{2\overline{Z_2}[(j+\omega\overline{C_1})\overline{Z_1}\overline{Z_2}\tan(\theta_1\overline{f_Z})^2-\overline{Z_1}\tan(\theta_1\overline{f_Z})-\overline{Z_2}\tan(\theta_2\overline{f_Z})]}{-\overline{Z_1}\overline{Z_2}\tan(\theta_1\overline{f_Z})+j(\overline{Z_1}\tan(\theta_1\overline{f_Z})^2+\omega\overline{C_1}\overline{Z_1}\overline{Z_2}\tan(\theta_1\overline{f_Z})-\overline{Z_2})} \tag{4.11}$$

Thus, the capacitance $\overline{C_2}$ and resistance $\bar{R}$ in the isolation circuit can be obtained by solving:

$$\begin{cases} \text{Re}\left(\overline{Z_{\text{ISO}}}\right)=\overline{R}/2 \\ \text{Im}\left(\overline{Z_{ISO}}\right)=1/2\omega\overline{C_2} \end{cases} \tag{4.12}$$

Since $\overline{Z_1}$, $\overline{Z_2}$, θ_1 and θ_2 have been chosen from the even-mode analysis, hence a proper range of $\overline{C_2}$ can be determined by substituting different values of capacitance $\overline{C_1}$ to (4.11).

4.3 Design Method

To extend the matching bandwidth, the value of $\overline{Z_1}$ could be changed from the calculated result of (4.6). For a given frequency $\overline{f_z}$, values of $\overline{Z_1}$ and $\overline{Z_2}$ that satisfy equation (4.6) can generate one reflection-zero at $\bar{f}_z$. However, if $\overline{Z_1}$ changes, $|S_{11}|$ will not be equal to zero at the frequencies near $\overline{f_z}$, but it can be kept very low so that the frequency tuning range can be extended. The following sections will discuss the effect on the tuning range in terms of the impedance $\overline{Z_1}$, $\overline{Z_2}$ and capacitance $\overline{C_1}$. Also, a design guidance is provided at the end of this section.

4.3.1 Determination of Impedance $\overline{Z_1}$ and $\overline{Z_2}$

For the proposed reconfigurable PD, continuously changing the capacitance $\overline{C_1}$ will result in consecutive S_{11} pass bands. Every single response band has a frequency minimum, $\overline{f_m}$ (normally the centre frequency of the tunable band). Thus, continuously tuning $\overline{C_1}$ can produce consecutive frequency minima which form an envelope curve of $|S_{11}|$. The frequency tuning range can be determined referring to the envelope curve as it records the movement of the $|S_{11}|$ trough over the whole operating band. To improve the impedance matching range, the input impedance should approximately equal to the load impedance over a wide frequency range. This section discusses how to enhance the adaptive frequency range by choosing appropriate values of $\overline{Z_1}$ and $\overline{Z_2}$.

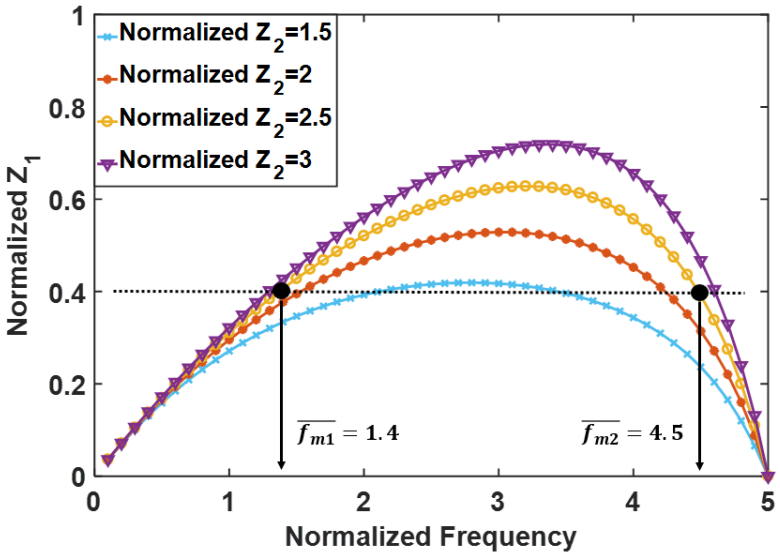

Fig. 4. 4 Theoretical reflection-zero frequency curve with changing Z_1 and Z_2.

Taking $\theta_1 = 30^o$, $\theta_2 = 18^o$ and $\overline{Z_2}$ =3 as an example, **Fig. 4. 4** depicts several calculated curves based on (4.6) which represent the relationship between $\overline{Z_1}$, $\overline{Z_2}$ and the zero-reflection frequencies. Curves with four different values of $\overline{Z_2}$ range from 1.5 to 3 are plotted here. If $\overline{Z_1}$ and $\overline{Z_2}$ have only one intersection point then there is only one zero-reflection frequency, and in this case $\overline{Z_1} = \bar{Z}_{\text{matched}}$. Maintaining $\overline{Z_2}$, and slightly decrease $\overline{Z_1}$, two intersection points will appear, as a result, the approximate matching range is extended. For example, the intersection points of $\overline{Z_1} = 0.4$ and $\overline{Z_2} = 2.5$ have corresponding frequencies $\overline{f_{m1}} = 1.4$ and $\overline{f_{m2}} = 4.5$ which indicates that $\overline{f_{m1}}$ and $\overline{f_{m2}}$ are the zero-reflection frequencies over the whole tuning range. Theoretically, the wider these two frequencies apart, the wider the approximate matching range can be. When $\overline{Z_2} = 1.5$, $\overline{Z_1}$ should employ a value between 0.2 and 0.4 to have two intersection points on the curve as shown in **Fig. 4. 4**, otherwise there will be no approximate matching over the operating band. Although the large gap between these two frequencies indicates a wide tuning range, such small $\overline{Z_1}$ ($\overline{Z_1} = 0.2\sim0.4$) indicate large width of the transmission lines which makes it more difficult to connect with the varactors.

4.3.2 Frequency Tuning Range Regarding $\overline{C_1}$

This section discusses the relationship between the value of the loaded capacitors $\overline{C_1}$ and the corresponding centre operating frequency $\overline{f_m}$. The design in [17] has a reflection minimum at around the original frequency and an additional reflection-zero introduced by the capacitors.

Thus, there will be two reflection minima in the passband, and the frequency bandwidth can be tuned by changing the capacitance of the capacitors. The difference of the proposed work here is that, by properly choosing $\overline{Z_1}$, $\overline{Z_2}$, θ_1 and θ_2, this design only retains the reflection minimum introduced by the loaded capacitors. As a result, instead of having a tunable bandwidth as in [17], this design will have a tunable centre frequency by changing the capacitance.

As the S_{11} curves in **Fig. 4. 5**(a)-(d) illustrate, the reflection minimum frequency $\overline{f_m}$ is a function of $\overline{C_1}$. By choosing an appropriate $\overline{C_1}$, a minimum $|S_{11}|$ at the chosen frequency can be generated. Since each S_{11} curve has only one trough which is the reflection minimum, the expression of the S_{11} envelope curve can be calculated based on the derivation of $|S_{11}|$ regarding frequency. In this case, to find the corresponding capacitance $\overline{C_1}$ and the reflection minimum frequency $\overline{f_m}$, the derivative of $|S_{11}|$ should be zero at $\overline{f_m}$:

$$\frac{d\left|S_{11}\right|}{d\overline{C_1}} = 0 \tag{4.13}$$

Which gives (4.14).

$$\overline{C_1} = \frac{1}{8}\cdot\frac{\left(-2\overline{P}\overline{Z_1}^2+8\overline{Y}\right)\overline{Z_1}\cos(\theta_1\overline{f_m})^2+\left(\left(4+\overline{P}^2\overline{Z_1}^4+\overline{Z_1}^4-4\overline{P}^2\overline{Z_1}^2-5\overline{Z_1}^2\right)\sin(\theta_1\overline{f_m})-\overline{P}\overline{Z_1}\left(\overline{Z_1}^2+4\right)\right)\cos(\theta_1\overline{f_m})+\left(\left(\overline{P}^2+1\right)\overline{Z_1}^4-4\right)\sin(\theta_1\overline{f_m})+\overline{P}\overline{Z_1}^3-4\overline{P}\overline{Z_1}}{\pi\overline{f_m}\overline{Z_1}\left(\left(\left(\overline{P}^2+\frac{5}{4}\right)\overline{Z_1}^2-2\right)\cos(\theta_1\overline{f_m})^2+\left(4-\frac{1}{4}\overline{P}\overline{Z_1}\left(Z_1^2-12\right)\sin(\theta_1\overline{f_m})\right)\cos(\theta_1\overline{f_m})-\frac{1}{4}P\overline{Z_1}\left(\overline{Z_1}^2+12\right)\sin(\theta_1\overline{f_m})-2-\left(\overline{P}^2+\frac{5}{4}\right)\overline{Z_1}^2\right)} \tag{4.14}$$

The relationship of $\overline{C_1}$ and $\overline{f_m}$ as shown in (4.14) indicates the correlation of the capacitance range and the frequency tuning range. To further reveal the relationship between $|S_{11}|$ and reflection minima frequencies $\overline{f_m}$, the envelope of $|S_{11}|$ needs to be derived. As $\overline{f_m}$ is a dependent variable of $\overline{C_1}$ in (4.13), so $\overline{C_1}$ can be replaced by substituting (4.13) to (4.5). Thus, the envelope of $|S_{11}|$ can be expressed by:

$$\left|S_{11}\right|_{envelope} = \frac{2c\cdot\left(\overline{Y}\,\overline{Z_1}^2\sin(\theta_1\overline{f_m})+\overline{Z_1}\left(1-\cos(\theta_1\overline{f_m})\right)\right)-d\cdot\overline{Z_1}^2\sin(\theta_1\overline{f_m})}{-2a\cdot\left(\overline{Y}\,\overline{Z_1}^2\sin(\theta_1\overline{f_m})+\overline{Z_1}\left(1-\cos(\theta_1\overline{f_m})\right)\right)+3b\cdot\overline{Z_1}^2\sin(\theta_1\overline{f_m})} \tag{4.15}$$

where a, b, c, d and $\overline{Y}$ can be found in (4.1) and (4.5).

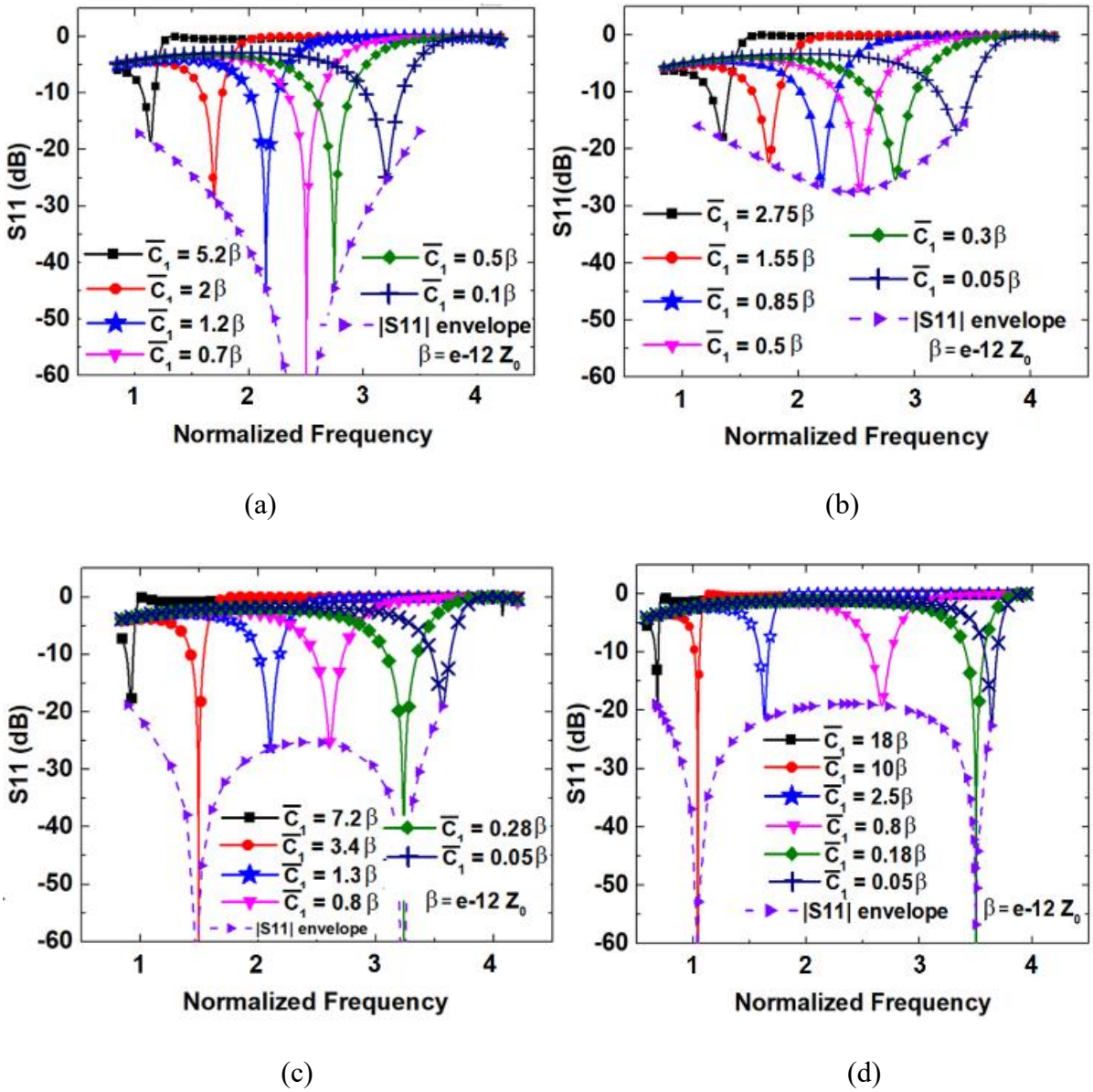

Fig. 4. 5 Theoretical S11 envelope curves as a function of $C_1$for different impedance of front transmission lines for (a) α=1, (b) α=1.15, (c) α=0.85 and (d) α=0.6.

By only changing the impedance $\overline{Z_1}$ while $\overline{Z_2}$ is fixed, the frequency tuning range of PD changes regularly. **Fig. 4. 5**(a)-(d) depicts six sampled $|S_{11}|$ curves with different values of $\overline{C_1}$. A dash line that is so called 'envelope curve', is drawn to illustrate the troughs of $|S_{11}|$ curves over the whole frequency band. The envelope curve is a group of reflection minima that records the movement locus of minimum values $|S_{11}|_{\min}$ when $\overline{C_1}$ is changing, and other parameters remain the same. Let $\overline{Z_1}$= α· $\bar{Z}_{\text{matched}}$, or α=1, where α is a rational factor. **Fig. 4. 5**(a) represents that when $\overline{Z_1} = \bar{Z}_{matched}$, there is only one zero-reflection point over the tuning

range. In this case, the centre frequency tuning range is relatively narrow. If α increases, for instance, α=1.15, the reflection-zero disappears and the minimum of the S_{11} envelope will be worse, and the tuning range will shrink as shown in **Fig. 4. 5** (b). Conversely, there will be two reflection-zeros on the S_{11} envelope curve if α decreases from 1 (e.g. α=0.85, 0.6) as shown in **Fig. 4. 5**(c) (d). In this case, the frequency tuning range can be extended by controlling the distance between the two reflection-zeros. A larger distance between the two minima leads to a wider frequency tuning range. However, it should be noted that the S_{11} between the two zeros will be sacrificed.

4.3.3 Tuning range of the tunable PD

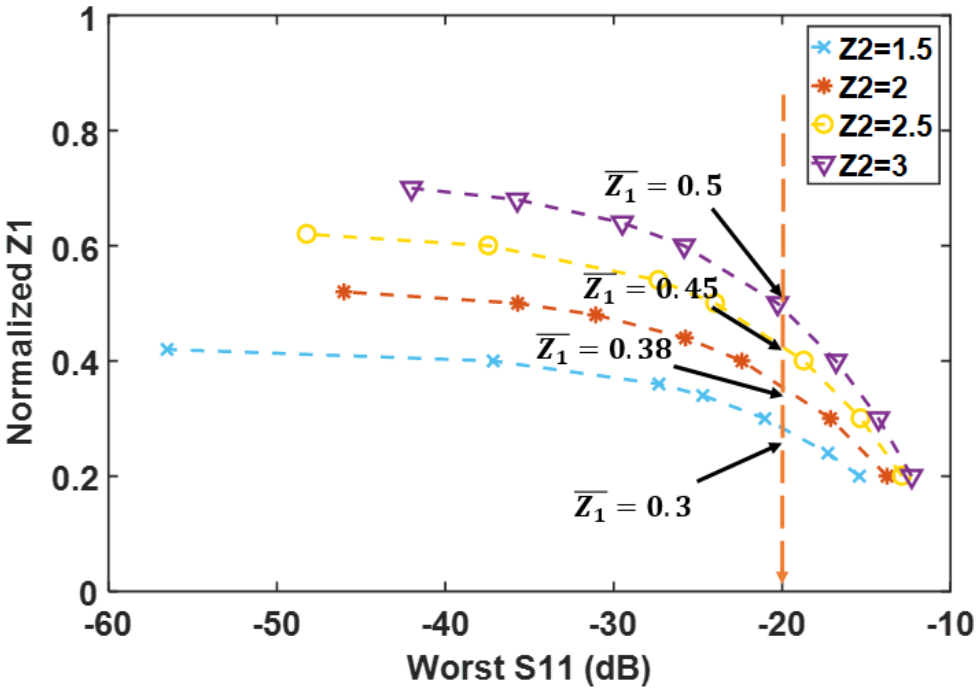

Fig. 4. 6 The relationship between the worst in-band S_{11} and changing $\overline{Z_1}$.

The worst in-band $|S_{11}|$ is the other crucial factor that needs to be considered for bandwidth calculations. Although large difference between the two reflection-zeros indicates a wide tuning range, the S_{11} envelope should be better than a specified value. For example, if S_{11} is expected to be better than 20 dB, α should be greater than 0.6 because $|S_{11}|$ at the centre frequency will exceed 20 dB as shown in **Fig. 4. 5**(d) if α is smaller than 0.6, which does not meet the design specification. Mathematically, the worst in-band S_{11} can be calculated by

taking the derivative of the S_{11} envelope. Due to the complexity of the calculation, **Fig. 4. 6** can be used to give a picture of how the worst in-band S_{11} varies with a changing $\overline{Z_1}$ for different $\overline{Z_2}$. The curves in **Fig. 4. 6** are plotted in Matlab based on four sets of calculations. By substituting $\theta_1 = 30^o$, $\theta_2 = 18^o$, and $\overline{Z_2}$ ($\overline{Z_2} = 1.5, 2, 2.5$ and 3) into (4.15), the envelope of $|S_{11}|$ can be expressed as a function of the reflection minimum frequency $\overline{f_m}$ and $\overline{Z_1}$. Sweeping $\overline{Z_1}$ from 0.2 to 0.8 in Matlab, the corresponding worst in-band S_{11} can then be obtained using the derivation of $|S_{11}|_{envelope}$ regarding $\overline{f_m}$. For a fixed $\overline{Z_2}$, the smaller $\overline{Z_1}$ is, the higher the in-band S_{11} will be, because a smaller $\overline{Z_1}$ results in a wider frequency difference between the two reflection zeros. It can also be observed that a smaller $\overline{Z_2}$ will result in a wider frequency difference with a fixed $\overline{Z_1}$. Since 20 dB is often the desired in-band S_{11} value in PD design, a vertical marker line is drawn and the four interception points are $\overline{Z_1} = 0.3, \overline{Z_2} = 1.5$, $\overline{Z_1} = 0.38, \overline{Z_2} = 2$, $\overline{Z_1} = 0.45, \overline{Z_2} = 2.5$, and $\overline{Z_1} = 0.5$, $\overline{Z_2} = 3$, respectively. With these impedance combinations, the worst in-band value of the $|S_{11}|$ envelope is exactly 20 dB, to make full use of the tuning band. Nevertheless, the frequency tuning ranges for these four sets of impedances are different, the largest tuning range in this case is realized when $\overline{Z_1} = 0.3, \overline{Z_2} = 1.5$ referring to the previous discussion.

Another factor that affects the frequency tuning range of the PD is the capacitance tuning range of the varactors. **Fig. 4. 7** shows an example of the tuning range. The two curves imply that the frequency tuning range of the PD varies as a function of the required capacitance for varactor $\overline{C_1}$ and $\overline{C_2}$. The blue curve exhibits the tuning range of $\overline{C_1}$. The capacitance versus reflection minimum frequency can be solved using Matlab by substituting $\overline{Z_1}$ = 0.4, $\overline{Z_2}$ = 2, and θ_1 = 30°, θ_2 = 18° to (4.14). Once the tuning range of $\overline{C_1}$ is determined, substituting $\overline{C_1}$ together with $\overline{Z_1}$,$\overline{Z_2}$, θ_1 and θ_2 to (4.11) will give the relationship between $\overline{Z_{ISO}}$ and $\overline{f_m}$. According to (4.12), the tuning range of $\overline{C_2}$ can be worked out by extracting the imaginary part of $\overline{Z_{ISO}}$. By specifying $|S_{11}|$, the specified maximum operating frequency $\overline{f_{\max}}$ and the minimum operating frequency$\overline{f_{\min}}$, the corresponding $\overline{C_{1\min}}$ and $\overline{C_{1\max}}$ can be found using (4.12) and (4.13). To simplify the design process, $\overline{C_{1\min}}$ and $\overline{C_{1\max}}$ can be found from **Fig. 4. 7** by specifying $\overline{f_{\max}}$ and $\overline{f_{\min}}$,, then $|S_{11}|$ will be evaluated if it is better than the specified value at $\overline{f_{\max}}$ and $\overline{f_{\min}}$,. The frequency tuning range depends on the tuning range of the varactors while it is usually limited by the mechanism of the varactor diodes. Although a wide frequency tunable range can be achieved theoretically, the range will be limited by the capacitance range of the varactors in

practice. In that case, the required $\overline{C_{1\min}}$ and $\overline{C_{1\max}}$ for $\overline{f_{\max}}$ and $\overline{f_{\min}}$, should be in the capacitance tuning rage of the commercial varactors or as much as possible.

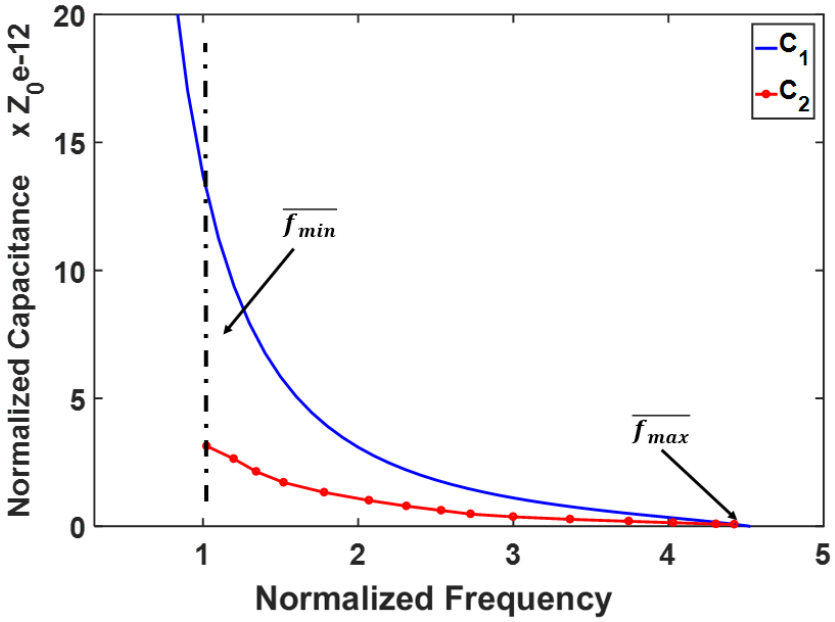

Fig. 4. 7 Theoretical required capacitance $\overline{C_1}$ and $\overline{C_2}$ versus corresponding frequency with $\overline{Z_2}$ =2 when $\overline{Z_1}$=0.4, $\theta_1 = 30°$ and $\theta_2 = 18°$.

4.3.4 Design Guidance

The design procedure of the proposed tunable PD can be summarized as follows.

1) Specify the desired frequency range $\overline{f_{\min}}$ and $\overline{f_{\max}}$.

2) Choose appropriate θ_1 and θ_2 based on the desired frequency range. Determine $\overline{Z_1}$ and $\overline{Z_2}$ referring to (4.6) and **Fig. 4. 4**, making sure the chosen frequency range is slightly wider than the two reflection-zero frequencies. Besides, ensure that the worst in-band S_{11} would meet the specification.

3) Verify if $|S_{11}|$ at $\overline{f_{\max}}$ and $\overline{f_{\min}}$would satisfy the specification based on (4.14) and (4.15). If not, choose other values for θ_1 and θ_2 and repeat design procedure from step 2).

4) Calculate the required capacitance range for varactor $\overline{C_1}$.

5) The resistance $\bar{R}$ and capacitance $\overline{C_2}$ on the isolation circuit can be calculated by substituting all previous design parameters into (4.11) and (4.12). The required tuning range of $\overline{C_2}$ on the isolation circuit can be estimated if $\overline{C_1}$ and the corresponding frequency f are specified.

6) Choose varactors that can achieve the required tuning ranges of $\overline{C_1}$ and $\overline{C_2}$.

7) After obtaining these parameters, implement the PD with distributed elements and optimize the physical dimensions with the aid of EM simulation tools. Bias circuits will also be added to tune the varactors in the measurement.

4.4 Fabrication and Measurement

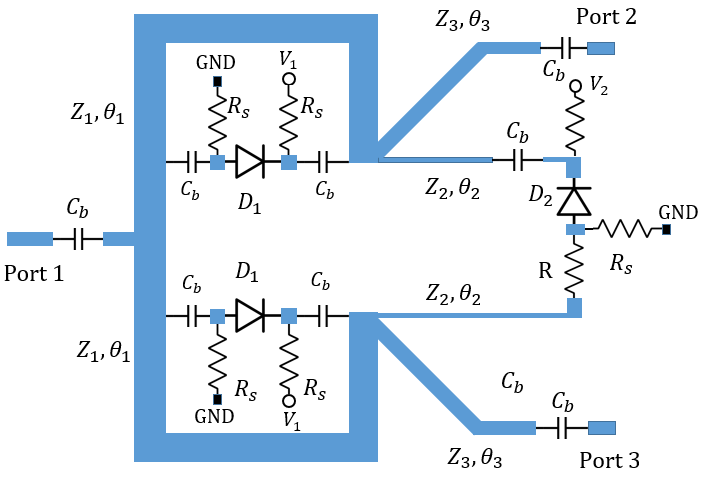

(a)

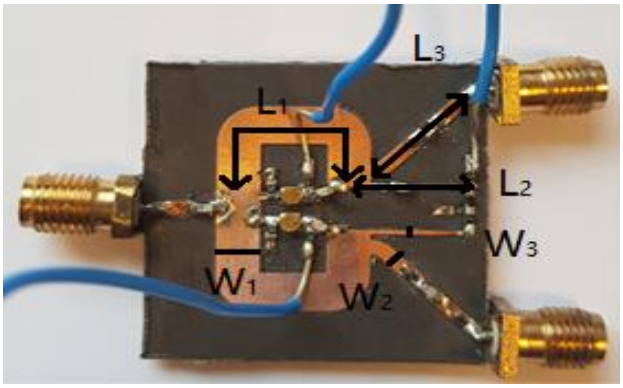

(b)

Fig. 4. 8 (a) Configuration of the proposed PD and (b) photo of the fabricated PD.

Table 4. 1 DESIGN PARAMETERS OF THE PROTOTYPE TUNABLE POWER DIVIDER.

W_1(mm)	4.3	C_1 (pF)	5.1-0.01
W_2(mm)	2.3	C_2 (pF)	2.1-0.2
W_3(mm)	0.5	R (Ω)	100
L_1(mm)	21	V_1 (V)	1.7-20
L_2(mm)	7	V_2 (V)	0-20
L_3(mm)	12		

One prototype tunable PD with a frequency tuning range from 1 GHz to 4.2 GHz was designed and fabricated for the validation of the proposed method. Based on the desired tuning range, the electric lengths of the front and isolation transmission lines are $\theta_1 = 30^{\circ}$and $\theta_2 = 18^{\circ}$ at 1 GHz. According to (4.6), $\overline{Z_1} = 0.4$ and $\overline{Z_1} = 2.4$ are selected in the design. Hence the characteristic impedances are $Z_1 = 20.3\ \Omega$ and $Z_2 = 120\ \Omega$. The corresponding $|S_{11}|$ at 1 GHz and 4.2 GHz are both lower than -20 dB. Then the required capacitance range for C_1 is obtained to be 0-7.9 pF. Theoretically, as shown in **Fig. 4. 5**(d), the achievable frequency tuning range is 4.7:1. For the design parameters in isolation circuit, the resistor R is chosen as 100 Ω according to (4.11) and (4.12), and the tuning range of C_2 is 0.2 pF to 2 pF. Based on the desired capacitance tuning ranges of C_1 and C_2, surface mount tuning varactors MA46H 202 (7-0.5 pF) are chosen for C_1, while C_2 is realized by an SMV 2202 (2.1-0.23 pF). Similar to the process in Chapter 3 Section 3.5.1, the calculated parameters are converted to distributed elements by using Sonnet simulation. The substrate used in Chapter 3 is employed in this design. **Fig. 4. 8** (a) shows the configuration of the design with bias circuits supplying voltages to the varactors. Proper gaps are reserved on the layout for soldering lumped elements. Optimized design parameters are listed in **Table 4.1**. Design layout file is imported to LPKF CircuitCAM for the fabrication process. The fabricated circuit is shown in **Fig. 4. 8**(b). The front transmission lines are bent in order to connect the varactors (MA46H-202) in parallel with them. Resistor R and a capacitor (SMV-2202) connecting in series are soldered to the isolation circuit. There are three DC bias circuits added to the divider. 20 pF capacitors and 10 kΩ resistors are used for DC blocking and RF blocking purposes in the bias circuits, respectively.

A DC power supply (BK PRECISION 9202) and a VNA (Agilent FieldFox N9917A) are employed in the measurement. The varactor diodes are operated under reverse bias conditions, so that there is no conduction. The capacitance C_1 is increased from 0.5 pF to 5.1 pF as the bias

voltage for the varactors in the main transmission lines is decreased from 20V to 0V. Conversely, the capacitance C_2 is decreased from 2.1 pF to 0.2 pF as the bias voltage on the isolation circuit varies from 0 to 20 V. Since the capacitance range of these varactors cannot cover the required tuning range of C_1 and C_2, two capacitors with fixed values of 0.01 pF and 0.2 pF are used in turn here to replace the varactors for part of the measurements. In the measurement, gradually tune the bias voltage on MA46H 202 to 1.7V, 6.1V, 11.4V and 20V to give S_{11} band located at 0.9 GHz, 1.7 GHz, 2.1 GHz, 2.8 GHz, respectively. Besides, 0.01 pF and 0.2 pF capacitors are used in turns to replace MA46H-202 to tune the centre frequency to 3.45 GHz and 4.2 GHz. At the same time, in order to make sure S_{22} and S_{23} move along with S_{11}, the bias voltage on SMV-2202 is set to be 0V, 0V, 0V, 2.2V, 7.8V and 20V, respectively. The measurement procedure is repeated several times, and the precision of the measurement is $\pm$0.1dB.

Fig. 4. 9 and **Fig. 4. 10** show the comparison of the simulated and measured *S*-parameter responses when the divider is tuned to the six sampled frequency bands accordingly. The measured S_{11} and S_{22} are below -20 dB at each band. The insertion loss varies between 3.2 dB and 4 dB, or 0.2 dB to 1 dB above the intrinsic loss of 3 dB. The measured isolation S_{23} is better than -20 dB at most of the sampled frequencies. The isolation is slightly worse at 4.2 GHz with a value of -17 dB, which is probably caused by fabrication errors and the accuracy of C_2. The measured tunable frequency range is 0.9 GHz to 4.2 GHz. The tuning range is 4.67:1 as the measured results indicate. Overall, the measured results are in very good agreement with the simulated ones. To show the advantages of the proposed PD, **Table 4.2** lists the performance comparison between this work and other works reported in recent years. As the table illustrated, the frequency tuning range (when S_{11}<-20 dB) for the proposed work is much wider than other relevant works. The measured in-band S_{11} (better than 25 dB) is better than all other works. The circuit is very compact as well for such a wide tuning range.

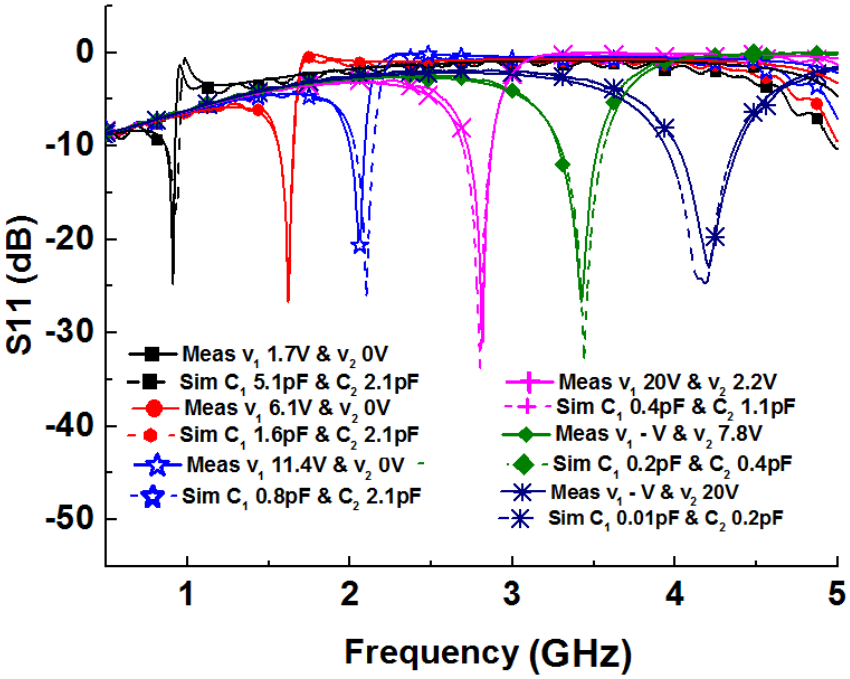

(a)

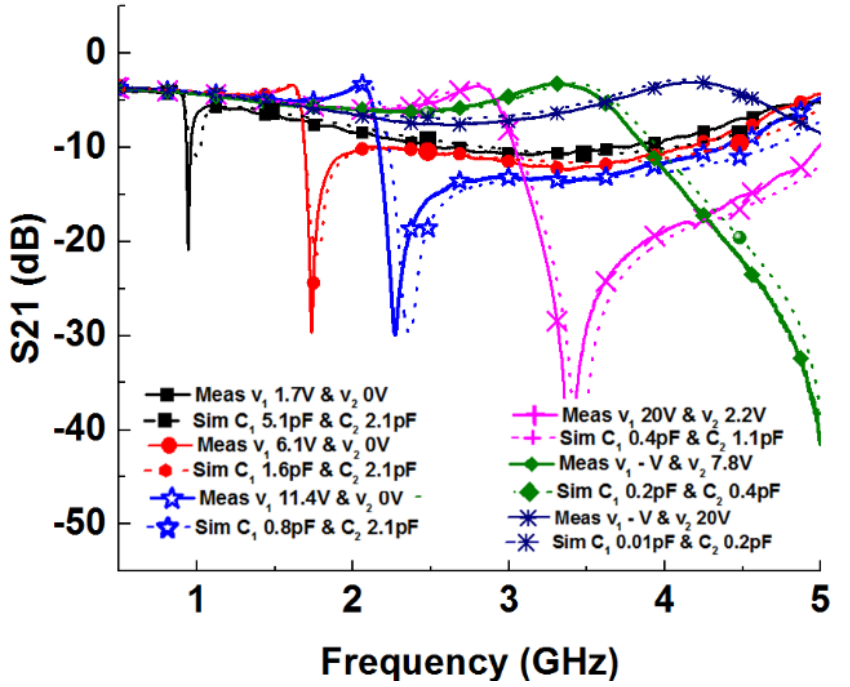

(b)

Fig. 4. 9 Comparison between simulations and measurements, (a) S_{11} and (b) S_{21}.

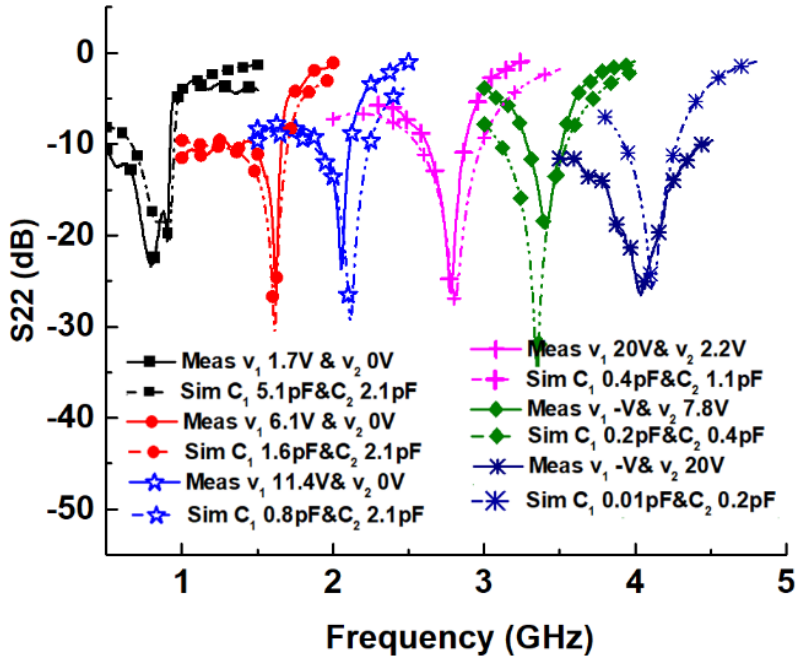

(a)

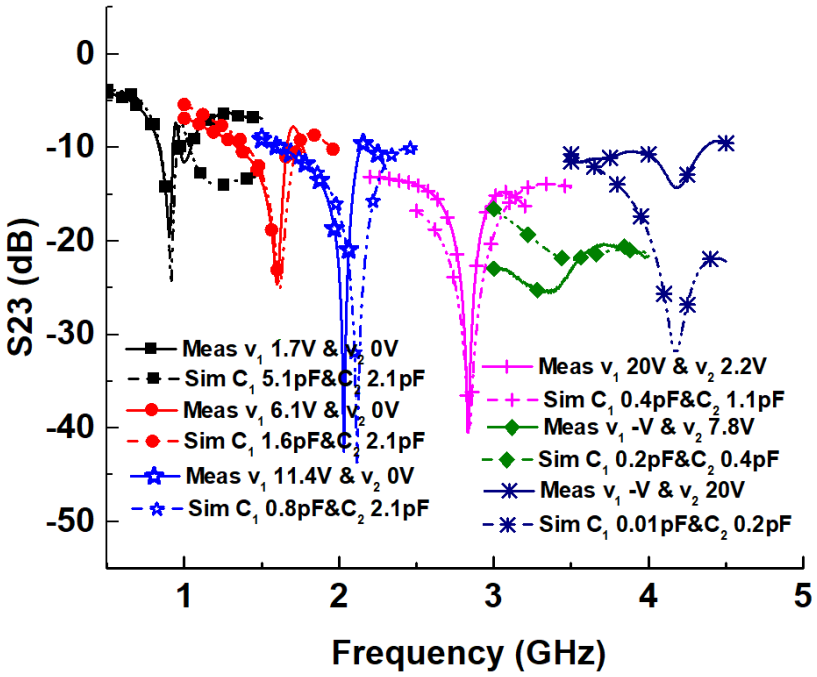

(b)

Fig. 4. 10 Comparison between simulations and measurements, (a) S_{22}, and (b) S_{23}.

Table 4. 2 COMPARISON TO OTHER WORKS.

Ref.	Tuning Range (GHz)	Return Loss (dB)	Insertion Loss (dB)
[10]	1.3-2.08 (1.6:1)	≥ 20	5.3-2.9
[11]	0.62-0.85 (1.37:1)	≥ 15	5.4-4.8
[13]	0.56-1.39 (2.48:1)	≥ 22	4.5
[14]	0.5-1.3 (2.6:1)	≥ 17	4.6-3.5
[15]	0.83-2.4 (2.9:1)	> 23	3.5-3.3
[16]	0.85-2.4 (2.82:1)	> 20	5.6-2.16
This work	**0.9-4.2 (4.67:1)**	**≥ 25**	**4-3.2**

4.5 Summary

A compact PD with a wide frequency tuning range has been designed and verified in this chapter. The proposed structure is based on a Horst-type PD, and a pair of varactors is added in parallel with the main transmission lines which introduces a controllable reflection minimum sensitive to the capacitance change. A single varactor diode is added in series to the isolation circuit to tune the operating bands of output return losses and isolation. The design equations have been derived to quantificate the changing center frequency with capacitances. A design guidance is provided to determine the parameters of the proposed PD. Impedances and the tuning range of the varactors should be carefully selected for achieving desired tuning bandwidth. The centre frequency tuning range is dramatically broadened by using the proposed method. To validate the proposed theory, a prototype with a frequency tuning range from 0.9 GHz to 4.2 GHz has been fabricated and measured. In the measurements, two sets of bias circuits are added to the design to alter the capacitance of the varactors. To the best of authors' knowledge, the tuning range is superior to all other works. The circuit has a relatively very compact size ($0.2\ \lambda_g \times 0.16\ \lambda_g$). The measured and simulated results have a perfect agreement with each other. Moreover, this method can also be applied to multi-way designs. The reason is that the operating band of the two-way PD exhibits a very good response but within a narrow bandwidth. When several two-way PDs are cascaded together, the impedance matching at the interconnecting points will be good as well, so that the overall circuit will obtain the same frequency tuning range as the two-way PD exhibits.

References

[1] X.-D. Wang, J.-P. Wang, G. Zhang, J.-S. Hong and W. Wu, "Dual-Wideband Filtering Power Divider With Good Isolation and High Selectivity," *IEEE Microwave and Wireless Components Lett.*, vol. 27, no. 12, pp. 1071-1073, 2017.

[2] D. Psychogiou, R. Gómez-García, A. C. Guyette, and D. Peroulis, "Reconfigurable single-/multi-band filtering power divider based on quasi-bandpass sections," *IEEE Microw. Wireless Compon. Lett.*, vol. 26, no. 3, pp. 684–686, Sep. 2016.

[3] Wu, Y., Liu, Y., Xue, Q., Li, S., and Yu, C.: 'Analytical design method of multi-way dual-band planar power dividers with arbitrary power division', *IEEE Trans. Microw. Theory Tech.*, 58, (12), pp. 3832–3841, 2010.

[4] Y.-F Pan, S.-Y Zheng, Y.-M. Pan, Y.-X. Li and Y.-L. Long, "A Frequency Tunable Quadrature Coupler with Wide Tuning Range of Center Frequency and Wide Operating Bandwidth," *IEEE Trans. Circuits Syst. II, Exp. Briefs*, vol. 65, no. 7, pp.864-868, 2018.

[5] T. Yang, and G. M. Rebriel, "Bandpass-to-Bandstop Reconfigurable Tunable Filters with Frequency and Bandwidth Controls," *IEEE Trans. Microw. Theory Techn.*, vol. 65, no. 7, pp. 2288-2297, 2017.

[6] Z. Wang, J. R. Kelly, P. S. Hall, A. L. Borja, and P. Gardner, "Reconfigurable parallel coupled band notch resonator with wide tuning range," *IEEE Trans. Ind. Electron.*, vol. 61, no. 11, pp. 6316–6326, Nov. 2014.

[7] Zhi-Han Chen and Qing-Xin Chu: 'Dual-band reconfigurable bandpass filter with independently controlled passbands and constant absolute bandwidths', *Microw. Wireless Compon. Lett.*, 2016, 26, (2),pp.92-94.

[8] L. Athukorala, D. Budimir, "Open-loop tunable resonators and filters with constant bandwidth," *Microwaves, Antennas & Propagation, IET*, vol.6, no.7, pp.800-806, May 16, 2012.

[9] H. Zhu, and A. M. Abbosh, "Tunable balanced bandpass filter with wide tuning range of center frequency and bandwidth using compact coupledline resonator," *IEEE Microw. Wireless Compon. Lett.*, vol. 26, no. 1, pp. 7--9, Jan. 2016.

[10] P.-L. Chi and T. Yang, "A 1.3–2.08 GHz Filtering Power Divider With bandwidth control and high in-band isolation," *IEEE Microw. Wireles Compon. Lett.*, vol. 26, no. 6, pp. 407-409, 2016.

[11] L. Gao, X. Y. Zhang, and Q. Xue, "Compact Tunable Filtering Power Divider With Constant Absolute Bandiwdth," *IEEE Trans. Microw. Theory Techn.*, vol. 63, no. 10, pp. 3505-3513, 2015.

[12] A.-L. Perrier, O. Exshaw, J.-M. Duchamp, and P. Ferrari, "A Semi-Lumped Miniaturized Spurious Less Frequency Tunable Three-port Divider\combiner with 20 dB Isolation Between Output Ports," in *IEEE MTT-S International Microwave Symposium Digest*, San Francisco, 2006.

[13] X. Shen, Y. Wu, S. Zhou, and Y. Liu, “A novel coupled-line tunable wikinson power divider with perfect port match and isolation in wide frequency tuning range,” *IEEE Trans. Compon., Packag. Manuf. Technol.* , vol. 6, no. 6, pp. 917-925, 2016.

[14] S. Lin, Y. Chen, P. Chiou and S. Chang, "Tunable Wilkinson power divider utilizing parallel-coupled-line-based phase shifters," *IEEE Microw Wirel Components Lett* 27(4), pp. 335–337, 2017.

[15] T. Zhang and W. Che, “A Compact Tunable Power Divider With Wide Tuning Frequency Range and Good Reconfigurable Responses,” *IEEE Trans. Circuits Syst. II, Exp. Briefs*, vol. 63, no. 11, pp. 1054-1058, 2016.

[16] T. Zhang, X. Wang and W. Che, “A Varactor Based Frequency-Tunable Power Divider With Unequal Power Dividing Ratio,” *Microwave and Wireless Components Letters, IEEE*, vol. 26, no. 8, pp. 589-591, 2016.

[17] A. Chen, Y. Zhuang, Y. Huang and J. Zhou, ‘A Horst-type Power Divider with Wide Frequency Tuning Range Using Varactors,’ *IEEE Access,* ISSN: 2169-3536， pp: 1-13, 2018.

[18] S. Horst, R. Bairavasubramanian, M. M. Tentzeris, and J. Papapolumerou, “Modified Wilkinson power dividers for millimeter wave applications,” *IEEE Trans. Microw, Theory Techn*., vol. 55, no. 11, pp. 2439-2446, 2007.

[19] X. Wang, I. Sakagami, N. Ito, and A. Mase, “Miniaturized Horst-type Wilkinson power divider with simple layout,” *Electron. Lett*., vol. 49, no. 6, pp. 384-395, 2013.

Chapter 5 Millimetre-Wave CPW PDs Using Spiral Resonators for Miniaturization.

5.1 Introduction

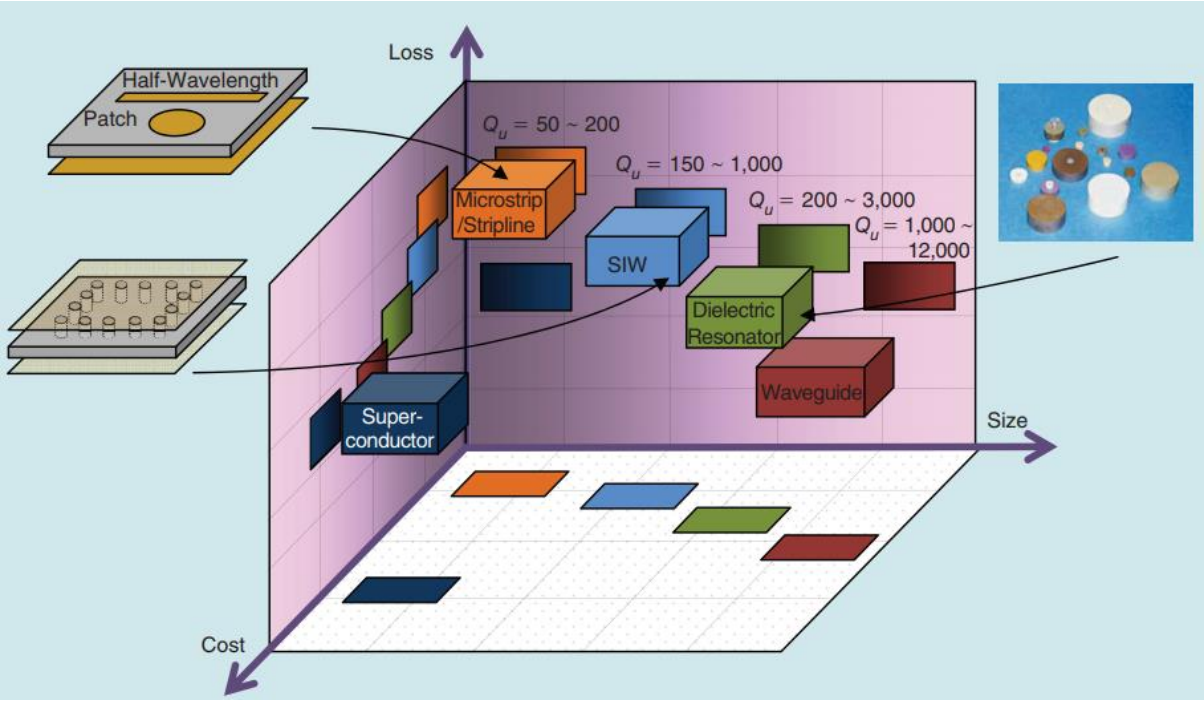

Fig. 5. 1 Relative loss, size, and cost of various RF resonators [1].

PD designs for mm-Wave applications require low loss, compact size, low cost and easy to be integrated into MMICs [1]. **Fig. 5. 1** compares these features between various technologies including superconductors, microstrip/striplines, substrate integrated waveguide (SIW), dielectric resonators and conventional metal waveguides [1]. For such high frequencies, the traditional waveguide is mostly used due to its high Q and low power loss. However, the traditional waveguide suffers from its massive size which is not preferred for circuit integration. To overcome this problem, SIW technique has been introduced. The substrate with via-holes can transmit signal just as in a waveguide with a much higher permittivity compared to the air used in the conventional waveguides, leading to a compact circuit size [2]. However, the substrate used in SIW operating in mm-Wave will be relatively lossy [1][3][4].

Superconducting components can be applied to achieve both a compact size and sufficient low loss. However, the cost is too high to perform mass production. Therefore, to make a trade-off among these features, coplanar PDs are proposed using coupled resonators.

The coplanar waveguide (CPW) was firstly proposed by Wen [5]. It consists of a metal strip and two adjacent ground planes printed on the dielectric substrate. The most significant advantage of the CPW is that only a single-layer metal process is required. As via-hole grounding can be omitted because the ground and metal strip are uniplanar so that the active or passive components in shunt configuration can be easily connected. On the other hand, the conducting material used in the CPW structure is still relatively lossy in mm-Wave [6]-[9]. Typically, a three-port component requires a T-junction to connect two output ports with the input to form a PD. These connections occupy larger sizes and produce more conducting loss especially for mm-wave applications. Moreover, the unwanted quasi-TEM mode will rise due to the intrinsic structure of CPW [3]. Air-bridges are needed to suppress the undesired mode by keeping the lateral ground planes at the same potential, which will indeed complicate the fabrication process and introduce more loss [4]. Many CPW-PD designs have been reported [10][11] recently. They used long CPW lines (quarter wavelength) that require more air-bridges to maintain the desired operating mode, resulting in large sizes and losses. To overcome the problems discussed above, [12]-[16] introduced CPW coupled resonators. [16] utilises three stepped resonators in the design to eliminate air-bridges. However, this type of resonators is not easy to be implemented at mm-Wave, and the topology is complicated to be used for multi-way PDs.

The spiral resonators have been adopted in mm-Wave filters designs which can be realised in the forms of CPWs [17] [18]. The spiral resonators can achieve a very compact circuit size by folding a quarter-wavelength CPW central strip into a spiral. Referring to the size comparison between the spiral resonator and open-loop resonator in [19], the spiral resonator only occupies 40% of the area of an open-loop at the same resonant frequency. The spiral resonators are not only compact but also have remarkable properties such as high Q, high power capability and insensitivity to the fabrication process [9]. Hence, the CPW coupled resonators are firstly adopted in mm-Wave PD designs. In this work, the conducting loss can be minimised by replacing the interconnecting lines with coupled resonators. G type spiral resonators are utilised

in this design for size miniaturisation. Moreover, the Q can also be improved which will be explained in detail in the following sections.

5.2 Analysis of the Coupled-Resonator PD

To design a low loss and compact size PD, three CPW spiral resonators are employed in the circuit. To transmit power from one input port to two output ports, an equivalent circuit of three coupled resonators is depicted in **Fig. 5. 2.**

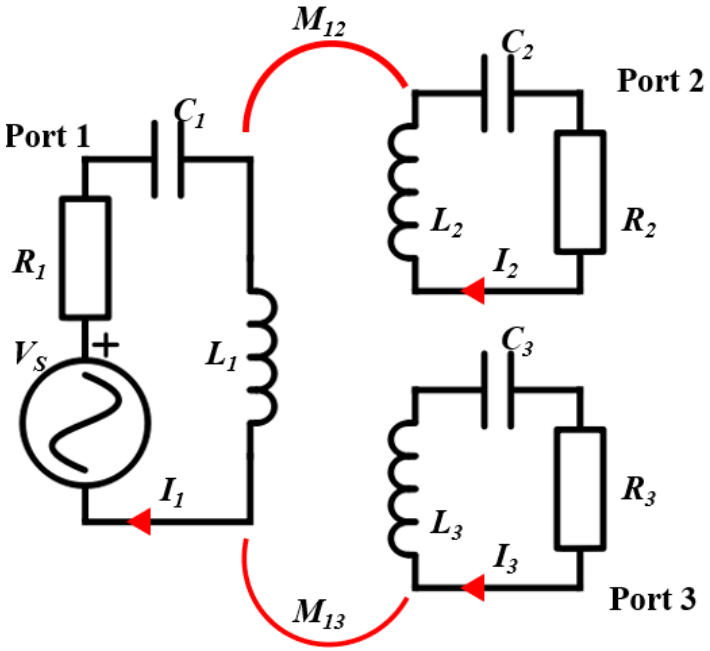

Fig. 5. 2 The equivalent circuit of a PD with three coupled resonators.

The inductance, capacitance and resistance of each resonator are denoted as L, C, and R in **Fig. 5. 2**, respectively. I represents the loop current in each resonator while V_s indicates the source voltage. M_{12} and M_{13} represent the mutual inductances between Resonator 1 and 2, and Resonator 1 and 3, respectively. By using the voltage law, the algebraic sum of the voltage drops around any closed loop circuit in a network is zero. Based on the Kirchhoff's Voltage Law (KVL), the voltages on the resonators can be expressed as:

$$\left(R_1 + j\omega L_1 + \frac{1}{j\omega C_1}\right) I_1 - j\omega M_{12} I_2 - j\omega M_{13} I_3 = V_S \tag{5.1}$$

$$-j\omega M_{12} I_1 + \left(R_2 + j\omega L_2 + \frac{1}{j\omega C_2}\right) I_2 - j\omega M_{23} I_3 = 0 \tag{5.2}$$

$$-j\omega M_{13} I_1 - j\omega M_{23} I_2 + \left(R_3 + j\omega L_3 + \frac{1}{j\omega C_3}\right) I_3 = 0 \tag{5.3}$$

It can be assumed that the coupling between the two outputs can be ignored as it is very weak compared to the main coupling from the input port, yielding $M_{23} = 0$.

The port termination of each port is usually the same at 50 Ω, therefore, that is, $R_1 = R_2 = R_3 = R = 50\ \Omega$. Then, when the system is operating at the resonant frequency ω_0, the current flow in each loop can be derived as:

$$I_1 = \frac{RV_S}{(R^2 + \omega_0^2 M_{12}^2 + \omega_0^2 M_{13}^2)} \tag{5.4}$$

$$I_n = \frac{j\omega M_{1n} V_S}{(R^2 + \omega_0^2 M_{12}^2 + \omega_0^2 M_{13}^2)}, (n = 2 or 3) \tag{5.5}$$

Now, the scattering parameters of the system can be evaluated as:

$$S_{11} = 1 - \frac{2RI_1}{V_S} = 1 - \frac{2R^2}{(R^2 + \omega_0^2 M_{12}^2 + \omega_0^2 M_{13}^2)} \tag{5.6}$$

$$S_{n1} = \frac{2RI_n}{V_S} = \frac{2\, j\omega M_{1n} R}{(R^2 + \omega_0^2 M_{12}^2 + \omega_0^2 M_{13}^2)}, (n = 2 or 3) \tag{5.7}$$

It can be found that the power splitting ratio of the output ports can be derived as:

$$S_{21} / S_{31} = M_{12} / M_{13} \tag{5.8}$$

On the other hand, to minimise the reflection coefficient to enable the maximum power to be injected to the system, S_{11} should be equal to zero, yielding:

$$\begin{aligned} 1-\frac{2R^2}{(R^2+\omega_0^2M_{12}^2+\omega_0^2M_{13}^2)}&=0 \\ R^2-\omega_0^2(M_{12}^2+M_{13}^2)&=0 \\ \sqrt{M_{12}^2+M_{13}^2}&=\frac{R}{\omega_0} \end{aligned} \tag{5.9}$$

Then, by combining the desired power splitting ratio derived in (5.8) (5.9), the desired mutual inductances to realise the PD can be obtained. The same method can be applied to design an *N*-way PD with desired power division ratio.

Coupling coefficient k_{ij} is usually employed to describe the relationship between the distances of resonators and the coupling strength, while mutual inductance M_{1n} cannot show intuitive relationship between distance and coupling strength. So introducing k_{1n} to equations can simplify the realisation of designs. M_{1n} and k_{1n} can be expressed as:

$$k_{1n}=\frac{M_{1n}}{\sqrt{L_1L_n}} \tag{5.10}$$

And introducing external quality factor Q_e into the equation,

$$\frac{1}{Q_{en}}=\frac{R_n}{\omega_0L_n} \tag{5.11}$$

where $\omega_0 = 1/\sqrt{LC}$.

So the power dividing ratio of the output ports can be concluded as

$$S_{21}/S_{31}=\frac{k_{12}}{k_{13}}\cdot\sqrt{\frac{Q_{e2}}{Q_{e3}}} \tag{5.12}$$

As the Eq (5.12) indicates, the power division are not only relates to the coupling coefficients, but also affected by the ratio of their external quality factors.

5.3 CPW PD with Spiral Resonators

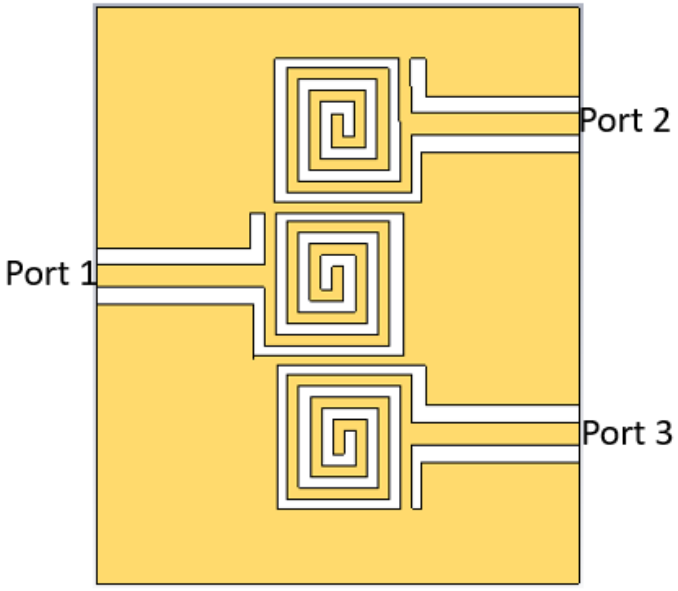

Fig. 5. 3 The configuration of the proposed CPW PD with three resonators.

To reduce the circuit footprint, spiral resonators are employed for significant size reduction compared to conventional ring resonators. To verify the method, a CPW-PD with three spiral resonators is designed with a centre frequency of 48.5 GHz. The configuration of the design is shown in **Fig. 5. 3**. The spiral line winds clockwise with one end connected to the ground. The length of the resonator is about $\lambda/4$. The width W and gap S of the spiral line are both chosen to be 10 μm while the distance between two adjacent resonators is denoted as d. All the resonators are directly connected with the input 50 Ω CPW line where S_{port} is 15μm and W_{port} is 20μm. Due to the winding shape of the spiral resonator, if two resonators are coupled to the common resonator at two sides, these three resonators cannot be centrosymmetric. As a result, the common and upper resonators are wound in one direction while the lower one in the opposite direction to the common resonator winding.

5.3.1 Resonant Frequency

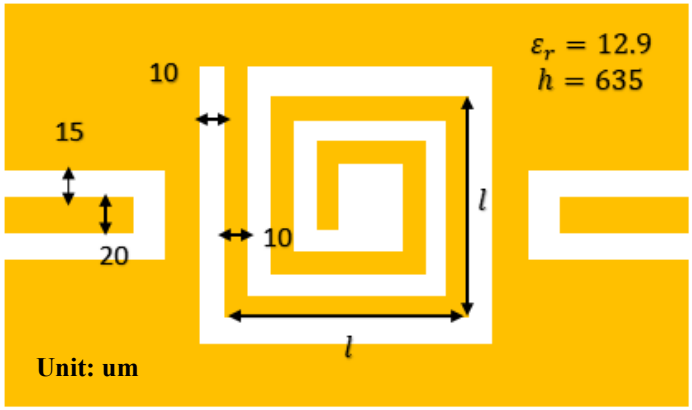

(a)

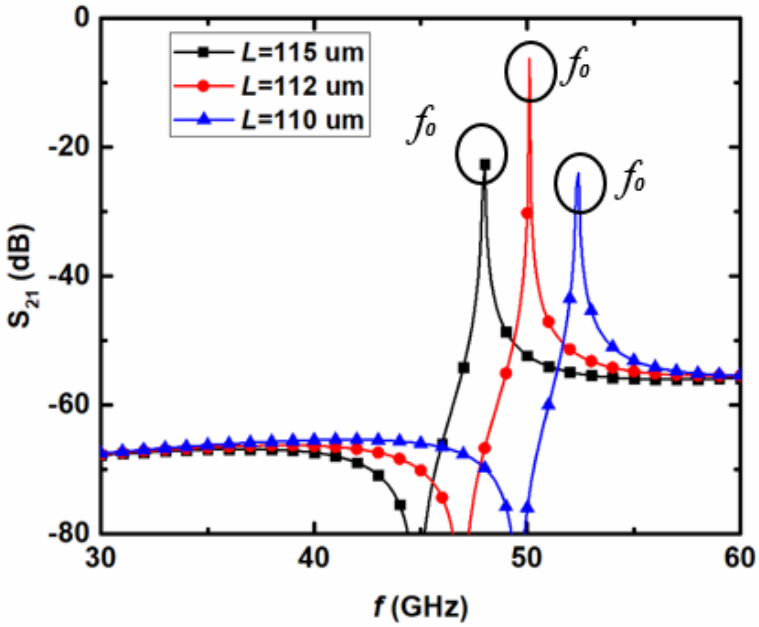

(b)

Fig. 5. 4 (a) The configuration of a quarter-wavelength spiral resonator, and (b) the relationship between resonance frequencies and side-length *L*.

To examine the resonant frequency f_0, a pair of open CPW feed-lines are placed at both sides of the resonator with some distance. The side-line length of the spiral resonator l is chosen to be 110 µm, 112 µm, and 115µm, and the overall length of the spiral line is 596 µm, 614 µm and 656 µm, respectively. **Fig. 5. 4**(a) shows the configuration of a single spiral resonator for

computation and **Fig. 5. 4**(b) depicts the variation of resonance frequency f with side-length l of the spiral. In obtaining the relationship given in **Fig. 5. 4**(b), the physical dimensions in **Fig. 5. 4**(a) are applied. The curve illustrates that the resonant frequency in general increases as the length of the spiral line decreases. In this chapter, a PD with a centre frequency f_0 equals to 48.5 GHz is designed. As a result, l is chosen to be 115 μm to conduct the following designs.

5.3.2 Coupling Coefficient *k*

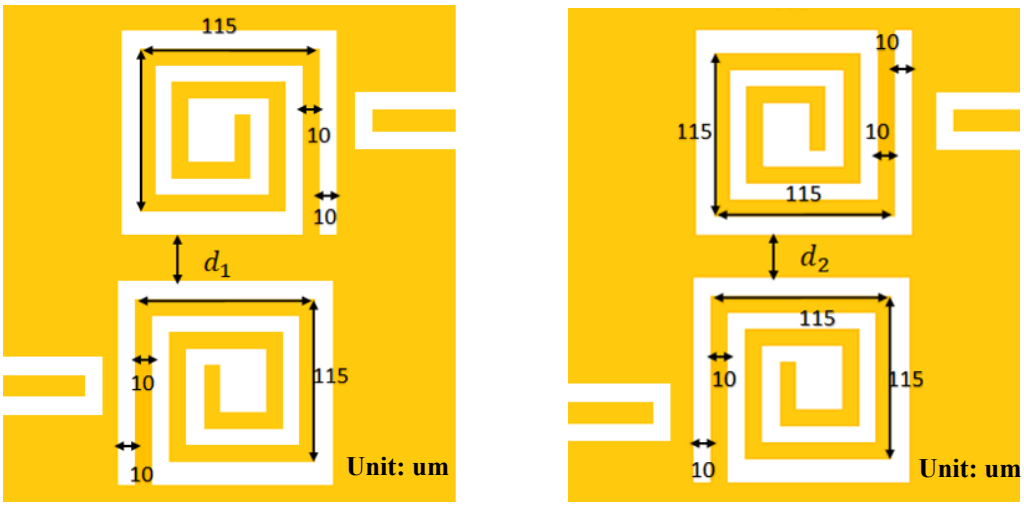

(a) (b)

Fig. 5. 5 (a) Face-to-back oriented, and (b) back-to-back reversely oriented resonators.

Fig. 5. 5 illustrates two types of coupled spiral resonators, one is face-to-back orientation and the other in back-to-back direction. The distances between every two resonators are denoted as d_1 and d_2 respectively. Simulation of the coupling can be carried out by placing a pair of feed lines to the two resonators in the opposite direction. With the coupling, the resonant frequency will be split into two, frequencies f_1 and f_2 as shown in **Fig. 5. 6**(a)-(b). The inter-resonator coupling coefficient can be calculated by

$$k = \frac{{f_2}^2 - {f_1}^2}{{f_2}^2 + {f_1}^2} \tag{5.13}$$

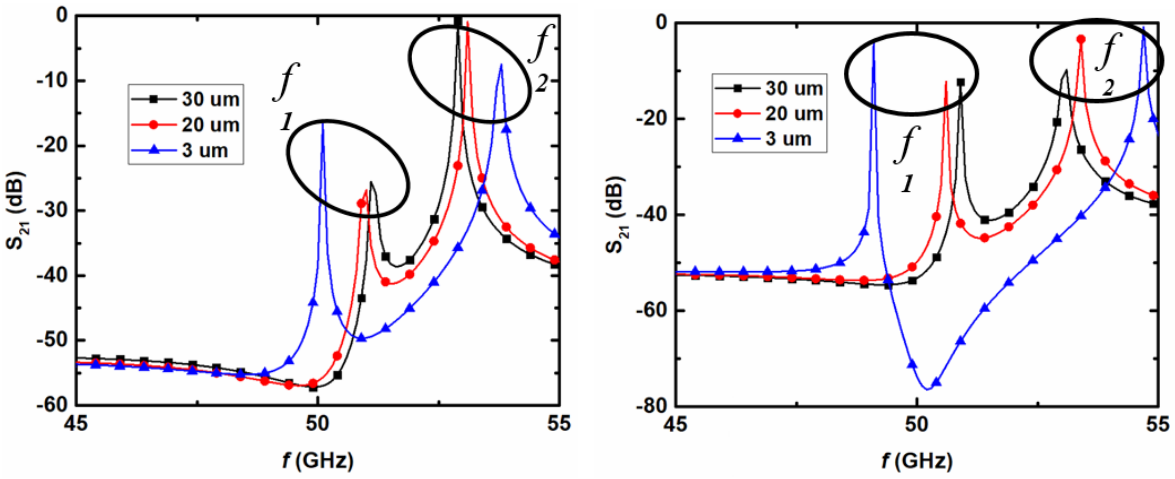

(a) (b)

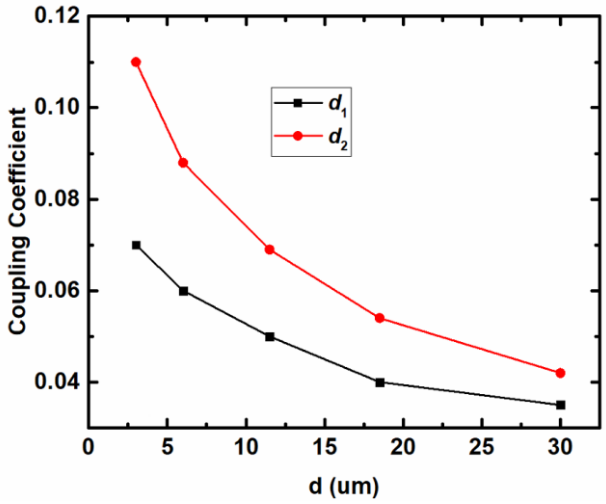

(c)

Fig. 5. 6 Resonant mode splitting phenomena of (a) face-to-back oriented and (b) back-to-back reversely oriented. (c) Coupling coefficient *k* versus the distance d between resonators.

Generally, with the increase of distance *d*, the split resonance frequencies f_1 and f_2 come closer, which means the coupling is weaker. The coupling coefficient *k* is computed, and the variation with different distance *d* is shown in **Fig. 5. 6**(c).

5.3.3 External Coupling Q_e

The general behaviour of these coupled resonators is affected by parameters, including the position and offset of the feeding lines, the gaps between spiral line and the ground and the height of the air gap. To achieve optimal performance, a parametric study on realizing external Q_e is performed in this section. For the tapped-line coupling, a 50 Ω CPW line is directly tapped onto the input and output resonators. L_{feed} denotes the distance between the point where the spiral line is connected to the ground and the CPW feed-point. The external single loaded quality factor can be extracted from simulation by using:

$$Q_e = \frac{\omega_0}{\Delta\omega_{\pm 90^\circ}} \tag{5.14}$$

Where $\omega_0 = 1/\sqrt{LC}$ is the resonant frequency, and $\Delta\omega_{\pm 90^\circ}$ represents the absolute bandwidth between the $\pm 90^\circ$ points which should be determined from the frequency at which the phase shifts $\pm 90^\circ$ with respect to the absolute phase at ω_0.

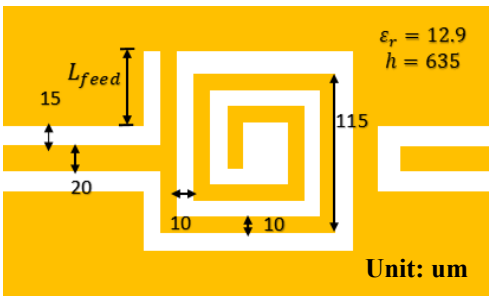

(a)

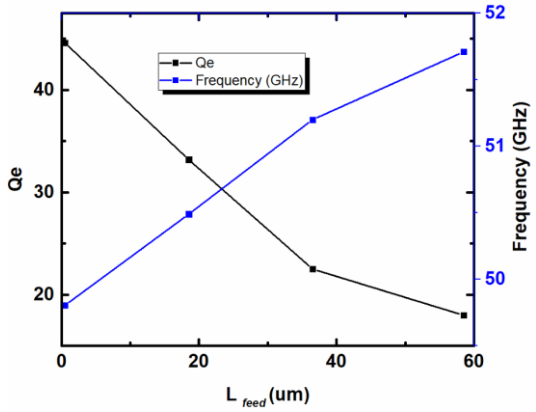

(b)

Fig. 5. 7 (a) Feeding structure of the PD, and (b) relationship between external Q_e and centre frequency f_0 with the off-set L_{feed} in (a).

Fig. 5. 7 (b) illustrates that the loaded quality factor is decreasing with the distance between the spiral-line end to the feed line increases. The Q_e achieves the maximum value when the feed-line is directly connected to the spiral line end. This is because the smaller the L_{feed} is, the closer is the tapped line to a virtual grounding of the resonator, which results in a weaker coupling, in other words, a larger external Q_e.

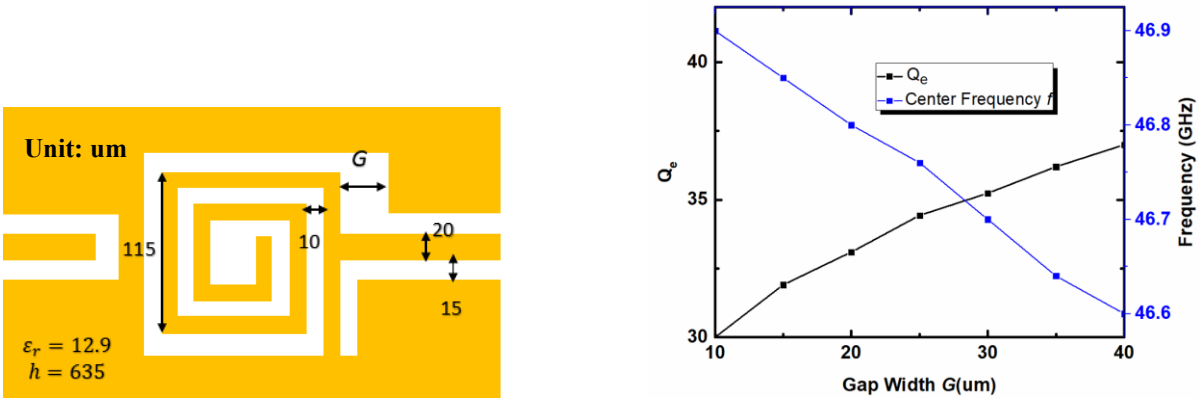

(a) (b)

Fig. 5. 8 (a) Feeding structure of the resonator, and (b) variation of Q_e and centre frequency f_0 with the gap width in (a).

Another way to increase the external coupling is to change the gap width *G* between the spiral and the ground on the feeding side. As is shown in **Fig. 5. 8**(b), when the gap width *G* is extended, the external coupling is enhanced significantly. However, extending the gap width *G* will also result in a centre frequency shifting down. To increase the external coupling without changing the centre frequency, the inner spiral line can be shorted a little bit to compensate. To get higher or lower values for the external quality factor Q_e is a matter of choosing the proper side for feeding the resonator.

5.4 Configurations and Designs

5.4.1 Proposed PDs

Fig. 5. 9(a) shows the structure of the proposed CPW two-way PD. The feedings at all three ports have an offset instead of feeding in the middle of the first spiral line to enhance external coupling. The signal is passing through the common resonator and coupled to upper and lower resonators with the same amount of the coupling. That is, the coupling coefficients k_{12} and k_{13} are the same. When the distance between the lower resonator and the common resonator

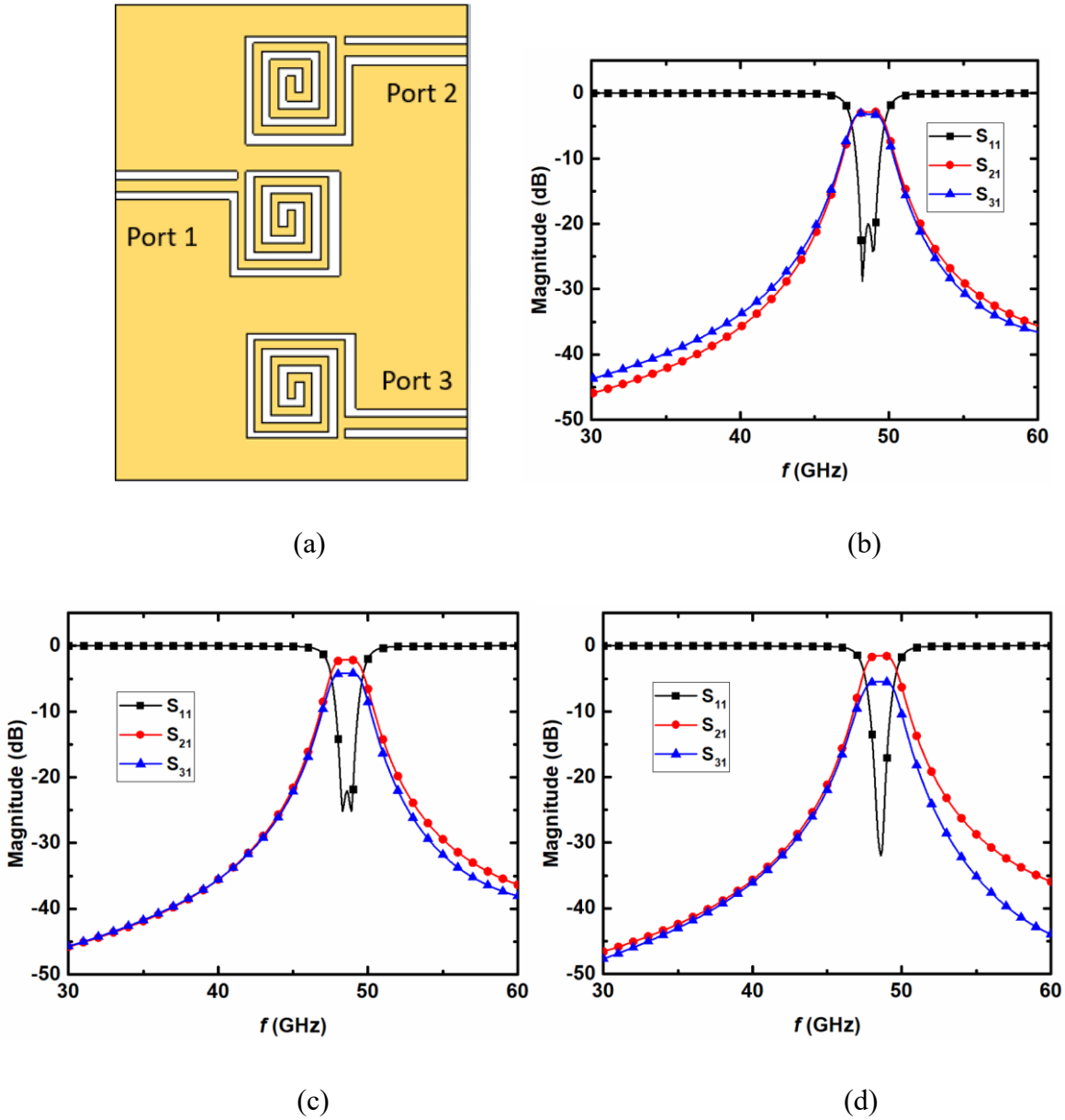

Fig. 5. 9 (a) Configuration of the optimized three-resonator PD with a 1:4 power division ratio, (b) 1:1 power division, (c) 1:2 power division and (d) 1:4 power division.

increases, the coupling strength between them will decrease, less energy will be coupled to the lower coupling path (from Port 1 to Port 3) and vice versa. It is the same for Port 1 and Port 2. For equal splitting, the mutual coupling coefficients be $k_{12} = k_{13} = 0.026$, and $Q_{e2} = Q_{e3} = 38.43$ to achieve a 3-dB bandwidth of 2.2 GHz at a centre frequency of 48.5 GHz. Then the corresponding physical distance between coupled resonators can be read from **Fig. 5. 9**(c). Also, this coupling structure is required to have a coupling coefficient ratio of k_{12}/k_{13}= 1:2 and 1:4 according to (5.8) for unequal power splitting.

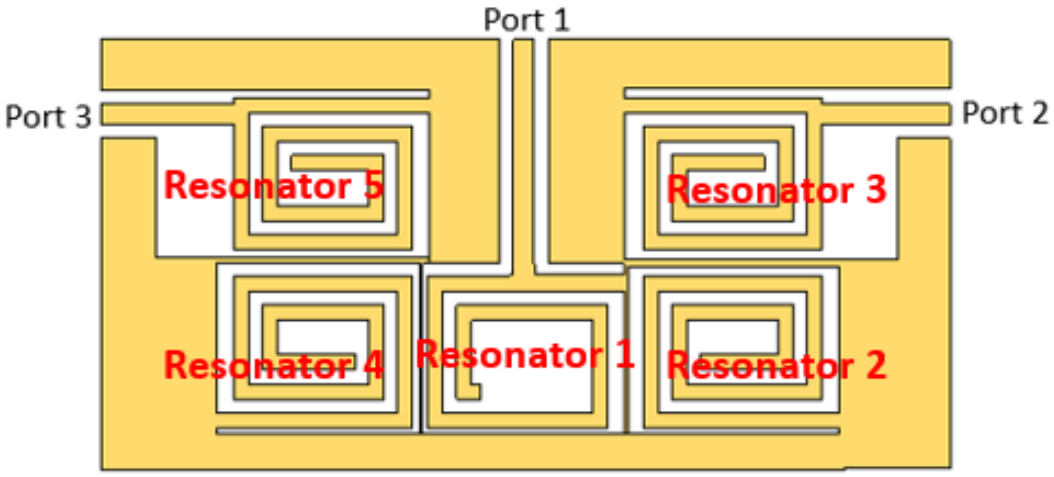

(a)

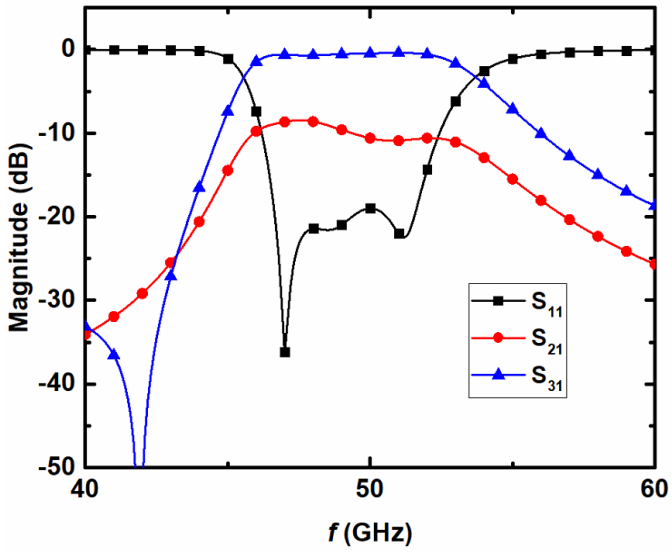

(b)

Fig. 5. 10 (a) Configuration of the CPW PD with five resonators, and (b) its simulated performance.

A PD with five asynchronous spiral resonators is shown in **Fig. 5. 10**(a). More spiral resonators are used to obtain a sharp-selectivity bandpass response compared to the third-order PD for the same Q_e. However, compared to the three-resonator PD, the power division ratio is more difficult to control due to the introduction of more resonators. These resonators are not allocated in one axis for the purpose of circuit miniaturization. The coupling path requires resonators with different orientations which would severely change the coupling conditions

between resonators because of the asymmetry of the spiral structure. As **Fig. 5. 10**(b) indicates, the bandwidth is around 1.13:1, and the coupling between Resonator 1 and Resonator 3 is stronger than the other that of Resonator 1 and Resonator 2 which results in a power division around 1:8.

5.4.2 Splitting Frequencies (diplexer)

Similar to a PD, a diplexer is also a three-port network, but assign disparate frequency bands at the same time. In this section, a five-resonator diplexer is designed by using resonators of different sizes and controlling the coupling strengths between them.

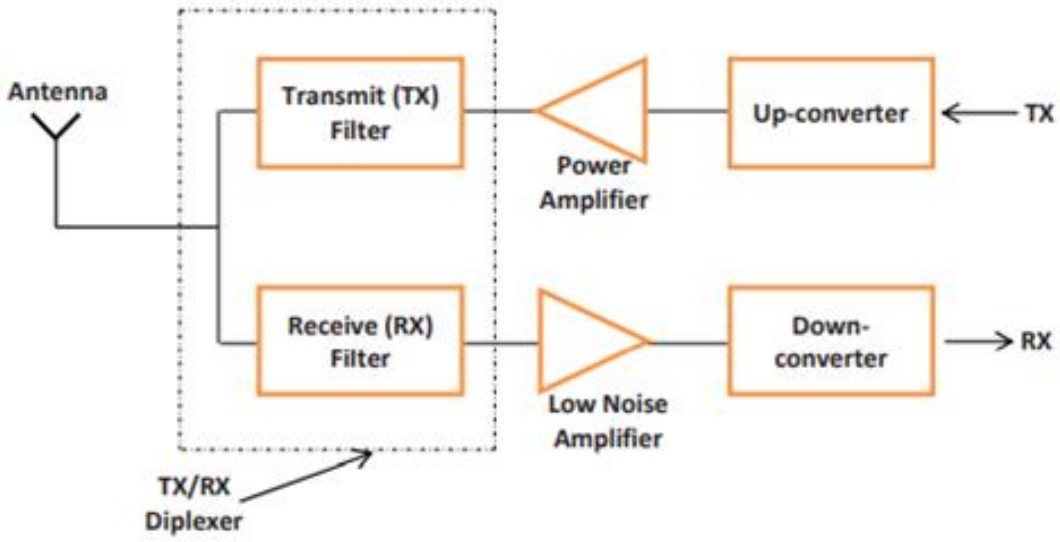

Fig. 5. 11 RF front end of a cellular base station [20].

A diplexer is commonly used in satellite communication systems to combine both the Tx (Transmit) and the Rx (Receive) antennas on spacecraft. It is frequently used in the RF front end of cellular radio base stations to separate Tx and the Rx channels as shown in **Fig. 5. 11**. The response of a diplexer contains two individual frequency bands, the lower passband and the higher passband. Conventionally, diplexers can be formed by connecting two separately designed filters via an external energy distribution device, such as a T-junction [20][21], a Y-junction [22], a circulator [23] or a common resonator [24][25]. The external junctions utilised in the conventional approaches for diplexer design resulte in more complex and larger size devices. Also, the connecting device does not contribute to the resultant diplexer but increases circuit size. To overcome these drawbacks, referring to designs [16][24][25], the work in this

section eliminates the external junctions and replacing it with a common resonator to distribute the input signal.

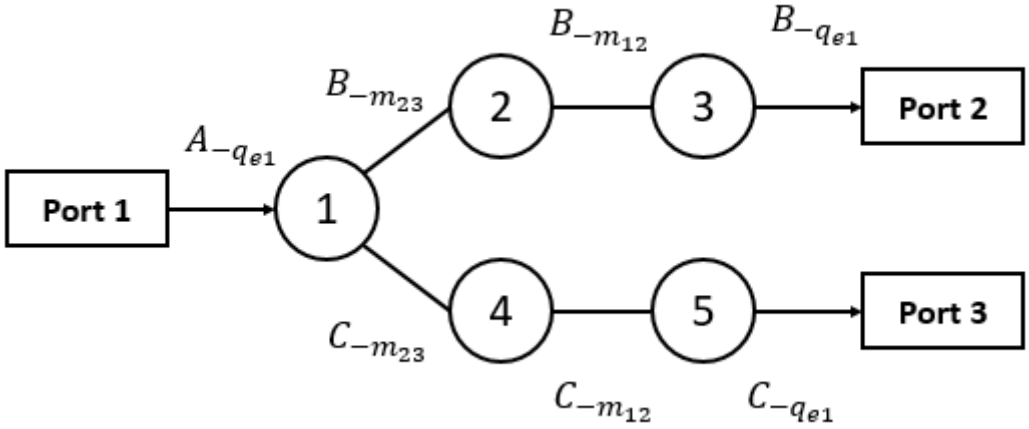

Fig. 5. 12 The topology of the proposed resonator-based diplexer.

Fig. 5. 12 shows the topology of the proposed 5-resonator diplexer with each circle represents a resonator and the interconnecting lines represent the coupling between them. The diplexer can be divided into two parts. The leading part is directly connected to the input which is called the stem. The other part is the two branches, one including Resonator 2 and 3 and the other formed of Resonator 4 and 5. Resonator 2 and 4 are coupled to the common Resonator 1. The common resonator or Resonators 1 has dual-resonant response to attenuate signals outside of the lower and higher passbands [26]. The two branches (B and C) work like two individual single band bandpass filters. Each branch occupies one of the two passbands of the dual-band filter so that the input signal passing through the common resonator will be guided to one of the branches, but rejected by the other branch. The general response of the device is given in as well as the lower and higher frequency bands for the two bandpass filters. f_c denotes the centre frequency of the whole circuit. As shown in **Fig. 5. 13**, the passbands $|f_2 - f_1|$ and $|f_4 - f_3|$ are not only the responses of the two branches, respectively, but also the passbands for the dual-band filter. Let us define A, B, and C as the common structure, and two passband filters, respectively. $A_{-q_{e1}}$, $B_{-q_{e1}}$ and $C_{-q_{e1}}$ in **Fig. 5. 12** represent the external coupling between the ports to the terminal resonators for the filters. $B_{-m_{12}}$ and $B_{-m_{23}}$, and $C_{-m_{12}}$ and $C_{-m_{23}}$ represent the internal coupling for the bandpass filters which can be directly employed as the internal coupling of the diplexer.

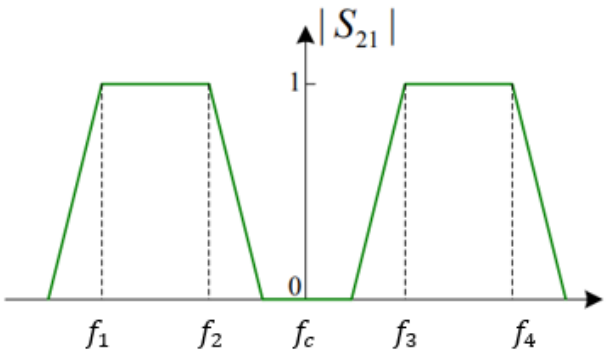

(a)

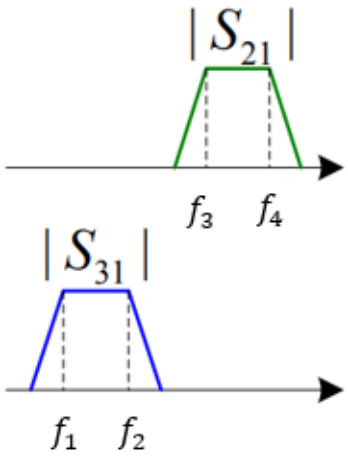

(b)

Fig. 5. 13 Theoretical response of (a) the dual-band bandpass filter, and (b) the bandpass filters of lower and higher frequency bands, respectively [22].

Normally, the coupling between the common resonators is strong, as well as the coupling between Resonator 2 and 3, and Resonator 4 and 5. On the contrary, the coupling between the branches and the common resonator, for example, Resonator 1 and 2 is weak. Moreover, the common resonator can always be replaced by any networks that have dual-band responses.

For a diplexer with asynchronously frequency bands, the sizes of the resonators on the two branches (1-2-3 and 1-4-5) are different, so that the self-coupling $m_{i,i}$ is introduced here. The self-coupling $m_{i,i}$ is used to quantify the difference between the resonant frequency f_i of Resonator *i* and the canter frequency f_c of the whole circuit. When resonator *i* is synchronously

tuned, which normally means the size of the resonators are the same, the normalized self-coupling $m_{i,i}$ equals to zero, while in asynchronously tuning, $m_{i,i}$ is an non-zero term. According to the coupling analysis in [26], the relationship between the normalized self-coupling $m_{i,i}$ and the resonant frequency f_i can be derived as

$$f_i = f_c \cdot \left[\frac{FBW \cdot m_{i,i}}{2} + \sqrt{\left(\frac{FBW \cdot m_{i,i}}{2} \right)^2 + 1} \right] \tag{5.15}$$

And the normalized self-coupling $m_{i,i}$ of resonator *i* equals to that of the higher or lower band pass filter.

$$m_{i,i} = 1 - \frac{BW_{\text{higher / lower band}}}{f_c \cdot FBW} \tag{5.16}$$

According to the specifications and the coupling matrix synthesis in [9], the normalized coupling matrix of the diplexer is $\{m_{12}, m_{23}, m_{14}, m_{45}, m_{11}, m_{22}, m_{33}, m_{44}, m_{55}, Q_{e1}, Q_{e2}, Q_{e3}\}$ = {0.45, 0.34, 0.45, 0.34, 0, 0.7, 0.74,-0.7,-0.74, 1.34, 2.2, 2.2}.

The normalized coupling matrix is transformed to the desired frequency band with a centre frequency $f_c = 50$ GHz.

The configuration of the proposed diplexer is shown in **Fig. 5. 14**(a), and different sizes of resonators are chosen to implement the design. To distribute the input signal to two frequency bands, the signal from the common resonator to the output resonator must pass through one output at a particular frequency band while there is little signal passing through to the other output. For the lower frequency band, the common resonator and the two resonators to Port 2 realize a passband at lower frequencies while the common resonator and the two resonators to Port 3 realize another passband at higher frequencies. The isolation between Port 2 and 3 should be high to avoid interference. Since the two coupling paths contribute to two distinct frequency bands, the isolation is typically good for coupling-based diplexers. The simulation shows that the diplexer has two frequency bands at 47.5GHz and 52 GHz. This design shows a narrow passband and only one reflection minimum is realized at each frequency band. To obtain better filtering performances with more in-band poles, more resonators can be used.

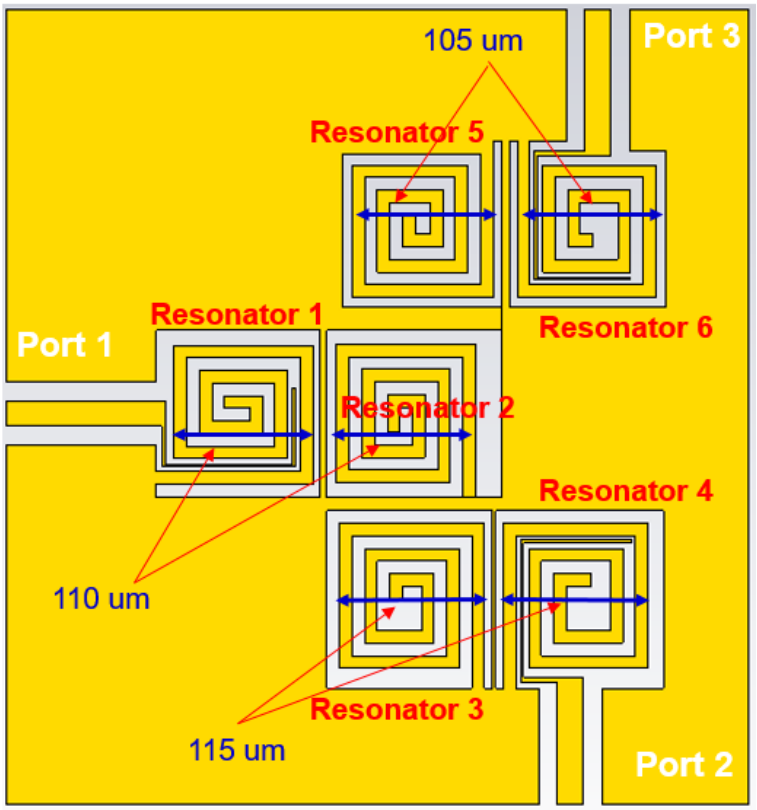

(a)

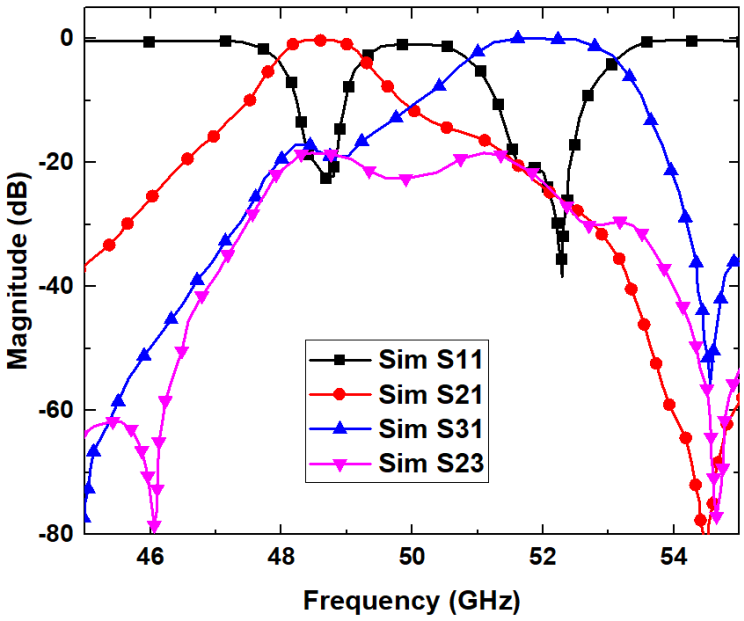

(b)

Fig. 5. 14 (a) Proposed five-resonator diplexer, and (b) its performances.

5.5 Fabrication Process and Measurement

Due to the limitation of facilities, the minimum width or gap of metal is 0.1 mm if using LPKF ProtoMat S62. To prove the design concept, the designs in this Chapter have been scaled down from 50 GHz to 2 GHz as shown in **Fig. 5. 15** for experimental validation. A equal splitting PD is designed in Sonnet on a Rogers RT6010LM substrate with $\varepsilon_r = 10.2$, and a thickness of 1.27 mm. The smallest width of the gap/strip is 0.2 mm, which is the smallest fabrication dimension of LPKF ProtoMat S62. Three 2.92mm edge launch connectors are clapped onto the three ports tightly. The edges of signal lines are wore off finely to prevent short-circuit to connectors. The circuit is measured by using a VNA (Agilent FieldFox N9917A) with a frequency range up to 18 GHz. A 50 Ω male load is always attached to the spare port that is not being measured. The simulated and measured results are imported to Origins for data plotting as shown in **Fig. 5. 16**. The measured S_{11} is better than 20 dB. S_{21} is about -4 dB, which means there is 1 dB loss caused by fabrication error and substrate. It can be observed from the comparison that the measured *S*-parameters are in good agreement with the simulation.

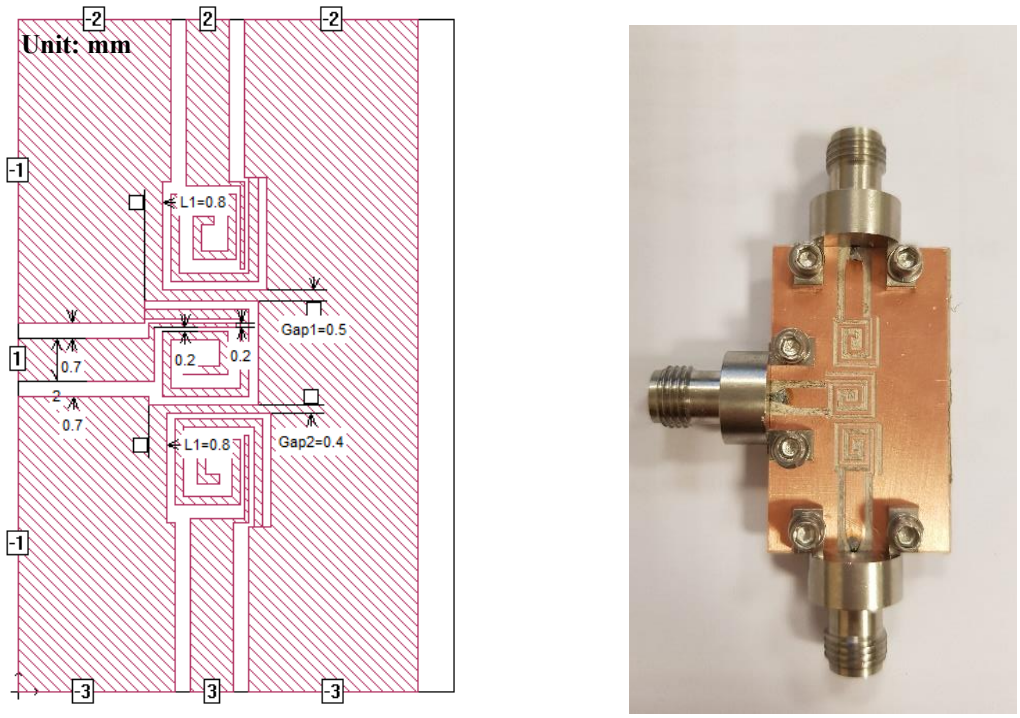

(a) (b)

Fig. 5. 15 (a) Circuit layout of a 2 GHz PD, and (b) the fabricated circuit.

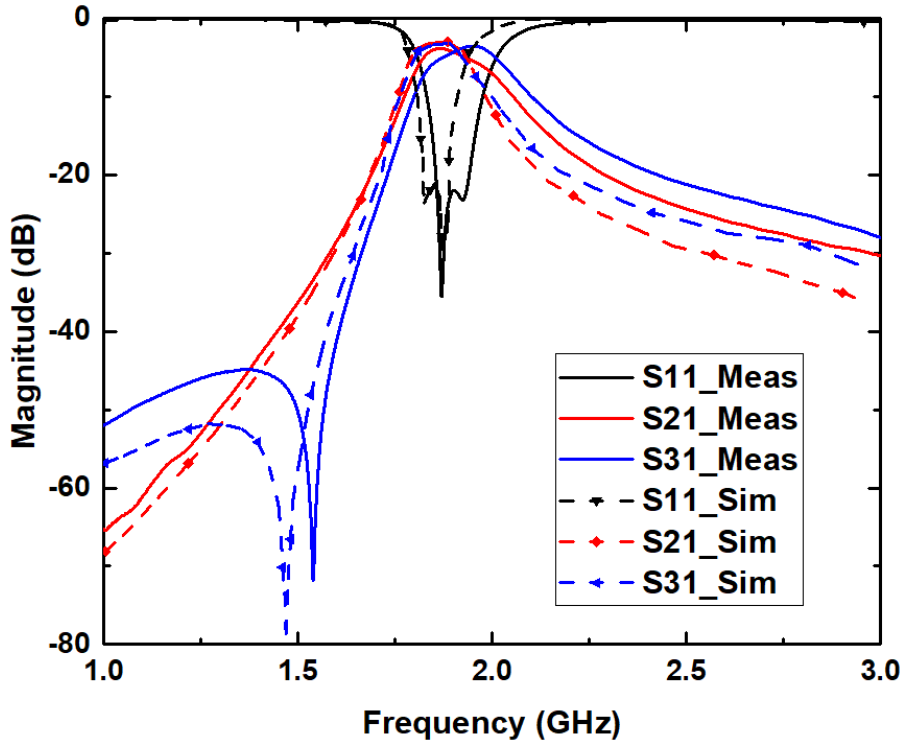

Fig. 5. 16 Comparison between the simulated and measured results of the 2 GHz PD.

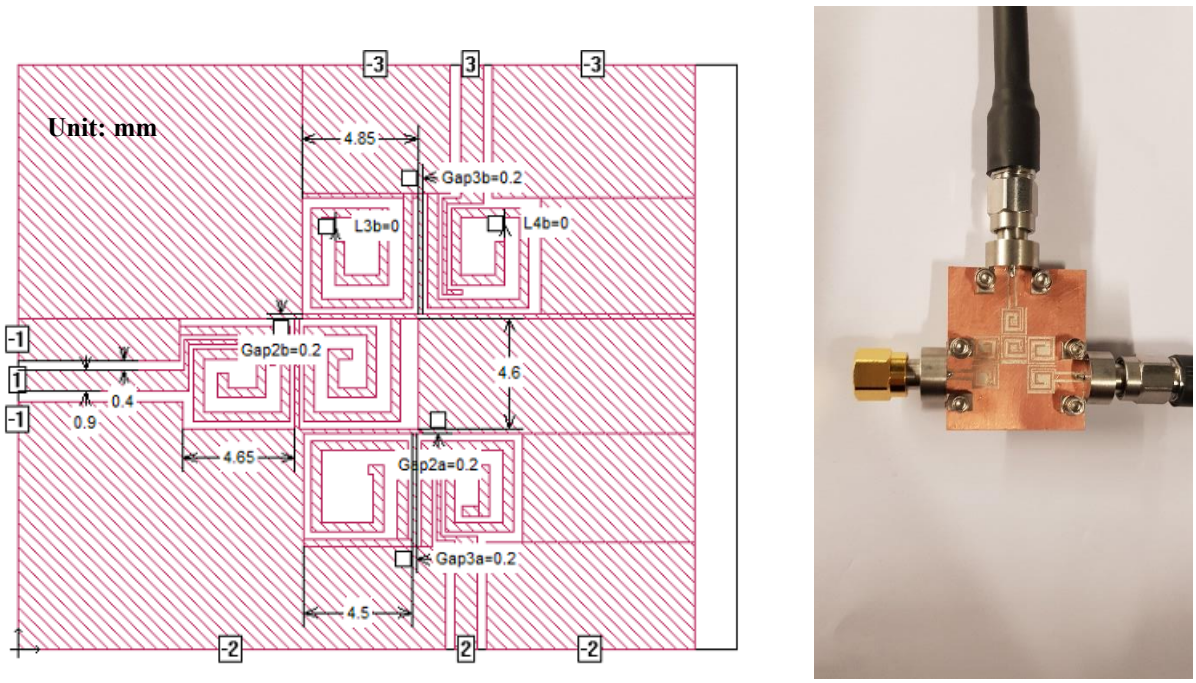

(a) (b)

Fig. 5. 17 (a) Circuit layout of a 2 GHz diplexer, and (b) the fabricated circuit.

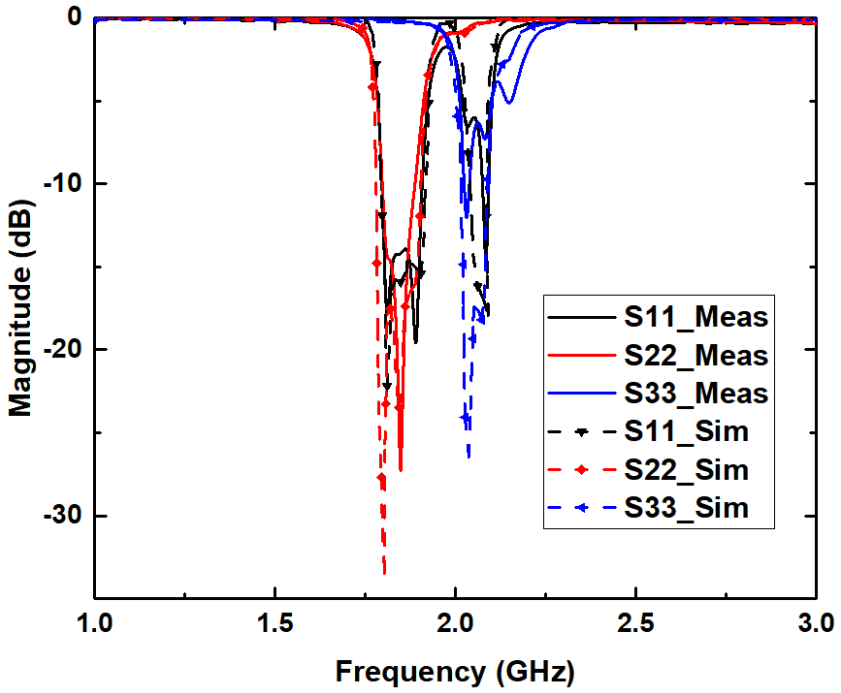

(a)

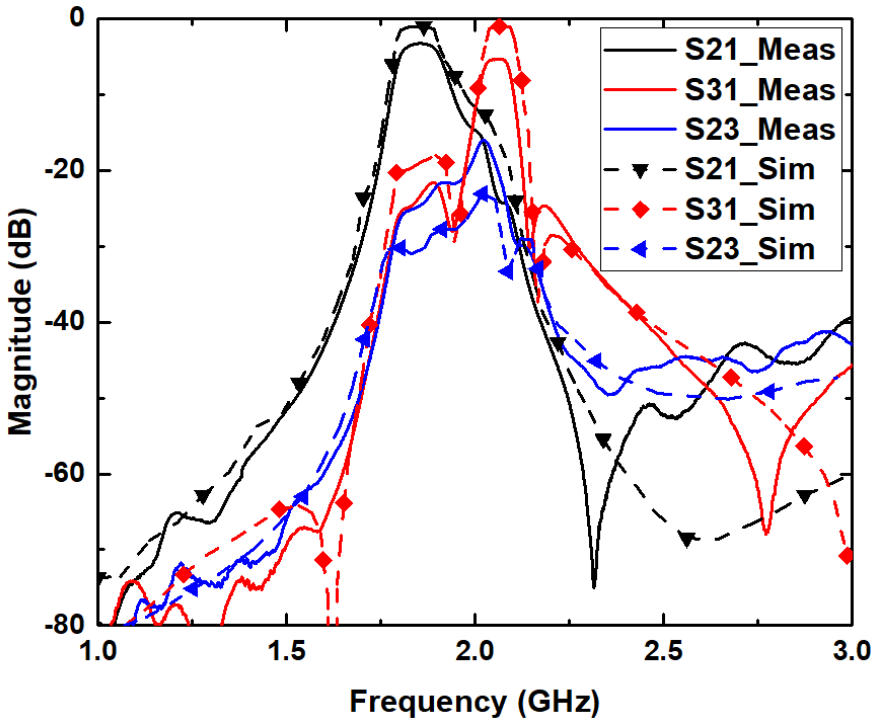

(b)

Fig. 5. 18 Comparison between the simulated and measured (a) S_{11}, S_{22} and S_{33}, and (b) S_{21}, S_{31} and S_{23} of the 2 GHz Diplexer.

A 2 GHz diplexer has been fabricated and measured in the same way. The circuit layout and the fabricated circuit are shown in **Fig. 5. 17**. The simulated and measured results are plotted using Origins as shown in **Fig. 5. 18**. The measured return loss S_{11} for lower frequency band is better than 14 dB. However, the return loss for higher frequency band is less than 7 dB which is caused by the fabrication precision ($\pm$0.1 mm in this case) of the gap between the resonators for higher frequency band. The fabrication precision also contributes to a relatively high insertion loss in measurement. In all, the measurement traces agree with simulations. The measured results show the potential of the proposed method to be applied for mm-Wave PD and diplexer designs to avoid using T- or Y- junctions and air-bridges.

5.6 Summary

In this chapter, two PDs and a diplexer have been designed by using coupled resonators. The idea of filter designs has been employed which enables the proposed circuits to have filtering responses. The bandwidth can be tuned by controlling the coupling coefficients between resonators. The rectangular G-type spiral resonators have been used to implement all the designs, allowing significant size miniaturisation. Moreover, a common spiral resonator replaces the T-junction between two branches to avoid using air-bridges. It should be noted that with the same distance between resonators, different orientations of two adjacent resonators will result in different coupling coefficients which in turns produces distinct power division ratios (1:1, 1:2, 1:4 and 1:8). The PDs occupy very compact sizes. The one with three resonators has a size of $0.13\,\lambda_g \times 0.1\,\lambda_g$ while the size of the PD with five resonators is roughly $0.2\,\lambda_g \times 0.06\,\lambda_g$. One equal splitting PD operating at 2 GHz has been fabrication and measured, the measured S_{11} is better than 20 dB which has verified the method well.

The diplexer design employs a common resonator to connect two branches to avoid using extra air-bridges and also eliminate unnecessary loss caused by T- or Y-junctions. The simulation shows two narrow frequency bands are located at 47.5 GHz and 52 GHz with S_{11} better than 20 dB. The isolation of these two branches is lower than 20 dB. The circuit size of the diplexer excluding feed lines is $0.07\,\lambda_g \times 0.26\,\lambda_g$ which is comparably compact compared to the designs with connecting junctions. A diplexer with 2 GHz centre frequency has also been

fabricated and tested. The measured results show that the diplexer is more sensitive to the gap between resonators, extra loss is caused by the fabrication precision.

References

[1] Chen, X.P., and Wu, K. "Substrate integrated waveguide filter: basic design rules and fundamental structure features," *IEEE Microw. Mag*., 2014, 15, (5), pp. 108–116.

[2] Zhang, Q.-L., Yin, W.-Y., He, S., and Wu, L.-S.: 'Compact substrate integrated waveguide (SIW) bandpass filter with complementary split-ring resonators (CSRRs)', *IEEE Microw. Wirel. Compon. Lett*, 2011, 20, (8), pp. 426–428.

[3] M. Strackx, K. Janssen, E. D'Agostino, G. Vandenbosch, P. Reynaert, and P. Leroux, "Ultra-wideband antipodal Vivaldi antenna array with Wilkinson power divider feeding network," in *Proc. IEEE ICUWB*, 2011, pp. 1–4.

[4] H.-M. Hizan, Z. Amback, et al, "Effect of Insertion Losses on Millimeter-Wave SIW Filters Using LTCC Technology," *2015 IEEE International RF and Microwave Conference (RFM)*, Kuching, Malaysia.

[5] C. P.Wen, "Coplanr waveguide: a surface strip transmission line suitable for nonreciprocal gyromagnetic device applications", *IEEE Trans*. MTT-7, 1969, 1087-1090.

[6] H. Issa, P. Ferrari, E. Hourdakis, and A. G. Nassiopoulou, "On-chip high-performance millimeter-wave transmission lines on locally grown porous silicon areas," *IEEE Trans. Electron Dev*., vol. 58, no. 11, pp. 3720–3724, Nov. 2011.

[7] Tang, X.-L., Franc, A.-L., Pistono, E., Siligaris, A., Vincent, P., Ferrari, P., and Fournier, J," Performance improvement versus CPW and loss distribution analysis of slow-wave CPW in 65mm HR-SOI CMOS technology," *IEEE Trans. Electron Devices*, 2012, 59, (5), pp. 1279-1285.

[8] G. Ghione and C.U.Naldi, "Coplanar waveguide for MMIC applications: Effect of upper shielding, conductor backing, finite extent ground planes, and line-to-line coupling", *IEEE Trans*. MTT-35, 1987, 260-267.

[9] Hong, J.S.G. and Lancaster, M.J., 2004. Microstrip filters for RF/microwave applications (Vol. 167). John Wiley & Sons.

[10] P. Vélez, J. Selga, J. Bonache, and F. Martín, "Slow-wave inductivelyloaded electromagnetic bandgap (EBG) coplanar waveguide (CPW) transmission lines and application to compact power dividers," in *Proc. Eur. Microw. Conf*. (EuMC), Oct. 2016, pp. 104–107.

[11] Tiku Yu, "A Broadband Wilkinson Power Divider Based on the Segmented Structure", *Microwave Theory and Techniques IEEE Transactions o*n, vol. 66, no. 4, pp. 1902-1911, 2018.

[12] C. Li, , L. B. Lok, A. Khalid, V. Papageorgiou, J. Grant, and D. R. S. Cumming, "A coplanar ring power divider with high isolation for Vband and W-band applications," Proceedings of the 42nd European Microwave Conference, 57–60, 2012.

[13] C. Li, L. B. Lok, A. Khalid, and D. R. S. Cumming, "Coplanar ring divider with wideband high isolation performance," *Progress Electromagn. Res. Lett*., vol. 25, pp. 1–10, 2011.

[14] E.-M. Fall, F.-Domingue, and A. Reinhardt, "Design of RF Power Combiner/Divider based on Surface Acoustic Wave Longitudinally Coupled Resonators," *2017 IEEE International Ultrasonics Symposium (IUS)*, Washington, DC, USA.

[15] J. Zhou, H, Qian, D. Huang and X. Luo, "Ultra-Wideband (UWB) Wilkinson Power Divider With Ultra-Narrow Dual-Notched Bands Using Embedded CPW Resonators," *2017 IEEE MTT-S International Microwave Symposium (IMS*), Honololu, HI, USA.

[16] G. Leon, L.-F. Herran and F.-L. Heras, "Novel CPW Power Divider Based on Resonators," European Conference on Antennas and Propagation (EUCAP), 2012 6th. Prague, Czech Republic.

[17] Ma, Z, Kawaguchi, T, Kobayashi, Y, Koizumi, D, Satoh, K, Narahashi, S."A miniaturized high temperature superconducting bandpass filter using CPW quarter-wavelength spiral resonators'. *IEEE MTT-S, Int. Microwave Symp. Digest*, June 2006, pp. 1197–1200.

[18] Z. Xu, "A compact dual-band bandpass superconducting filter using microstrip/CPW spiral resonators," *IEEE Microw. Wireless Compon. Lett*. vol. 23, no. 11, pp. 584–586, Nov. 2014.

[19] K. Song, X. Ren, F. Chen, and Y. Fan, "Compact in-phase power divider integrated filtering response using spiral resonator," *IET Microw. Antennas Propag*., vol. 8, no. 4, pp. 228–234, 2014.

[20] T. Zheng et al., "Design of compact superconducting diplexer with spiral short-circuited stubs," *IEEE Trans. Appl. Supercond.*, vol. 24, no. 2, Apr. 2014, Art. ID. 1500405.

[21] T. N. Zheng et al., "Compact superconducting diplexer design with conductor-backed coplanar waveguide structures," *IEEE Trans. Appl. Supercond*., vol. 25, no. 2, Apr. 2015, Art. no. 1501304.

[22] S. Bastioli, L. Marcaccioli, and R. Sorrentino, "An original resonant Y-junction for compact waveguide diplexers," in *IEEE MTT-S Int. Microw. Symp. Dig*., Jun. 7–12, 2009, pp. 1233–1236.

[23] C. E. Saavedra, "Diplexer Using a Circulator and Interchangeable Filters," Proceeding of the 7th International Caribbean Conference on Devices, Circuits and Systems, Mexico, 28-30 April 2008, pp. 1-5. doi:10.1109/ICCDCS.2008.4542631.

[24] X. Guan et al., "Compact, low insertion-loss, and wide stopband HTS diplexer using novel coupling diagram and dissimilar spiral resonators," *IEEE Trans. Microw. Theory Techn*., vol. 64, no. 8, pp. 2581–2589, Aug. 2016.

[25] A. O. Nwajana, and K. S. K. Yeo, "Microwave diplexer purely based on direct synchronous and asynchronous coupling," Radio engineering, vol. 25, no. 2, pp. 247-252, Jun. 2016.

[26] Xia, W. (2015). Diplexers and Multiplexers Design by Using Coupling Matrix Optimisation. Ph.D Thesis, University of Birmingham. Etheses.bham.ac.uk.

Chapter 6 Summary and Future Work

6.1 Summary

To summarise the contents of this thesis, it has been demonstrated that adding capacitors in parallel with transmission lines can effectively adjust the operating frequency of PDs. By carefully choosing the PD topology and the impedance of the transmission lines, broadband and reconfigurable responses with a wide tuning range can be achieved. Experiments have validated the design methods.

The other research objective is mm-wave PDs. Due to some common challenges in mm-Wave device design, such as high loss and low tolerance of fabrication error, the development of mm-Wave PDs is very challenging. Based on the improvement of manufacturing techniques, many simple but effective designs are promising.

Several key challenges regarding PD designs are listed below:

1) Due to the increasing number of multi-standard systems, PDs with multi-band, broadband or reconfigurable features have been investigated in depth. Although many published papers provide plenty of comprehensive solutions, most of them are hybrid technologies that require several essential design elements, such as using both coupled-line and stepped-impedance transformers to achieve wideband performance. Hybrid solutions are good choices for specific applications because they accomplish specifications. However, more versatile but straightforward designs are the most desired, because a simple design is more desired to be integrated into systems with minimised side effects.

2) As the competition among communication industries increases the scarcity of radio spectrum resource, PDs at higher frequencies, from mm-Wave to even Terahertz bands, are in high demand. Feasible solutions need to be investigated in depth.

3) Most high frequency-related researches are focusing on waveguide structures as they perform low loss and high-power capability features. However, they usually suffer from the large size and relatively high cost. Moreover, conventional waveguides are not perfect choices

for circuit integration. As a result, planar designs working on such high frequencies are imperatively desired. Since the majority of planar PDs are designed based on transmission lines, they usually have relatively high loss for high-frequency applications. PDs with a simple layout and a low-cost precision fabrication process are of great value to be investigated.

6.2 Key Contributions

This thesis has provided a thorough study of microwave PD designs and also presented a promising mm-Wave PD design.

The key contributions are detailed as follows.

Chapter 2

1) A comprehensive literature review has been carried out to show the critical and recent development of broadband and reconfigurable PD designs in microwave communication systems. It has also depicted several available mm-Wave PD designs to demonstrate the design and fabrication challenges.

Chapter 3

2) The idea of adding capacitors in parallel with main transmission lines is firstly proposed. This proposed structure solves three main challenges. Firstly, the added capacitors have broadened the overall bandwidth to a great extent (2.7:1 of 15-dB bandwidth for a two-way prototype). Secondly, changing the capacitance can result in a tunable bandwidth. The last key point is from the physical aspect of view. The proposed structure has two short stubs connecting the output ports which adding the physical isolation between them.
3) Also, an eight-way PD is designed and fabricated by cascading two-way structures together. The measured results indicate that the idea can be adapted to multi-way broadband PD designs which validates the importance of this work.

Chapter 4

4) By adding a pair of the capacitor in parallel with the main transmission lines, and by carefully choosing the lengths and impedances of the transmission lines, the operational frequency of the PD can be tuned over a wide range. The design in this Chapter focused on the main transmission lines and the stubs that connect the main transmission lines and the lumped-elements RLC in the isolation circuit. An analytic solution is provided in the

chapter to predict and control the frequency tuning range and its return loss performance. The designed two-way circuit uses three varactors and their corresponding bias circuits to tune the frequency band electrically. Measurement shows that the centre frequency with better than 20 dB return loss can be tuned from 0.9 GHz to 4.2 GHz, which is the widest compared to other similar works.

Chapter 5

5) The work in chapter 5 focuses on developing an mm-Wave PD using rectangular spiral resonators. Using a spiral resonator will significantly reduce the occupied area of the circuit. Besides, using a common resonator near the input port can achieve a low loss performance and also size reduction compared the traditional design using a T- or Y-junction and air-bridges. A CPW structure has its signal line and ground on the same side of the substrate which reduces the complexity of fabrication and makes it easier for integration. The design can effectively control the power division by changing the distances between the resonators. Moreover, a diplexer has been implemented by appropriately choosing the size and coupling coefficients of the resonators. Good demonstration has been made by testing frequency scaled-down PD and diplexer.

6.3 Future Work

Based upon the summary above, and considering the challenges of existing technologies, further works can be carried out in the following areas.

1) In Chapter 5, a 2 GHz PD and a diplexer have already been designed and tested to validate the design theory due to facility limitation. PDs and diplexer operating at 50 GHz can be fabricated and measured by using following method.

The PD and diplexer will employ the fabrication process in [1] on a 625 μm thick semi-insulating GaAs substrate with a loss tangent of 0.006. All patterns are defined using Electron beam lithography (EBL) which is a powerful technique for creating nanostructures that are too small to fabricate with conventional photolithography.

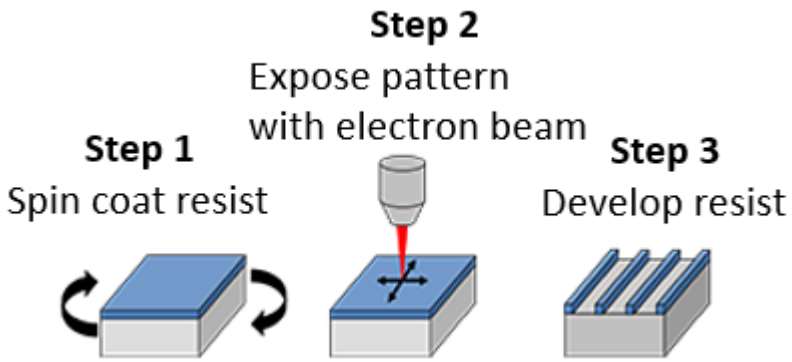

Fig. 6. 1 Resist pattern schematic by using EBL [2].

The technique works by moving a highly focussed electron beam [2] over a sample to write out a pattern designed with Computer-aided Design (CAD) tools. The pattern is recorded in an electron sensitive film (or resist) deposited on the sample before exposure by spin coating. The electron beam induces a change in the molecular structure and solubility of the resist film. Following exposure to the electron beam as shown in **Fig. 6. 1**, the resist is developed in a suitable solvent to selectively dissolve either the exposed or unexposed areas of the resist. There are two main reasons for using EBL. One is precision. EBL process can create structures at the level of 10 nm.

The device will be tested using on-wafer probes and a VNA system as shown in **Fig. 6. 2**(c). A typical 110 GHz system contains a VNA, cables, probes, probe positioners, probe station contact substrate, calibration substrate, calibration software, bias supply and a microscope [3]. The components will be tested using a pair of DC-110 GHz Ground-Signal-Ground (GSG) probes (as shown in **Fig. 6. 2**(a)(b)) with a 100 µm pitch separation from GGB Industries and an Agilent PNA N5250C on a Cascade semi-automated probe station. CPW transitions from 20 µm /15 µm to 60 µm /40 µm will be deployed at three ports to be compatible with the geometry of the test probes. A third probe terminated by a broadband 50 Ω load on the 1 mm coaxial port side is used to load the idle port [4]. This three-port component test method, unlike the conventional method that requires three devices of the same design but terminated with 50 Ω thin-film resistors for different ports [5], allows the same Device Under Test (DUT) to be characterised using a two-port VNA. Off-wafer calibration using a calibration substrate CS-15 from GGB Industries will used to calibrate the system reference plane to the probe tips before taking measurements.

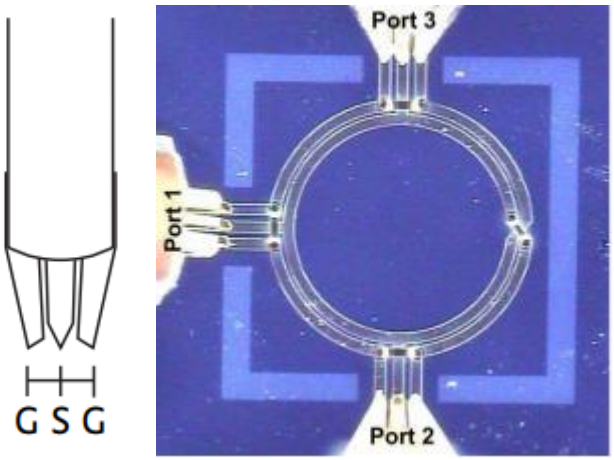

(a) (b)

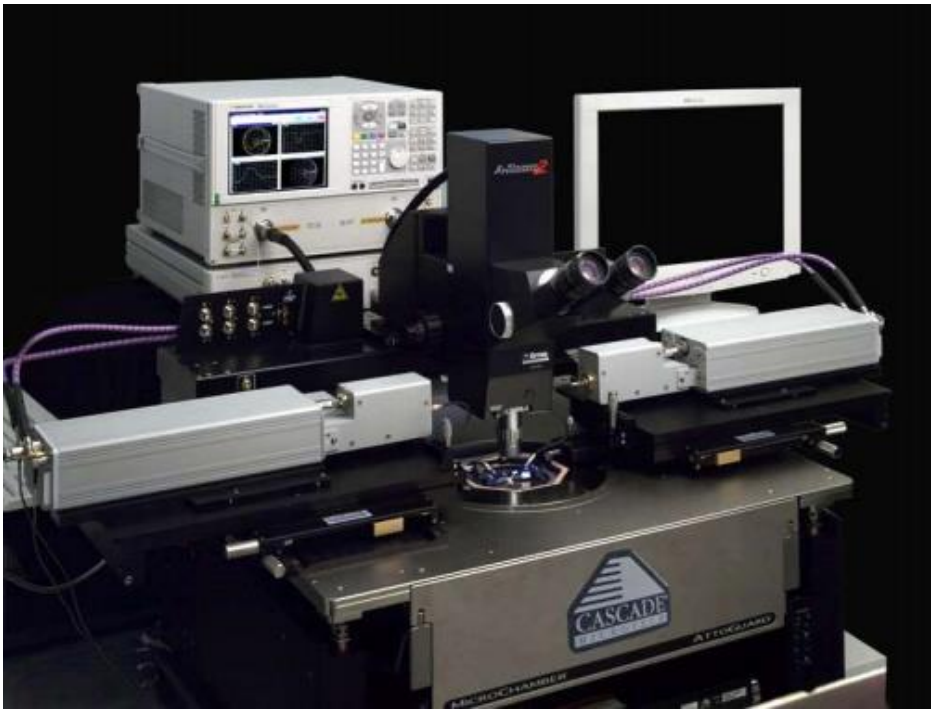

(c)

Fig. 6. 2 (a) The GSG probe, and (b) microphotograph of the fabricated ring divider under test [6], (c) Typical 110 GHz System [7].

The calibration will employ the Short-Open-Load-Reciprocal Thru (SOLR) method [8]-[10] for Port 1 to Port 2/Port 3, and a Line-Reflect-Reflect-Match (LRRM) calibration method will be used for Port 2 to Port 3 isolation measurement for it is not sensitive to the load asymmetry [11]. SOLR uses the SOLT Short- Open-Load Thru (SOLT) short, open, and load standards and requires the same characterization knowledge. SOLR calibration does require that the

through standard be reciprocal, such that S_{21} equals S_{12}. The probe station measurement requires a circuit configuration of input port to be orthogonal to the directions of output ports. Most circuits would not strictly satisfy the measurement requirements so that calibration is essential in order to obtain accurate results. The limited knowledge requirement on the through standard makes SOLR calibration ideally suited for situations where a non-ideal through standard is desired, such as with on-wafer probing where the probes are positioned 90° from each other (orthogonally) during the desired measurement. A through standard with a 90° bend could be used for calibration. A bend makes the through behave non-ideal and therefore creates errors or degradation in those calibration models relying on the ideal characteristics. SOLR calibration can overcome this limitation since it does not rely on an ideal through model so that eliminate degradation during the measurement. The use of the SOLR algorithm with a 90° through standard simplifies both calibration and measurement, which provides the best calibration for these less ideal measurement configurations.

2) Based on the results in Chapter 3, the topology is promising to be used in mm-wave PD designs to extend the operational bandwidth. However, surface mount capacitors are not widely available at such high frequencies. An interdigital capacitor as shown in **Fig. 6. 3** may be a good candidate as a semi-lumped element for mm-Wave device designs [12]-[13]. The design objectives are to provide the desired capacitance at the design frequency in a reasonably small area. The interdigital capacitors are easy to fabricate and have more freedom to achieve desired capacitance due to their structures.

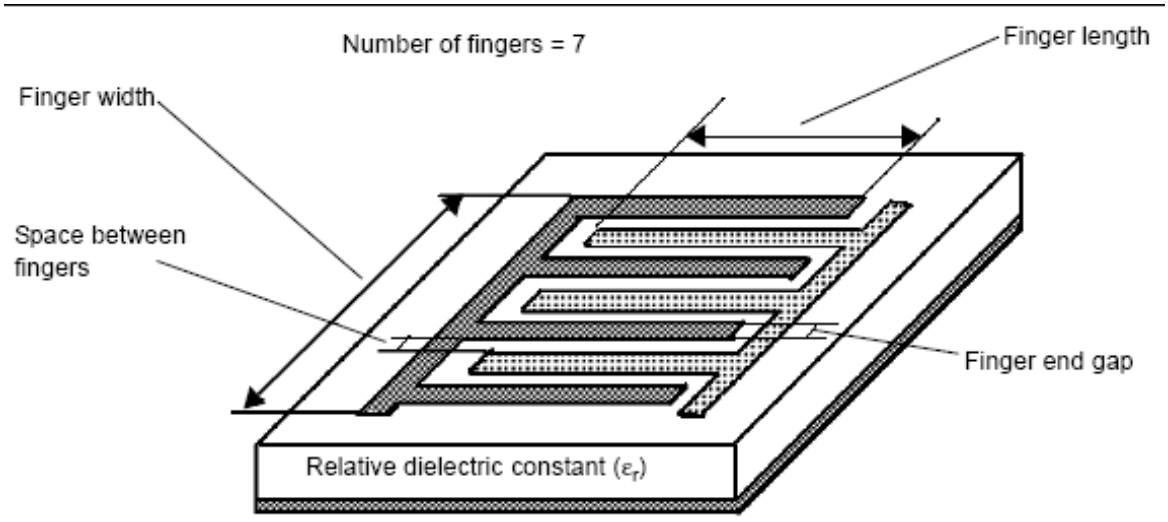

Fig. 6. 3 Configuration of an interdigital capacitor.

3) Since reconfigurable devices become more and more popular, it is of great value to investigate the conept in more depth. The term "reconfigurable" here may refer to different types of response instead of the centre frequency, bandwidth or power division ratio. For example, in Chapter 5, the PD that was designed based on coupling structures can be switched to a diplexer. Many papers on reconfigurable operating frequency [14]-[17] have been published. They are based on integrating varactors to the circuit to continuously control the resonant frequencies changing in a certain range. As the work in [6] indicates, the external quality factor Q_e and the operating frequency can be adjusted by altering the varactors on strait- and ring-slots. As a result, the two frequency bands can be controlled synchronously. Thus, a PD and diplexer can be switchable if the circuit configurations and bias circuits are carefully designed.

References

[1] C. Li, A. Khalid, V. Papageorgiou, L. B. Lok, and D. R. S. Cumming, "A wideband CPW ring power combiner with low insertion loss and high port isolation," *IEEE Microw. Wireless Compon. Lett*., vol. 22, no. 11, pp. 580–582, Nov. 2012.

[2] Sheffield, U. (2018). Overview - EBL Patterning - Electron Beam Lithography - The University of Sheffield. [online] Sheffield.ac.uk. Available at: https://www.sheffield.ac.uk/ebl/patterning [Accessed 16 Oct. 2018].

[3] Fisher, G. (2018). A guide to Successful on Wafer Millimeter wave Rf characterisation. [online] Keysight.com. Available at: https://www.keysight.com/upload/cmc_upload/All/OnWaferMillimeter.pdf [Accessed 16 Oct. 2018].

[4] C. Li, et al., "Novel on-wafer measurement technique for passive multiport devices in millimetre wave frequency range", in 9th Millimetre-wave User Group Meeting. Unpublished, p. 2, Glasgow, UK. March 2011.

[5] D. Lopez-Diaz, et al., "Monolithic integrated 210 GHz couplers for balanced mixers and image rejection mixers". *Workshop on Integrated Nonlinear Microwave and Millimeter-Wave Circuits (INMMIC)*, 2010: p.4.

[6] C. Li, L. B. Lok, A. Khalid, and D. R. S. Cumming, "Coplanar ring divider with wideband high isolation performance," *Progress Electromagn. Res. Lett.*, vol. 25, pp. 1–10, 2011.

[7] Fisher, G. (2018). A guide to Successful on Wafer Millimeter wave Rf characterisation. [online] Keysight.com. Available at: https://www.keysight.com/upload/cmc_upload/All/OnWaferMillimeter.pdf [Accessed 16 Oct. 2018].

[8] S. Basu and L. Hayden, "An SOLR calibration for accurate measurement of orthogonal on-wafer DUTs," *IEEE MTT-S Digest, Denver CO*, Jun 1997, pp. 1335-1338.

[9] Keysight Agilent Technologies. (2006). Advanced Calibration Techniques for Vector Network Analyzers. [online] Available at: http://anlage.umd.edu/Agilent_Advanced_VNA_calibration.pdf [Accessed 15 Oct. 2018].

[10] Zone.ni.com. (2018). Short-Open-Load-Reciprocal (SOLR) Calibration - NI Vector Network Analyzers (NI-VNA 14.0) Help - National Instruments. [online] Available at: http://zone.ni.com/reference/en-XX/help/373153D-01/vnahelp/calibration_solr/ [Accessed 15 Oct. 2018].

[11] Citeseerx.ist.psu.edu. (2018). A Review of VNA Calibration Methods. [online] Available at: http://citeseerx.ist.psu.edu/viewdoc/download?doi=10.1.1.662.2977&rep=rep1&type=pdf [Accessed 16 Oct. 2018].

[12] F. Aryanfar and K. Sarabandi, "Characterization of semilumped CPW elements for millimetre-wave filter design," *IEEE Tran. Microwave Theory Techn*., vol. 53, no. 4, pp. 1288–1293, Apr. 2005.

[13] F. Aryanfar and K. Sarabandi, "Compact millimeter-wave filters using distributed capacitively loaded CPW resonators," I*EEE Trans. Microw. Theory Tech*., vol. 54, no. 3, pp. 1161–1165, Mar. 2006.

[14] G. Zhang, Z. Qian and J. Yang, "Design of a compact microstrip power-divider diplexer with simple layout," *Electronic Letters*, vol: 4, issue:16, pp.1007-1009, Aug. 2018.

[15] M. S. Sorkherizi, A. Vosoogh, A. A. Kishk, and P.-S. Kildal, "Design of integrated diplexer-power divider," I*EEE MTT-S Int. Microw. Symp*. Dig., May 2016, pp. 1–3.

[16] P. Deng, W. Lo, B-L. Chen and C.-H. Lin, "Designs of Diplexing Power Dividers," *IEEE Access*, vol:6, pp. 3872-3881, Jan. 2018.

[17] X. Liu, Z. Tian, H-Jenny Qian, et al, "Reconfigurable Diplexer Using λ/2 Resonator with Hybrid Varactor Embedded Stepped-Impedance Open-Stub and Slot," *IEEE MTT-S International Wireless Symposium (IWS)*, Chengdu China, May 2018.

END